Dissertation
submitted to the
Combined Faculties for the Natural Sciences and for Mathematics
of the Ruperto-Carola University of Heidelberg, Germany
for the degree of
Doctor of Natural Sciences

Put forward by
Kambis Veschgini
born in Tehran, Iran
Oral examination: December 14, 2016

A Combined Functional Renormalization and Mean-Field Study of Competing Orders in the Two-Dimensional Hubbard Model

Referees:

Prof.Dr. Manfred Salmhofer
Prof.Dr. Andreas Komnik

Studie des zweidimensionalen Hubbard Models durch kombinierte funktionale Renormierung und Mean-Field-Theorie

Kurzzusammenfassung: Der Gegenstand der vorliegenden Arbeit ist das zweidimensionale Hubbard-Modell. Mit Hilfe der funktionalen Renormierungsgruppe wird das Phasendiagramm des 2D-Hubbard-Modells in der statischen Näherung abgeschätzt und dann unter Berücksichtigung der Frequenzabhängigkeiten und vollständiger Selbstenergie verfeinert. Der Fokus fällt hierbei insbesondere auf die Umgebung eines quantenkritischen Punktes an dem das Verhalten des Systems von dem einer Fermi-Flüssigkeit abweicht. In Mean-Field-Rechnungen wird klar, dass die spezielle Frequenzabhängigkeit der Selbstenergie starke Auswirkungen auf den Grundzustand hat. Des Weiteren wird der Einfluss der Dichte-Dichte-Wechselwirkung auf die Lebensdauer der Quasiteilchen ermittelt. Im Zusammenhang mit diesen Untersuchungen werden eine Sattelpunkt-Formulierung der Schwinger-Dyson Gleichungen sowie ein neues Renormierungsgruppen-Schema entwickelt, welche für alle fermionischen Systeme gültig sind.

A Combined Functional Renormalization and Mean-Field Study of Competing Orders in the Two-Dimensional Hubbard Model

Abstract: The primary subject of this thesis is the two-dimensional Hubbard model. Using the functional renormalization Group in static approximation we will present the phase diagram of the 2D-Hubbard model and refine it by including frequency dependencies and full self-energy effects. The focus will fall on the vicinity of the quantum critical point, where the system shows a non-Fermi-liquid-like behavior. In mean-field calculations, we show that the frequency dependence of the self-energy has a substantial impact on the ground state. Furthermore, we investigate the relation between the density-density interaction and the quasiparticle lifetime. During the course of our study, we will develop a saddle-point formulation of Schwinger-Dyson equations and present a new renormalization group scheme which is valid for all fermionic systems.

Contents

Introduction

Motivation

Numerous interesting phenomena in physics are believably described by quantum field theories which we cannot yet solve reliably. A prime example is unconventional superconductivity. Even the Hubbard Hamiltonian, the simplest one assumed to capture the relevant physics of some high-temperature superconductors has turned out to be extremely tough to solve in any non-trivial limit. The relevant parameter region is not accessible by perturbative methods, nor can it be treated with exact diagonalization or lattice Monte Carlo methods. Established and successful methods of the past don't carry over. Meanwhile, on the one hand improving our understanding of the Hubbard model seems essential for the understanding of superconductivity in cuprates. On the other hand, since the Hubbard Hamiltonian is the simplest in its class, our ability to handle more complicated models is naturally limited by our ability to solve this model. For the latter reason, it serves well as a playground for the development of new tools and methods for fermionic quantum field theories. The aim of this work is not only to contribute to our understanding of the Hubbard model but also to push the development of such new non-perturbative techniques.

The Hubbard Model

The model we refer to as the Hubbard model was introduced in 1963 by Gutzwiller [1] and Hubbard [2] as a simple, approximate model describing the interaction of electrons and their collective behavior in solids. The model is based on the tight-binding approximation where the set of bound and continuous levels of each electron are reduced to a single (spin degenerate) localized state and the electrons can *hop* between the states of neighboring lattice sites. The screened Coulomb interaction is approximated by an onsite repulsion. In the 60s the Hubbard model was found to successfully describe magnetism

and the metal-insulator transition. The effect of the correlations turned out to be pronounced and the Hubbard model was found to have a rich phase diagram, which could not be understood with predecessor models like the one-electron theory of Hund and Mulliken or the localized electron model of Heitler-London.

The Hubbard Hamiltonian,

$$H = \sum_{i,j} \sum_{\sigma} t_{i,j} \left(\hat{c}^{+}_{i,\sigma} \hat{c}_{j,\sigma} + \text{h.c.} \right) + U \sum_{i} n_{i,+} n_{i,-} \,,$$

consist of two contributions. The kinetic term describing the *hopping* of electrons between sites and the on-site interaction approximating the interaction between electrons. The hopping matrix $t_{i,j}$ is assumed to be translational invariant and it is usually restricted to nearest- and next-to-nearest-neighbors. $U > 0$ corresponds to a repulsive (e.g. Coulomb) interaction while $U < 0$ would describe an attractive interaction. The summation goes over lattice sites labeled by i, j in D dimensions and spin index $\sigma \in \{+, -\}$.

The apparent simplicity of the Hubbard Hamiltonian is deceptive. Despite considerable effort during the past decades, exact results are very rare. Rigorous results are available for $D = 1$. For $U > 0$, nearest-neighbors hopping only and at half filling, Lieb and Wu solved the model exactly and showed that the ground state exhibit no conductor-insulator transition [3]. At $T = 0$ the excitation spectrum was then computed by Ovchinnikov [4] and the magnetic susceptibility by Shiba [5]. Low-Temperature Specific-Heat is known due to Takahashi [6]. Exact finite temperature results are rare and their validity is usually restricted to a certain limit of another parameter of the model. Taking the limit $D \to \infty$ simplifies the diagrammatic treatment substantially [7], but interestingly the correlations among the fermions remain non-trivial. Certain bounds are known to hold for arbitrary dimensions. In particular Langer and Mattis have found upper and lower bounds to the ground state energy [8] and upper bounds on the susceptibilities have been computed by Kubo and Kishi [9]. There are also two theorems on the angular momentum of the ground state of the Hubbard model proven by Lieb [10]. The first theorem states that for $U < 0$ it has angular momentum $S = 0$ for every electron filling. The second theorem implies that for $U > 0$ with a bipartite lattice and a half-filled band, the angular momentum is given by $S = \frac{1}{2} | \|B\| - \|A\| |$, where $\|\bullet\|$ is the number of sites in the corresponding sublattice. In both cases the ground state was also shown to be unique apart from the trivial $(2S + 1)$-fold degeneracy. For $\|B\| \neq \|A\|$ the second theorem gives rise to an example of itinerant ferromagnetism.

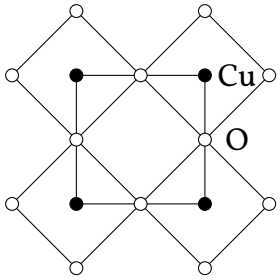

Figure 1: Schematic picture of the CuO_2 plane in cuprates. Copper atoms represented by black circles sit on a square lattice with oxygen atoms depicted by white circles in between.

The strong and weak coupling limits have been treated extensively in the literature. In the strong coupling limit, Gutzwiller's approximation [11] and the slave-boson theory introduced by Kotliar and Ruckenstein [12] have been very successful. The weak coupling limit can be treated with perturbation theory. A conserving approximation was introduced by Bickers [13]. For intermediate values of the coupling mean-field and Hartree-Fock calculations are partially successful. They describe the magnetic orders particularly well in two dimensions [14] but fail to capture the superconducting tendencies in the case of a repulsive interaction. Numerical Monte Carlo and exact diagonalization techniques are limited to very small clusters. For a review on the history of the Hubbard model please refer to the reprint collection [15].

The discovery of high-temperature superconductivity in cuprates by Bednorz and Müller in 1986 [16] has revived the interest in the Hubbard model. The common building block of cuprates is copper oxide planes sandwiched between charge reservoir blocks. The two-dimensional Hubbard model is believed to be the minimal model capturing the essential physics of this class of high-temperature superconductors [17, 18]. The CuO_2 plane is shown schematically in Figure 1. The copper atoms sit on sites of a square lattice, which maps to the lattice of the one-band Hubbard model.

In two dimensions and for intermediate interaction strengths, such as when it becomes of the same order of magnitude as the kinetic term —which seems to be the case for cuprates [19]— straightforward perturbation theory in not usually satisfactory. Infinite summations in the form of ladder approximations are insufficient when more than one channel becomes important and their interplay becomes relevant. The method of choice for us, in this case, is the *functional renormalization group* (fRG). It sums up perturbative diagrams up to an infinite order in the bare interaction. Functional RG goes beyond the Fermi liquid description and lets us capture any anomalous frequency dependence in the

interaction vertex or self-energy. Furthermore, different interaction channels are taken into account in an unbiased way.

Functional Renormalization Group

The functional renormalization group is an exact description of the dependence of free-energy or some other generating functional on a *scale* parameter Λ, which can be a physical quantity like temperature or artificial like a momentum cutoff. The latter one is usually introduced using a regulating function suppressing infrared fluctuations smaller than the scale parameter. The goal is then to start in the trivial limit $\Lambda \to \infty$ and compute the correlations function in the limit $\Lambda \to 0$ where all fluctuations are included. In this sense, the fRG bridges the gap between microscopic dynamics and macroscopic thermodynamics. The exact *flow* can be expressed in terms of an infinite hierarchy of differential equations. Non-perturbative solutions follow from integrating the ODES in some approximation.

The exact renormalization group was first introduced by Polchinski [20] for bosonic amputated connected Green functions. A fermionic version was formulated by Brydges and Wright [21]. Flow equations for Wick-ordered effective interactions were derived by Salmhofer [22]. The most used scheme for numerical calculation is formulated in terms of the generating functional of the one-particle irreducible correlation functions and was introduced by Wetterich [23] and Salmhofer and Honerkamp [24], respectively. What makes this scheme particularly practical is that it's local in the scale parameter, the self-energy feedback is included automatically and it contains only one-particle irreducible contributions. An alternative formulation of the exact renormalization group based on a continuous unitary transformation of the Hamiltonian was presented by Wegner [25]. For a review on fRG please refer to [26] or [27].

Generally, flow equations cannot be solved exactly. Approximations follow from different truncations of the hierarchy of equations. Local conservation laws usually get spoiled by a naive truncation. A very successful approximation was derived by Katanin [28] and extended to flows with symmetry breaking by Salmhofer et. al [29]. Following the fermionic flow into a phase with broken symmetry is possible but numerically demanding. Alternatives consist of partial bosonization during the flow due to Floerchinger and Wetterich [30], mean-field calculations based on the effective action (see Chapter 4) or in a different approach introduced by Wang, Eberlein and Metzner [31].

fRG methods have been used in past years to study the Hubbard model and progress has been made in many areas. First, two-patch studies limited to van Hove filling gave a rough approximation of the interaction vertex [32, 33, 34, 35, 36, 37, 38]. Then the four-point function was approximated in n-patch schemes and studied in different schemes [39, 40, 41]. Early studies revealed that even though a sharp momentum cutoff has technical advantages, it can artificially suppress interaction in the magnetic channel. To overcome the problem, temperature flow was introduced by Honerkamp and Salmhofer in [42]. Around the same time, the inclusion of the self-energy in flows with a momentum cutoff was investigated in [43, 44]. Later the frequency dependence of the self-energy was studied and more recently flows with frequency dependent interaction vertex and purely imaginary self-energy were computed [45]. Several studies have revealed a suppression of the quasiparticle weight at van Hove points [46, 47] and a non-Fermi-liquid-like self-energy behavior was found in [48].

Thesis Outline

This thesis is organized as follows: In Chapter 1 we make the relation between Katanin's scheme and Schwinger-Dyson equations explicit. Then we present a generalization of the Luttinger-Ward functional, which can be used as the basis for the construction of conserving approximations within the framework of Baym and Kadanoff. In Chapter 2 we test and compare the scheme developed in the first chapter against Katanin's truncation. In Chapter 3 we determine the instabilities of the Hubbard model in a large parameter regime. In Chapter 4 we study the effects the non-Fermi-liquid-like self-energy found in previous studies by Giering, Husemann and Salmhofer on gap formation. We also investigate the relation between a certain frequency dependent density-density interaction found in the fRG flow at the quantum critical point on the self-energy and quasiparticle lifetime. Finally, in Chapter 5 we discuss some of our findings, answer some questions posed by our studies and draw conclusions.

In the following I present a one page summary of each chapter.

Summary of Chapter 1

In Chapter 1 we show that for a fermionic system with a bare propagator C and a generic two-particle interaction v there exists a functional,

$\mathscr{F} = \ln\det G -$ 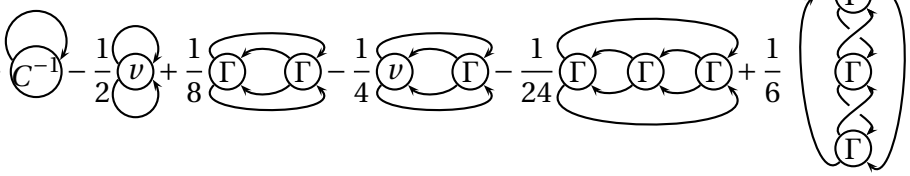 $+\cdots$, (short version of Eq. (1.8) on page 19)

of the self-energy Σ or the full propagator G, represented here with a heavy line, and the one-particle irreducible four-point correlation function $\Gamma^{(4)}$ with the following property. $\mathscr{F}(\Sigma,\Gamma^{(4)})$ is variational in both parameters and for G and $\Gamma^{(4)}$ obeying Schwinger-Dyson equations we have

$$\frac{\mathrm{d}}{\mathrm{d}\Sigma}\mathscr{F}\left(\Sigma,\Gamma^{(4)}\right)=0 \quad \text{or} \quad \frac{\mathrm{d}}{\mathrm{d}G}\mathscr{F}\left(\Sigma,\Gamma^{(4)}\right)=0\,, \qquad \frac{\mathrm{d}}{\mathrm{d}\Gamma^{(4)}}\mathscr{F}\left(\Sigma,\Gamma^{(4)}\right)=0\,. \qquad \text{(Eq. (1.9) on page 20)}$$

Assuming that $C = C_\Lambda$ depends differentiably on a parameter Λ, we can formulate flow equations to solve these self-consistent saddle-point equations. In particular the solution of the well known Katanin's equations,

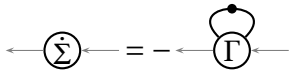 (Eq. (1.14) on page 22)

and

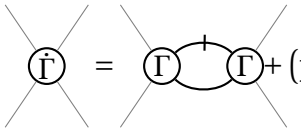 (Eq. (1.12) on page 22)

solves the saddle-point equations up to $\mathscr{O}\left(\Gamma^{(4)3}\right)$. In the flow equations $\frac{\mathrm{d}}{\mathrm{d}\Lambda}G \simeq$ and stands for the single-scale propagator $S = \dot{G} + G\dot{\Sigma}G$.

The functional $\mathscr{F}$ is a generalization of the Luttinger-Ward functional which eases the construction of conserving approximation. The idea of using flow equations for finding approximate solutions to these equations leads to a new scheme for fermionic flow equations. We refer to this scheme as Schwinger-Dyson renormalization group. It coincides with Katanin's truncation at one-loop level and generalizes this successful scheme by proving a systematic way of incorporating higher order corrections.

Summary of Chapter 2

In Chapter 2 we compute the renormalized couplings of the two-dimensional Hubbard model at van Hove filling using self-consistent and flow equations developed in Chapter 1. In both cases we use a frequency dependent infrared regulating function which introduces a scale Ω. Since the most relevant scattering processes are those between states near van Hove singularities, a minimal parametrization consists of four couplings,

(Fig. 2.1 on page 26)

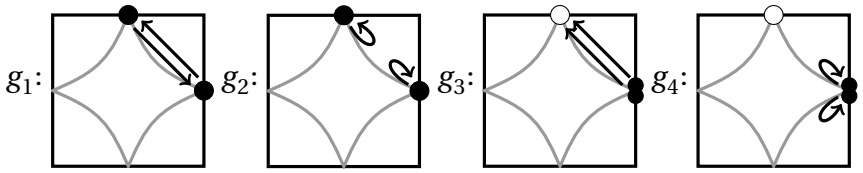

which are assumed to be spin-independent. In the schematic representation the initial and final particles are connected by an arrow and have the same spin.

In a parametrization with n couplings, the self-consistent equation for the interaction vertex has 2^n solutions. We identify the physical solution by solving the equations for many intermediate scales and following the trajectories of the couplings to the ultraviolet limit $\Omega \to \infty$. In this limit the physical couplings converge to their bare values. Considering the couplings as a function of the scale we can identify different instabilities which show themselves through divergent derivatives. In the case of Katanin's flow equations, the couplings diverge themselves. The solutions from the two different approaches agree qualitatively as long as the couplings and their scale derivative remain reasonably small.

We found that for a next-nearest-neighbor hopping $t'/t \approx 0.34$, the physical solution exists up to arbitrary small scales. For smaller hopping parameter we see superconducting and for larger ones ferromagnetic instabilities. This indicates a quantum critical point near $t'/t \approx 0.34$. Results from flow equations show a similar behavior. By analyzing the equations we learn that the physics in the vicinity of the QCP is controlled strongly by the balance between the particle-hole bubbles at momenta (π,π) and $(0,0)$.

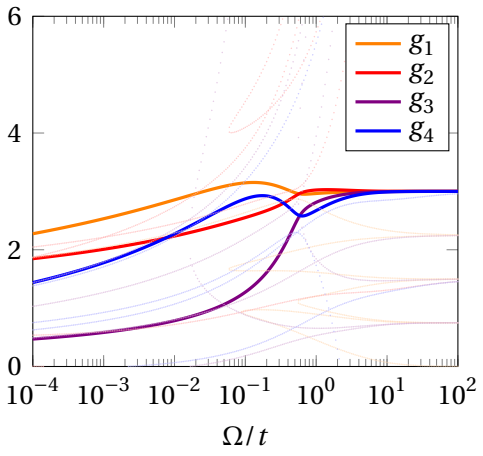

(Fig. 2.2.c on page 31)

Summary of Chapter 3

In Chapter 3 we go through the technical details of setting up n-patch flow equations for the Hubbard model. The same set of equations are then used throughout the thesis to compute flows with or without the inclusion of the self-energy or frequency dependence of the interaction vertex and self-energy. Projecting all frequencies to zero and neglecting the self-energy we obtain the following instability diagram:

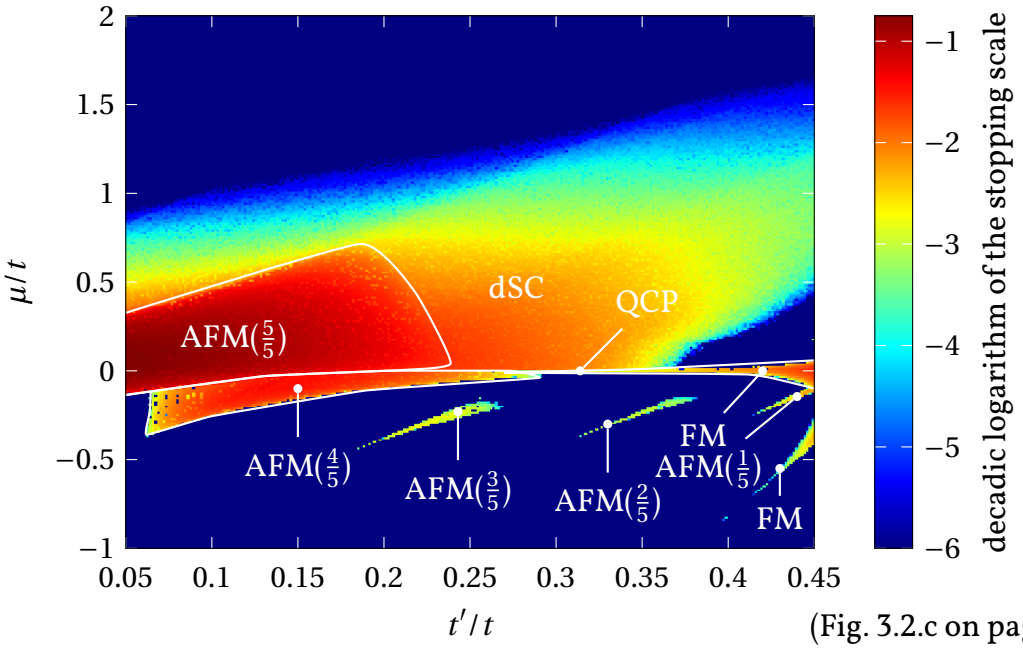

(Fig. 3.2.c on page 47)

In our convention $\mu = 0$ corresponds to van Hove Filling. AFM stands for antiferromagnetic, FM for ferromagnetic and dSC for d-wave superconducting instability. QCP marks the position of the quantum critical point.

We will explain that the region $\mu < 0$ is mostly dominated by incommensurate antiferromagnet instabilities. The instability is not always captured due to the finite resolution of the patching. We discuss how the instability is related to the shape of the Fermi surface.

In the region $\mu > 0$ we find antiferromagnetic and d-wave superconducting instabilities. In some parts of the diagram the stopping scale drops below our numerical limit but we still expect the ground state to be superconducting due to the Kohn-Luttinger effect.

Summary of Chapter 4

In Chapter 4 we continue previous fRG studies of the two-dimensional repulsive Hubbard model by Giering, Husemann and Salmhofer, which have been published in [48], [45] and [49]. These studies provide the effective interaction and imaginary part of the self-energy at some stopping scale at van Hove filling in the vicinity of the critical hopping $\theta^\star = t'/t = 0.341$.

We investigate a toy-model and show that the non-Fermi-liquid-like self-energy $\Sigma \sim (-)\,\mathrm{i}\,\mathrm{sgn}(\omega)|\omega|^{0.74}$ found near $\theta^\star$ suppresses gap formation.

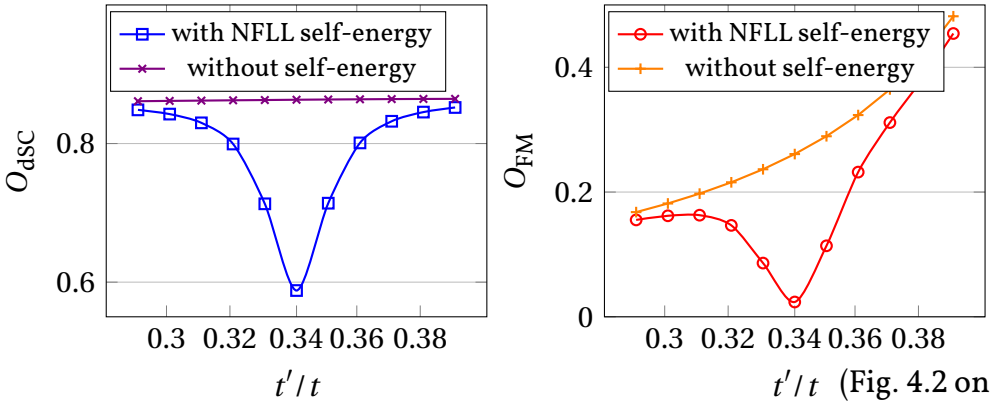

(Fig. 4.2 on page 57)

Then starting with the fRG data, we use the Hubbard-Stratonovich transformation to compute the order parameters for ferromagnetism and Cooper pairing and show that they vanish at the quantum critical point:

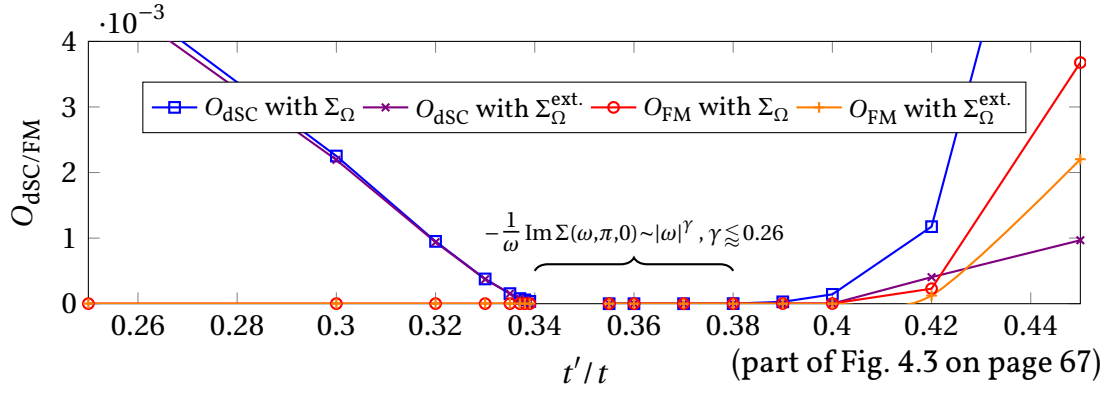

(part of Fig. 4.3 on page 67)

Knowing that the ground state is gapless at the QCP, we investigate the relation between the frequency dependent density-density interaction and the self-energy. The fRG data show an enhanced repulsion at a finite frequency in the density-density channel. We model this interaction with a delta-peak and show that it leads to strong suppression of the quasiparticle lifetime.

Summary of Chapter 5

Chapter 5 is dedicated to clarifying some results and answering certain questions raised by our studies so far.

We will discuss how the one-loop self-energy flow equation captures two-loop contributions and check the consistency of the non-Fermi-liquid-like self-energy.

We will include the full self-energy, i.e. real and imaginary parts both depending on frequency and momenta in fRG calculations. This increases the cost of numerical calculations significantly, but it is important to check the impact of the full self-energy on the results in few selected points. In particular near the QCP where the second derivative of the real part of the self-energy is divergent and slightly away from van Hove filling where it might affect the ferromagnetic instability significantly. In terms of our scale parameter Ω, which represents a soft frequency cut-off, we found that the real part of the self-energy and it's second derivative remain small up to scales as small as $10^{-4}t$ and the impact on the result is negligible. Yet the second derivative will diverge in the limit $\Omega \to 0$ and may require careful treatment, particularly when it comes to rigorous results regarding the zero-temperature ground state. Regarding the ferromagnetic instability we also found that the self-energy doesn't alter the instabilities predicted within the static-vertex approximation in Chapter 3.

We will show that the particular form of the density-density interaction at the QCP is not specific to that point. But mean-field calculations in manner of Chapter 4 cannot be applied away from the QCP.

We will discuss the possibility of choosing a regulating function, which is analytic in the upper-half complex plane, and discuss some advantages and disadvantages of such a regulator.

At the end of the chapter we will draw conclusions.

Chapter 1

Schwinger-Dyson Renormalization Group

Large parts of this chapter's contents have been published in [50] in collaboration with professor Salmhofer.

1.1 Introduction

Renormalization group (RG) and Schwinger-Dyson equation (SDE) hierarchies are widely used methods to study the correlation functions of quantum field theories. The SDE is a hierarchy of integral equations [51, 52] for the Green functions obtained, e.g., by integration by parts in the functional integral representation. The simplest truncation of this hierarchy corresponds to the Hartree-Fock equations and the next level also includes loop corrections to the two-fermion scattering. Depending on the model, these equations may require renormalization subtractions to be well-defined. Even after that, the equations are typically singular integral equations, allowing for solutions that exhibit symmetry breaking or other drastic changes compared to the bare system. The *functional* RG approach (for reviews, see e.g. Refs. [24, 53, 27]) starts by introducing a scale parameter and a modification of the theory that regularizes, i.e., smoothes out singularities, in the propagator. The RG flow is obtained when the regulator is gradually removed by taking a limit of the scale parameter Λ (we use the standard Wilsonian convention that the Λ corresponds to an infrared regulator which is decreased to generate the flow, and eventually sent to zero, $\Lambda \to 0$). The resulting RG equation is a functional differential equation which becomes a hierarchy of equations in the usual expansion in the fields. Instead of a self-consistency, as in the SDE, it describes a flow. This regularizing effect

in the above procedure (often corresponding to a localization in position space) is the main reason for the good mathematical properties of the RG equations. Terms that lead to symmetry breaking or other singular behaviour develop early on in the flow, without any need for assumptions on their type, and gradually grow so that their effect can be taken into account scale by scale.

It is useful to make the relation between the two approaches as explicit as possible. In this chapter, we will formulate RG equations based on the SDE hierarchy, and then relate Katanin's truncation [28] of the RG hierarchy for the one-particle irreducible vertex functions to a particular truncation of the RG derived from the SDE. This is important because Katanin's truncation scheme has been shown [28, 29] to generate a flow that automatically satisfies certain self-consistency equations, and because this scheme has been used extensively in RG calculations, both for fermionic and for spin systems [27].

The full SDE hierarchy encodes all analytic and combinatorial properties of the vertex functions and retains the symmetries of the original action. Truncations of this hierarchy usually violate Ward identities and conservation laws. In the RG approach, the same problem arises, but in addition, the regularization may violate some symmetries explicitly, so that the restoration of Ward identities in the limit where the regulator is removed requires proof. The most important examples of this are theories with local gauge symmetries, e.g., QED [54, 55].

A general theory of conserving approximations was developed by Baym and Kadanoff [56, 57] in the context of many-body theory, and later also used in high-energy quantum field theory [58]. An essential object there is the Luttinger-Ward (LW) functional, which expresses the grand canonical potential as a function of the bare vertex and the full propagator of the theory. The field equations are obtained by a stationarity condition as the propagator is varied. Similar constructions using the self-energy as the variational parameter instead of the propagator were introduced by Potthoff [59, 60].

It is a natural question whether there is a scale-dependent variant of this functional, in which both the full scale-dependent propagator and the effective two-particle vertex (instead of the bare one) appear. Here we define a functional which has these properties, in terms of an expansion in powers of the effective two-particle vertex. In principle, the iteration of the RG equations in their integral form (in a procedure generalizing the derivations in Ref. [29]) automatically generates such an expansion. However, the expression for the functional in-

volves integrals over intermediate scales, similarly to the Brydges-Kennedy formula [61], which provides an explicit solution to Polchinski's equation.

Another generalization of the LW functional was given by the Lund group, in which the bare interaction is replaced by the screened interaction using the Bethe-Salpeter equation. The resulting functional is variational in both parameters [62, 63].

1.2 Stationary Point Formulation of the Schwinger-Dyson Equations

Our main goal in this chapter is the derivation of flow equations for the Green's functions for fermions on a lattice. From a practical point of view, the difficulty lies rather in finding a good truncation or an exact formuation that will simplify this task. We seek an exact formulation in orders of the irreducible four-point vertex which can be truncated at different orders to produce a conserving approximation. In order to reduce the numerical complexity, we will also consider simplification in which we trade exact conservation laws for better performance.

To keep the formalism simple, we will use the functional integral formulation for a fermionic field theory on a finite lattice $\mathbb{L}$. At the very end, we take the limits volume to infinity and lattice spacing along the imaginary time axis to zero. In the coordinate space we retain the finite lattice spacing. To keep the notation clean we will absorb prefactors like volume and temperature into the definition of our summation symbol which we denote by the integral symbol $\int_x$. We will specify the definition as soon as we turn our attention to a specific model in the following chapters. A label $x = (k_0, \boldsymbol{k}, \sigma)$ in momentum space is composed of the Matsubara frequency k_0, the momentum $\boldsymbol{k}$ and the spin orientation σ. The summation goes over all variables.

Let ψ_x and $\overline{\psi}_x$ be two Grassmann fields and consider the action

$$S[\psi, \overline{\psi}] = -(\overline{\psi}, C^{-1}\psi) - V[\psi, \overline{\psi}],$$

where C is the propagator of the non-interacting system and V is a two body interaction of the general form

$$V[\psi, \overline{\psi}] = \int_{x_1, x_2, x_1', x_2'} v_{x_1, x_2; x_1', x_2'} \overline{\psi}_{x_1} \overline{\psi}_{x_2} \psi_{x_2'} \psi_{x_1'}.$$

The bilinear form (f,g) is defined as the sum $\int_x f(x)g(x)$. The grand canonical partition function of this system is given by

$$Z[\eta,\overline{\eta}] = \int \mathrm{d}\mu_C \, \mathrm{e}^{V[\psi,\overline{\psi}]} \, \mathrm{e}^{(\overline{\eta},\psi)+(\overline{\psi},\eta)} \,,$$

where $\mathrm{d}\mu_C = \frac{1}{\det C} \prod_x \mathrm{d}\psi_x \, \mathrm{d}\overline{\psi}_x \, \mathrm{e}^{(\overline{\psi},C^{-1}\psi)}$. The connected m-particle Green function $G^{(2m)}$ is obtained from the generator $\mathcal{G} := -\ln Z$ by differentiating with respect to $\eta,\overline{\eta}$ and evaluating for vanishing sources:

$$G^{(2m)}_{x_1,\ldots,x_m;x'_1,\ldots,x'_m} = (-1)^m \frac{\partial^{2m}\mathcal{G}\left[\eta,\overline{\eta}\right]}{\partial\overline{\eta}_{x_1}\ldots\partial\overline{\eta}_{x_m}\partial\eta_{x'_m}\ldots\partial\eta_{x'_1}}\bigg|_{\eta=\overline{\eta}=0} .$$

The Legendre transform of $\mathcal{G}$,

$$\Gamma\left[\psi,\overline{\psi}\right] = (\overline{\eta},\psi) + (\overline{\psi},\eta) + \mathcal{G}\left[\eta,\overline{\eta}\right] \,,$$

with $\psi = -\frac{\partial\mathcal{G}}{\partial\overline{\eta}}$ and $\overline{\psi} = \frac{\partial\mathcal{G}}{\partial\eta}$ defines the generator of the one-particle irreducible (1PI) Green functions $\Gamma^{(2m)}_{x_1,\ldots,x_m;x'_1,\ldots,x'_m}$,

$$\Gamma^{(2m)}_{x_1,\ldots,x_m;x'_1,\ldots,x'_m} = \frac{\partial^{2m}\Gamma\left[\psi,\overline{\psi}\right]}{\partial\overline{\psi}_{x_1}\ldots\partial\overline{\psi}_{x_m}\partial\psi_{x'_m}\ldots\partial\psi_{x'_1}}\bigg|_{\psi=\overline{\psi}=0} .$$

We will formulate the equations we are going to derive in terms of the 1PI Green functions. In the following we will depict a vertex f by

$f_{x_1,\ldots,x_m;x'_1,\ldots,x'_m} \simeq$ 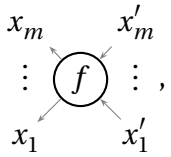

,

and use a heavy line to represent the full propagator G,

$$G_{x_1;x'_1} \simeq x_1 \longleftarrow x'_1 .$$

By integration by parts

$$\int \mathrm{d}\mu_C \psi_x F[\psi,\overline{\psi}] = -\int_y C_{x,y} \int \mathrm{d}\mu_C \frac{\partial}{\partial\overline{\psi}_y} F[\psi,\overline{\psi}] \,, \tag{1.1}$$

every m-particle correlation function obeys a Schwinger-Dyson equation

$$\begin{aligned}\int \mathrm{d}\mu_C \psi_{x_1}\dots\psi_{x_m}\overline{\psi}_{x'_m}\dots\overline{\psi}_{x'_1} e^{V[\psi,\overline{\psi}]} = \\ -\int_y C_{x_1,y}\int \mathrm{d}\mu_C \frac{\partial}{\partial\overline{\psi}_y}\psi_{x_2}\dots\psi_{x_m}\overline{\psi}_{x'_m}\dots\overline{\psi}_{x'_1} e^{V[\psi,\overline{\psi}]}\,.\end{aligned} \tag{1.2}$$

The correlation function on the right-hand side is disconnected, but can be expressed by standard cumulant formulas in terms of the connected Green functions. These, in turn, are given by a standard expansion in trees that have the full propagator $G := G^{(2)}$ associated to lines and the 1PI vertex functions to the vertices . For $m = 1$, Eq. (1.2) results in the following equation for the propagator G,

$$\begin{aligned}G_{x,x'} =& C_{x,x'} - \int_{z_1\cdots z_4} C_{x,z_1} G_{z_4,z_2} v_{z_1,z_2,z_3,z_4} G_{z_3,x'} \\ &-\frac{1}{2}\int_{\substack{z_1\cdots z_4\\ y_1\cdots y_4}} C_{x,z_1} v_{z_1,z_2,z_3,z_4} G_{z_3,y_1} G_{z_4,y_2} \Gamma^{(4)}_{y_1,y_2,y_3,y_4} G_{y_4,z_2} G_{y_3,x'}\,.\end{aligned}$$

We deduce that the self-energy $\Sigma = C^{-1} - G^{-1}$ is given by

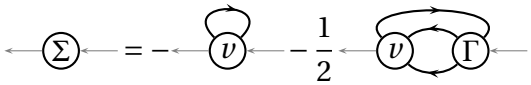

$$\begin{aligned}\Sigma_{x,x'} =& -\int_{z_2,z_4} G_{z_4,z_2} v_{x,z_2,x',z_4} \\ &-\frac{1}{2}\int_{\substack{z_2,z_3,z_4\\ y_1,y_2,y_3}} v_{x,z_2,z_3,z_4} G_{z_3,y_1} G_{z_4,y_2} \Gamma^{(4)}_{y_1,y_2,x',y_4} G_{y_4,z_2}\,.\end{aligned} \tag{1.3}$$

This equation will be referenced numerous times through this thesis. The one-loop contribution is the Hartree term. We will refer to such diagrams as tadpoles. The two-loop contribution is a so-called sunset diagram.

The SD equation for $m = 2$ gives the 4-point vertex (2-particle vertex) as

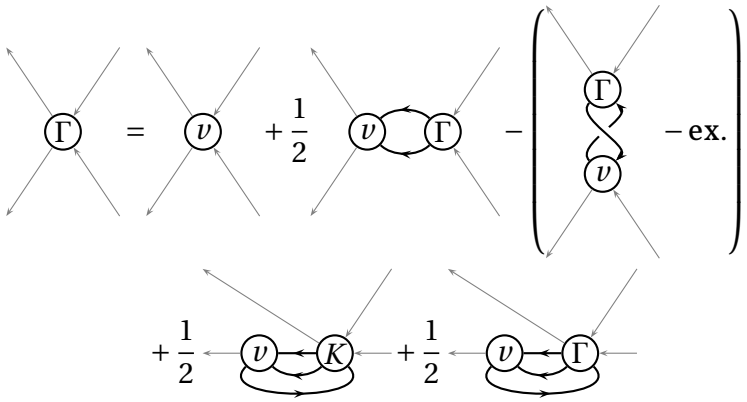

$$
\begin{aligned}
\Gamma^{(4)}_{x_1,x_2;x_1',x_2'} = v_{x_1,x_2;x_1',x_2'} &+ \frac{1}{2}\int\limits_{z_1\cdots z_4} v_{x_1,x_2;z_1,z_2} G_{z_1,z_3} G_{z_2,z_4} \Gamma^{(4)}_{z_3,z_4;x_1',x_2'} \\
&- \left(\int\limits_{z_1\cdots z_4} v_{x_1,z_1;x_3,z_2} G_{z_4,z_1} G_{z_2,z_3} \Gamma^{(4)}_{z_3,x_2;z_4,x_2'} - \left(x_3 \leftrightarrow x_4\right) \right) \\
&+ \frac{1}{2}\int\limits_{z_1\cdots z_6} v_{z_1,x_1;z_2,z_3} G_{z_3,z_5} G_{z_2,z_4} G_{z_6,z_1} K_{z_4,z_5,x_2,z_6,x_1',x_2'} \\
&+ \frac{1}{2}\int\limits_{z_1\cdots z_6} v_{z_1,x_1;z_2,z_3} G_{z_3,z_5} G_{z_2,z_4} G_{z_6,z_1} \Gamma^{(6)}_{z_4,z_5,x_2,z_6,x_1',x_2'} ,
\end{aligned}
\tag{1.4}
$$

where

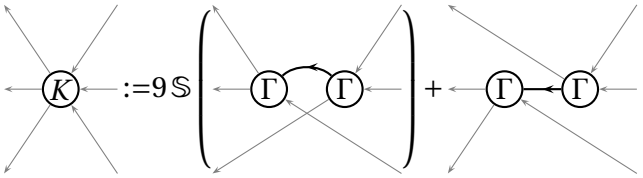

$$
\begin{aligned}
K_{x_1,x_2,x_3;x_1',x_2',x_3'} \coloneqq \quad & 9\,\mathbb{S}_3 \int\limits_{z_1,z_2} \Gamma^{(4)}_{x_2,x_3;x_1',z_1} G_{z_1,z_2} \Gamma^{(4)}_{x_1,z_2;x_2',x_3'} \\
& + \int\limits_{z_1,z_2} \Gamma^{(4)}_{x_1,x_2;x_1',z_1} G_{z_1,z_2} \Gamma^{(4)}_{z_2,x_3;x_2',x_3'} ,
\end{aligned}
\tag{1.5}
$$

and the antisymmetrization operator $\mathbb{S}_m$ projects a function $f_{x_1,\ldots x_m;x_1',\ldots,x_m'}$ to its antisymmetric part

$$
\mathbb{S}_m f_{x_1,\ldots,x_m;x_1',\ldots,x_m'} = \quad \frac{1}{(m!)^2} \sum_{\pi,\pi'\in\mathscr{P}_m} \operatorname{sgn}(\pi)\operatorname{sgn}(\pi') f_{x_{\pi(1)},\ldots,x_{\pi(m)},x'_{\pi'(1)},\ldots,x'_{\pi'(m)}} .
$$

The second term in Eq. (1.5) cancels a contribution from the first term which would otherwise lead to a reducible diagram in Eq. (1.4). Note that Eq. (1.3) for the self-energy and (1.4) for the irreducible vertex are exact. Using Eq. (1.1) the six-point Green function in Eq. (1.4) can be expressed in terms of the bare interaction and the four- and eight-point irreducible vertexes. We will neglect the eight-point 1PI Green function and approximate

$$\begin{aligned}\Gamma^{(6)}_{x_1,x_2,x_3;x_1',x_2',x_3'} \approx & \mathbb{S}\Big(-6\int_{z_1\cdots z_6} v_{x_1,x_2;z_1,z_2}\Gamma^{(4)}_{z_3,x_3;z_4,x_3'}\Gamma^{(4)}_{z_5,z_6;x_1',x_2'}G_{z_1,z_5}G_{z_2,z_3}G_{z_4,z_6}\\ & -3\int_{z_1\cdots z_6}\Gamma^{(4)}_{x_1,x_2;z_1,z_2}v_{z_3,x_3;z_4,x_3'}\Gamma^{(4)}_{z_5,z_6;x_1',x_2'}G_{z_1,z_5}G_{z_2,z_3}G_{z_4,z_6}\Big)\\ \approx & -9\mathbb{S}\int_{z_1\cdots z_6}\Gamma^{(4)}_{x_1,x_2;z_1,z_2}\Gamma^{(4)}_{z_3,x_3;z_4,x_3'}\Gamma^{(4)}_{z_5,z_6;x_1',x_2'}G_{z_1,z_5}G_{z_2,z_3}G_{z_4,z_6}\,.\end{aligned}$$

In the last step we have replaced v by $\Gamma^{(4)}+\mathcal{O}\left(\Gamma^{(4)}\right)^2$, according to Eq. (1.4). Denote the particle–particle bubble propagator by Π,

$$(\Pi_G)_{x_1,x_2;x_1',x_2'} := G_{x_1,x_1'}G_{x_2,x_2'}\,,$$

and the particle–hole bubble propagator by Υ,

$$(\Upsilon_G)_{x_1,x_2;x_1',x_2'} := G_{x_1,x_2'}G_{x_1',x_2}\,,$$

then define

$$(f\circ g)_{x_1,x_2;x_3,x_4} := \int_{z_1,z_2} f_{x_1,x_2,z_1,z_2}g_{z_1,z_2,x_3,x_4}$$

and

$$(f*g)_{x_1,x_2;x_3,x_4} := \int_{z_1,z_2} f_{z_1,x_2,z_2,x_4}g_{x_1,z_1,x_3,z_2}\,.$$

Below we introduce a short notation for a tadpole term, for later use. For a 4-point function f and a 2-point function g we define,

$$g[\![f]\!] := \int_{y,y'} g_{y',y}f_{x,y;x',y'}\,.$$

In this notation we obtain

$$\begin{aligned}\Gamma^{(4)} - v = \Theta := \mathbb{S}\Big\{ & \frac{1}{2}\Gamma^{(4)} \circ \Pi_G \circ \Gamma^{(4)} - 2\Gamma^{(4)} * \Upsilon_G * \Gamma^{(4)} \\ & - \frac{1}{4}\Gamma^{(4)} \circ \Pi_G \circ \Gamma^{(4)} \circ \Pi_G \circ \Gamma^{(4)} - 2\Gamma^{(4)} * \Upsilon_G * \Gamma^{(4)} * \Upsilon_G * \Gamma^{(4)} \\ & + \frac{1}{8}\Gamma^{(4)} \circ \Pi_G \circ \Gamma^{(4)} \circ \Pi_G \circ \Gamma^{(4)} \circ \Pi_G \circ \Gamma^{(4)} \\ & - 2\Gamma^{(4)} * \Upsilon_G * \Gamma^{(4)} * \Upsilon_G * \Gamma^{(4)} * \Upsilon_G * \Gamma^{(4)} \\ & - 4Q(G, \Gamma^{(4)})\Big\} + \mathcal{O}\left(\Gamma^{(4)}\right)^5 ,\end{aligned} \tag{1.6}$$

where we have eliminated v from the right-hand side by means of iteration before truncating the result at the given order in $\Gamma^{(4)}$. The last term $Q(G, \Gamma^{(4)})$ is given by

$$\begin{aligned}(Q(G, \Gamma^{(4)}))_{x_1, x_2; x_3, x_4} := \int\limits_{z_1 \cdots z_{12}} & \Gamma^{(4)}_{x_1, z_1; z_2, z_3} \Gamma^{(4)}_{z_4, x_2; z_5, z_6} \Gamma^{(4)}_{x_7, z_8; x_3, z_9} \Gamma^{(4)}_{z_{10}, z_{11}; z_{12}, x_4} \\ & \cdot G_{z_5, z_1} G_{z_3, z_{10}} G_{z_2, z_7} G_{z_9, z_4} G_{z_6, z_{11}} G_{z_{12}, z_8} .\end{aligned}$$

Eq. (1.6) can be extended to any order, in principle, though the computational effort grows rapidly. For a four–point function f define $\mathscr{C}$ as the operation

$$\mathscr{C}(f) = \int\limits_{x,y} f_{x,y;y,x} ,$$

which consists of closing the diagram and results in a scalar. Then Eq. (1.6) is equivalent to

$$\frac{\mathrm{d}}{\mathrm{d}\Gamma^{(4)}} \mathscr{F}_1(G, \Gamma^{(4)}) = 0 , \tag{1.7}$$

with

$$\begin{aligned}\mathscr{F}_1\left(G, \Gamma^{(4)}\right) = \frac{-1}{4}\mathscr{C}\Big\{ & \frac{1}{2}\left(\Gamma^{(4)} \circ \Pi_G \circ \Gamma^{(4)}\right) - \left(\Gamma^{(4)} \circ \Pi_G \circ v\right) \\ & - \frac{1}{6}\left(\Gamma^{(4)} \circ \Pi_G \circ \Gamma^{(4)} \circ \Pi_G \circ \Gamma^{(4)}\right) - \frac{2}{3}\left(\Gamma^{(4)} * \Upsilon_G * \Gamma^{(4)} * \Upsilon_G * \Gamma^{(4)}\right) \\ & + \frac{1}{16}\left(\Gamma^{(4)} \circ \Pi_G \circ \Gamma^{(4)} \circ \Pi_G \circ \Gamma^{(4)} \circ \Pi_G \circ \Gamma^{(4)}\right) - \frac{1}{2}\left(\Gamma^{(4)} * \Upsilon_G * \Gamma^{(4)} * \Upsilon_G * \Gamma^{(4)} * \Upsilon_G * \Gamma^{(4)}\right) \\ & - \frac{1}{40}\left(\Gamma^{(4)} \circ \Pi_G \circ \Gamma^{(4)} \circ \Pi_G \circ \Gamma^{(4)} \circ \Pi_G \circ \Gamma^{(4)} \circ \Pi_G \circ \Gamma^{(4)}\right) \\ & - \frac{2}{5}\left(\Gamma^{(4)} * \Upsilon_G * \Gamma^{(4)} * \Upsilon_G * \Gamma^{(4)} * \Upsilon_G * \Gamma^{(4)} * \Upsilon_G * \Gamma^{(4)}\right) \\ & + \frac{4}{5}\left(Q(G, \Gamma^{(4)}) \circ \Pi_G \circ \Gamma^{(4)}\right)\Big\} + \mathcal{O}\left(\Gamma^{(4)}\right)^6 .\end{aligned}$$

Note that the components of the gradient, with respect to $\Gamma^{(4)}$ are already antisymmetric. More precisely, we restrict $\Gamma^{(4)}$ to have the desired antisymmetry, meaning that the components of $\Gamma^{(4)}$ are not independent. The total derivative of a functional $F(\Gamma^{(4)})$, with respect to $\Gamma^{(4)}_{x_1,x_2;x_3,x_4}$, is thus given by

$$\frac{\mathrm{d}F(\Gamma^{(4)})}{\mathrm{d}\Gamma^{(4)}_{x_1,x_2;x_3,x_4}} = \frac{\partial F(\Gamma^{(4)})}{\partial\Gamma^{(4)}_{x_1,x_2;x_3,x_4}} - \frac{\partial F(\Gamma^{(4)})}{\partial\Gamma^{(4)}_{x_2,x_1;x_3,x_4}} - \frac{\partial F(\Gamma^{(4)})}{\partial\Gamma^{(4)}_{x_1,x_2;x_4,x_3}} + \frac{\partial F(\Gamma^{(4)})}{\partial\Gamma^{(4)}_{x_2,x_1;x_4,x_3}} .$$

The existence of the functional $\mathscr{F}_1$ with the property (1.7) is nontrivial and very interesting already, but we can go a step further. Let us define $\mathscr{F}_2$ as

$$\begin{aligned}\mathscr{F}_2(G(\Sigma)) = &-\int \mathrm{d}z_1\,\mathrm{d}z_2\, G_{z_2,z_1}\left(C^{-1}\right)_{z_1,z_2} \\ &-\frac{1}{2}\int \mathrm{d}z_1\cdots\mathrm{d}z_4\, v_{z_1,z_2;z_3,z_4} G_{z_3,z_1} G_{z_4,z_2} + \ln\left(\det G\right) ,\end{aligned}$$

and add this $\Gamma^{(4)}$-independent term to $\mathscr{F}_1$, then the stationary point of

$$\mathscr{F}\left(\Sigma,\Gamma^{(4)}\right) := \mathscr{F}_1\left(G(\Sigma),\Gamma^{(4)}\right) + \mathscr{F}_2(G(\Sigma))$$

$$= \ln\det G - \tfrac{1}{2}\,v + \tfrac{1}{8}\,\Gamma\,\Gamma - \tfrac{1}{4}\,v\,\Gamma - \tfrac{1}{24}\,\Gamma\,\Gamma\,\Gamma + \tfrac{1}{6}\,\Gamma\,\Gamma\,\Gamma + \tfrac{1}{64}\,\Gamma\,\Gamma\,\Gamma\,\Gamma + \tfrac{1}{8}\,\Gamma\,\Gamma\,\Gamma\,\Gamma - \tfrac{1}{160}\,\Gamma\,\Gamma\,\Gamma\,\Gamma\,\Gamma + \tfrac{1}{10}\,\Gamma\,\Gamma\,\Gamma\,\Gamma\,\Gamma + \tfrac{1}{5}\,\Gamma\,\Gamma\,\Gamma\,\Gamma + \cdots ,$$

(1.8)

with respect to Σ for some given $\Gamma^{(4)}$ is a solution of Eq. (1.3). Since $\mathscr{F}_2$ is independent of $\Gamma^{(4)}$ we conclude that the solution of Schwinger-Dyson equations (1.3) and (1.6) is a stationary point of $\mathscr{F}$, i.e.,

$$\begin{gathered}\frac{\mathrm{d}}{\mathrm{d}\Sigma}\mathscr{F}\left(\Sigma,\Gamma^{(4)}\right)=0 \quad \text{or} \quad \frac{\mathrm{d}}{\mathrm{d}G}\mathscr{F}\left(\Sigma,\Gamma^{(4)}\right)=0\,,\\ \frac{\mathrm{d}}{\mathrm{d}\Gamma^{(4)}}\mathscr{F}\left(\Sigma,\Gamma^{(4)}\right)=0\,.\end{gathered} \tag{1.9}$$

We can also write the first equation in the following way,

$$\Sigma_{x,x'}=\frac{\mathrm{d}\Phi}{\mathrm{d}G_{x',x}}\,,$$

where $\Phi \coloneqq -\frac{1}{2}\mathscr{C}(v\circ\Pi_G)+\mathscr{F}_1$. Hence the self-energy is Φ-derivable and it will remain so even when we truncate the functional $\mathscr{F}$ at a specific order in $\Gamma^{(4)}$. This is of great importance due to a theorem by Baym and Kadanoff which states that If and only if an approximate self-energy is Φ-derivable, the approximation is conserving [56, 57].

In summary, we have obtained a new saddle-point description of equations of motion in terms of the 1PI vertex and full propagator, which we can use to construct conserving approximations. We have checked that at least one further order of the functional $\mathscr{F}$ exists but it becomes too lengthy to be presented here. From a numerical point of view the equations are challenging. In the next chapter we will consider both a simple model where we can solve them directly and a compromise between computational cost and accuracy for more general cases. It is a natural idea to use flow equations as an alternative to iterative methods to solve self-consistency equations. Iterative methods in particular may suffer from three sources of convergence problems: the singular nature of the integral equations of unscaled SDE, divergence under iteration and convergence to a non-physical saddle point solutions. While we do not find it likely that using a flow equation will reduce the numerical cost generically, we do expect that some issues of convergence of iterations encountered may be avoided in an RG flow toward the solution of these equations.

We will show that the resummed SD equations are closely related to the well-known and very successful Katanin scheme. Our derivation allows further improvements to be included systematically, as desired. We refer to the hierarchy of fRG schemes derived in this way as *Schwinger-Dyson Renormalization Group* (SDRG).

1.3 Schwinger-Dyson Renormalization Group

Assume that $C = C_\Lambda$ depends differentiably on a parameter Λ, the SD equations (1.3), and (1.4) determine Λ-dependent self-energies Σ_Λ and two-particle vertices $\Gamma^{(4)}_\Lambda$, etcetera. Following the standard convention in fRG studies of condensed-matter systems, we arrange things so that for some value Λ_0 of Λ (the *starting scale*), the vertex functions are given by the bare ones, and the full correlation functions are recovered as $\Lambda \to 0$. Usually this is done by introducing a multiplicative regulator χ_Λ,

$$\chi_\Lambda \sim \begin{cases} 0 & \text{for} \quad \Lambda \to \Lambda_0 \\ 1 & \text{for} \quad \Lambda \to 0 \end{cases} ,$$

into the free propagator. We assume that Σ_Λ and $\Gamma^{(2m)}_\Lambda$ are differentiable functions of Λ as well and derivatives with respect to Λ can be exchanged with the summations occurring in the SDE. Note that this is an assumption on the solution of the hierarchy, which will in general contain singular functions in the limit $\Lambda \to 0$, hence checking it is important and nontrivial. However, for the standard momentum space cutoff RG, it has been proven [64, 65], and this proof extends to any RG flow that imposes a sufficient regularization on C, in particular the temperature RG flow [66] and the Ω-regularization [67]. Thus the assumption is satisfied in a large class of flows, for which the SDE holds at every scale Λ.

We have chosen to make C, but not V depend on Λ because we want to draw a connection between SDE and standard functional RG flows, and this choice of Λ-dependence is the same as in the derivation of the functional RG equation in [65, 24, 27]. One can think of many other useful ways in which a parameter Λ could be introduced in the SDE, such as in the interaction (or only there). A natural way to check the differentiability assumption is then to truncate the SDE hierarchy at successive levels, and within each truncation verify the differentiability conditions by analysis of the right-hand side of the flow equation.

To avoid overloading the notation we drop the subscript Λ from $\Gamma^{(4)}_\Lambda$, Σ_Λ and G_Λ. Consider the functional $\mathscr{F}$ truncated at the order $\left(\Gamma^{(4)}\right)^3$,

$$\begin{aligned}\mathscr{F}_{\text{trunc.}}\left(G,\Gamma^{(4)}\right) = \mathscr{F}_1 + \frac{-1}{4}\mathscr{C}\Big\{ &\frac{1}{2}\left(\Gamma^{(4)} \circ \Pi_G \circ \Gamma^{(4)}\right) - \left(\Gamma^{(4)} \circ \Pi_G \circ v\right) \\ &- \frac{1}{6}\left(\Gamma^{(4)} \circ \Pi_G \circ \Gamma^{(4)} \circ \Pi_G \circ \Gamma^{(4)}\right) - \frac{2}{3}\left(\Gamma^{(4)} * \Upsilon_G * \Gamma^{(4)} * \Upsilon_G * \Gamma^{(4)}\right)\Big\}.\end{aligned}$$

our saddle point equations (1.9), are then given by

$$\Gamma^{(4)} = v + \mathbb{S}\Big\{\frac{1}{2}\Gamma^{(4)} \circ \Pi_G \circ \Gamma^{(4)} - 2\Gamma^{(4)} * \Upsilon_G * \Gamma^{(4)}\Big\}, \tag{1.10a}$$

$$\Sigma = -G[\![v]\!] - \frac{1}{2} G[\![v \circ \Pi_G \circ \Gamma^{(4)}]\!]. \tag{1.10b}$$

Taking the derivative of Eq. (1.10a) with respect to Λ (denoted here by a dot and written out explicitly only in the particle-particle channel),

$$\begin{aligned}\dot{\Gamma}^{(4)}_{x_1,x_2;x_1',x_2'} =& \frac{1}{2}\sum_{z_1\cdots z_4} \Gamma^{(4)}_{x_1,x_2;z_1,z_2} \frac{\mathrm{d}}{\mathrm{d}\Lambda}\Big(G_{z_1,z_3}G_{z_2,z_4}\Big)\cdot\Gamma^{(4)}_{z_3,z_4;x_1',x_2'} \\ &+ \frac{1}{2}\sum_{z_1\cdots z_4} \dot{\Gamma}^{(4)}_{x_1,x_2;z_1,z_2} G_{z_1,z_3}G_{z_2,z_4}\cdot\Gamma^{(4)}_{z_3,z_4;x_1',x_2'} + \\ &+ \frac{1}{2}\sum_{z_1\cdots z_4} \Gamma^{(4)}_{x_1,x_2;z_1,z_2} G_{z_1,z_3}G_{z_2,z_4}\cdot\dot{\Gamma}^{(4)}_{z_3,z_4;x_1',x_2'} + + \cdots,\end{aligned} \tag{1.11}$$

gives rise to terms on the right-hand side where only propagators are differentiated, and ones where $\dot{\Gamma}^{(4)}_{\Lambda}$ appears. At each order in an expansion in $\Gamma^{(4)}$, it is possible to eliminate v and $\dot{\Gamma}^{(4)}$ from the right-hand side of Eq. (1.11) by substituting v from Eq. (1.10a) and iterating Eq. (1.11). This results in

$$\dot{\Gamma}^{(4)}_{x_1,x_2;x_1',x_2'} = \frac{1}{2}\sum_{z_1\cdots z_4} \Gamma^{(4)}_{x_1,x_2;z_1,z_2}\left(\frac{\mathrm{d}}{\mathrm{d}\Lambda}G_{z_1,z_3}G_{z_2,z_4}\right)\Gamma^{(4)}_{z_3,z_4;x_1',x_2'} - (\text{ph.}-\text{ex.}) + \mathscr{O}\left(\Gamma^{(4)}\right)^3. \tag{1.12}$$

Taking the Λ-derivative of Eq. (1.10b), after some trivial simplification, gives

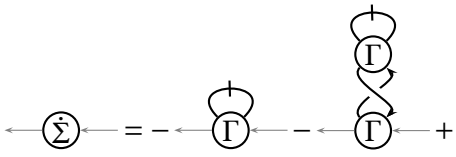

(1.13)

which is up to $\mathscr{O}\left(\Gamma^{(4)}\right)^3$ equivalent to

$$\dot{\Sigma} = -S[\![\Gamma^{(4)}]\!], \tag{1.14}$$

where $S = \dot{G} + G\dot{\Sigma}G$ is the single-scale propagator appearing in the standard RG equations for the irreducible vertex functions [24, 27]. The lowest order Schwinger-Dyson flow equations (1.12,1.14) coincide with Katanin's truncation

[28] of the RG hierarchy. Originally it was introduced as a modification to the 1PI scheme to improve the fulfillment of Ward identities. In our derivation it arises naturally from the SD equations and can be generalized to higher order equations systematically (see appendix A). Katanin's equations are not exactly conserving. We lost this property at the point where we replaced $\dot{\Gamma}^{(4)}$ on the right-hand side of $\dot{\Sigma}$ (with Σ given by Eq. (1.10b)) with an approximation in terms of a finite series in $\Gamma^{(4)}$. At one loop level, as presented here, their solution fulfills Ward identities up to the third order in the full interaction vertex [28].

Whether two loop and higher order contribution to the flow of the four-point vertex can be neglect or not depend on the initial interaction and the geometry of the Fermi surface. For smooth and curved Fermi surfaces, they can be shown to be small, at least in a specific scale range, due to phase space bounds. The presence of van Hove singularities makes the bounds tighter and reduce the scale range in which the one loop contributions dominate [68]. vHS also play a large role in the frequency behavior of the self-energy [69, 70]. Note that Katanin's truncation includes contributions from sunset diagrams with two full vertices; to be more precise they cancel exactly so that the error in Eq. (1.14) is of third order in $\Gamma^{(4)}$ (see also Section 5.1). Alternatively the self energy can be computed from the exact Eq. (1.3).

Chapter 2

Two-Patch Model Revisited: Schwinger-Dyson versus Katanin's Equations

2.1 Introduction

In Chapter 1 we derived self-consistent saddle point equations (1.9) for fermionic systems. Even in the simplest approximation, i.e. neglecting the self-energy and truncating the vertex equation at one loop, the resulting equation (1.10a) is generally tough to solve. Besides the physical solution this equation has many other non-physical solutions and the difficulty of picking the physical solution goes far beyond finding all solutions. This shall become clear as we proceed.

In the case of the Hubbard model we will revise the two-patch model. The main feature of the model in the reduction of the full interaction vertex to four couplings. These four couplings arise under the assumption that at van Hove filling the interaction between electron states near the saddle points will generate the dominant instabilities. The RG-flow of the couplings have been studied with a momentum cutoff in the past. Schulz [32] and Dzyaloshinskii [33] have studied the special case of a square Fermi surface. In summary, at half filling perfect nesting leads to antiferromagnetic oder while a superconduction transition may occur for non-half-filled band. The Hubbard model with finite nearest-neighbor hopping has been considered by Lederer et al. [34], Dzyaloshinskii [35], Furukawa, Honerkamp, Salmhofer and Rice [36, 37]. Finally, the Phase diagram of the U-V-J model has been studied by Kampf and Katanin [38].

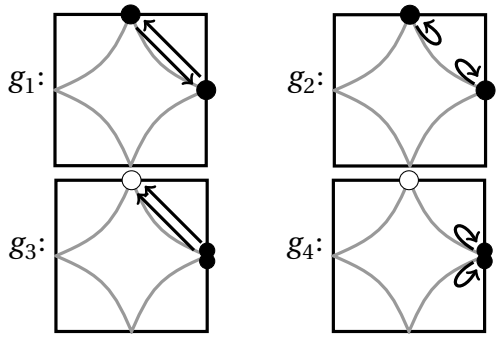

Figure 2.1: Schematic representation of the couplings. The most relevant scattering processes are assumed to be those between states near vHS. The couplings are assumed to be spin-independent. In this notation the initial and final particles are connected by an arrow and have the same spin.

The main advantage of the two-patch model is its simplicity. It allows us to study the Hubbard model using Schwinger-Dyson equations. RG result provide bases for comparison and the intuitive couplings of this patching scheme have always been useful for understanding the phenomenology of competing orders in the Hubbard model.

On a square lattice one expects the momenta in the vicinity of the van Hove singularities $a = (0, \pi)$, $b = (\pi, 0)$ to be the most important ones for the calculation of the interaction vertex. The two-patch model then consists of parameterizing the renormalized interaction vertex $\Gamma^{(4)}$ in terms of the four coupling g_k. The associated scattering processes are shown in Figure 2.1. The precise definition is given in appendix B. Note that normal and umkapp processes cannot be distinguished here.

To keep the focus on the current topic, we keep the setup brief and delay certain technical aspects to the next chapter. Here we plan to add a small nearest-neighbor interaction V to the Hubbard Hamiltonian to test the stability of the solutions. The full Hamiltonian is then given by

$$\mathscr{H} = \sum_{x,y} \sum_{\sigma} \hat{c}^{\dagger}_{x,\sigma} \hat{t}(x,y) \hat{c}_{y,\sigma} + U \sum_{x} n_{x,+} n_{x,-} + \frac{V}{2} \sum_{\langle xy \rangle} \sum_{\sigma,\sigma'} n_{x,\sigma} n_{y,\sigma'} ,$$

which in momentum space translates to

$$H = \sum_p \sum_\sigma \epsilon(\boldsymbol{p}) c^\dagger_{p,\sigma} c_{p,\sigma} \\ - \frac{1}{2L^4} \sum_{p_1,p_2,p_3,p_4} \sum_{\sigma,\sigma'} v(p_1,p_2;p_3,p_4) c^\dagger_{p_1,\sigma} c^\dagger_{p_2,\sigma'} c_{p_3,\sigma} c_{p_4,\sigma'} \delta_{p_1+p_2-p_3-p_4} .$$

With a nearest-neighbor hopping parameter t and a next-nearest-neighbor hopping amplitude t', the dispersion ϵ is given by

$$\epsilon(\boldsymbol{p}) = -2t\Big(\cos p_x + \cos p_y\Big) + 4t'\Big(\cos p_x \cos p_y + 1\Big) ,$$

and the bare interaction v is give by

$$v(p_1,p_2;p_3,p_4) = U + 2V f(\boldsymbol{p}_2 - \boldsymbol{p}_4) ,$$

where $f(\boldsymbol{p}) = 2\Big(\cos p_x + \cos p_y\Big)$. The bare values of the couplings g_i denoted by v_i are then given by

$$\begin{aligned} v_1 &= U - 4V , \\ v_2 &= U + 4V , \\ v_3 &= U - 4V , \\ v_4 &= U + 4V . \end{aligned}$$

In the following we will present several equations for the couplings $g_1 \dots g_4$ and compare the solutions. We will assume that the bare propagator includes some infrared regulating function, i.e. (c.f. 1.3)

$$C_\Omega(p) = \frac{\chi_\Omega(p)}{\mathrm{i}\omega - \epsilon(\boldsymbol{p})} ,$$

with

$$\chi_\Omega(p) \sim \begin{cases} 1 & \text{for} \quad \Omega \to 0 \\ 0 & \text{for} \quad \Omega \to \infty \end{cases} .$$

This might seem unnecessary at first glance but in the simplest case it provides us with a tool to overcome the divergence of the particle-particle and particle-hole bubbles at zero frequency and temperature by carefully taking the $\Omega \to 0$ limit. Generally due to the truncation the limit might not exist. A divergence at

some intermediate scale usually signals some instability, such as a broken symmetry. From a mean-field point of view a finite ferromagnetic, antiferromagnetic and superconducting gap becomes possible when the corresponding exchange propagator

$$\begin{aligned} B_{\mathrm{F}} &= g_1 + g_4 \,, \\ B_{\mathrm{AF}} &= g_2 + g_3 \,, \\ B_{\mathrm{dSC}} &= g_3 - g_4 \,, \end{aligned} \tag{2.1}$$

is positive and large enough.[1] A coexistence of anti-ferromagnet and superconductor is possible while the ferromagnet driven by a large coupling g_4 rules out a superconducting phase. The regularization will also prove to be very useful in identifying the physical solution, which will be explained in the following. For the numerical computation we will rely on the frequency based regulator [67],

$$\chi_\Omega(p) = \chi_\Omega(p_0) = \frac{p_0^2}{p_0^2 + \Omega^2} \,,$$

where Ω denotes the scale. The couplings take their bare values in the limit $\Omega \to \infty$.

2.2 Saddle-Point Equations

We begin with the SD equation (1.10a) written in terms of the 1PI vertex neglecting terms of order $\left(\Gamma^{(4)}\right)^3$ and higher. This truncation lead to the following

[1] The corresponding mean-field Hamiltonian is in every case given by

$$H = \sum_{\boldsymbol{k},\sigma} \epsilon(\boldsymbol{k}) \hat{c}^\dagger_{\boldsymbol{k},\sigma} \hat{c}_{\boldsymbol{k},\sigma} + \sum_{\boldsymbol{k}} \Delta_X \hat{O}_X(\boldsymbol{k}) + \frac{\Delta_X}{B_X}$$

where Δ_X is the gap parameter and $\hat{O}_X$ is the Fourier transform of a fermionic bilinear

$$\hat{O}_{\mathrm{F}}(i) = \frac{1}{2}\sum_\sigma \sigma \hat{c}^\dagger_{i,\sigma}\hat{c}_{i,\sigma} \quad , \quad \hat{O}_{\mathrm{AF}}(i) = \frac{(-)^{(i_x+i_y)}}{2}\sum_\sigma \sigma \hat{c}^\dagger_{i,\sigma}\hat{c}_{i,\sigma} \quad , \quad \hat{O}_{\mathrm{dSC}}(i) = \frac{1}{8}\sum_{j,\sigma} \sigma \lambda_{i,j} \hat{c}^\dagger_{i,\sigma}\hat{c}_{j,-\sigma} \,,$$

where $\lambda_{ij} = 1(-1)$ for $j = i \pm \delta_x(\delta_y)$. The gap parameter is related to the expectation value of these operators through $\Delta_X = \langle O_X \rangle B_X$. For in depth mean-field analysis of the Hubbard model at van Hove filling see Chapter 4.

system of equations,

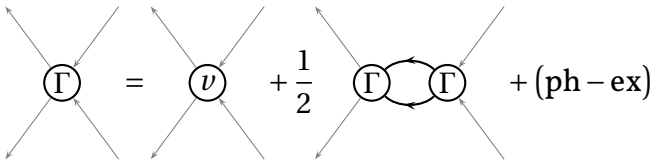

$$
\begin{aligned}
g_1 &= v_1 + 2b_4 g_1(g_1 - g_2) + 2b_2 g_1 g_2 - 2b_3 g_1 g_4 \,, \\
g_2 &= v_2 + b_2(g_1^2 + g_2^2) + b_4(-g_2^2 - g_3^2) + 2b_3(-g_1 + g_2) g_4 \,, \\
g_3 &= v_3 + 2b_4(g_1 - 2g_2) g_3 + 2b_1 g_3 g_4 \,, \\
g_4 &= v_4 + b_3(-g_1^2 + 2g_2(-g_1 + g_2) - g_4^2) + b_1(g_3^2 + g_4^2) \,.
\end{aligned}
\tag{2.2}
$$

The b_i correspond to the particle-particle and particle-hole bubble integrals,

$$
\begin{aligned}
b_1 &= \tfrac{1}{2}\Pi^{\mathrm{pp}}(0,0) \,, \\
b_2 &= \tfrac{1}{2}\Pi^{\mathrm{pp}}(\pi,\pi) \,, \\
b_3 &= \tfrac{1}{2}\Pi^{\mathrm{ph}}(0,0) \,, \\
b_4 &= \tfrac{1}{2}\Pi^{\mathrm{ph}}(\pi,\pi) \,,
\end{aligned}
\tag{2.3}
$$

at zero frequency. The bubbles are given by

$$
\Pi^{\mathrm{ph/pp}}(\boldsymbol{q}) = \pm \int_p C_\Omega(p) C_\Omega(\pm(p - \underline{q}))
$$

where $\underline{q} = (0, \boldsymbol{q})$. In this convention the signs have been chosen such that $b_i \geq 0$. The projection of the momenta in the Brillouin zone the to only two representative points $(0,0)$ or (π,π) simplifies the loop integration to the product between a bubble b_i and a quadratic term $g_k g_l$. Thus we end up with a system of four quadratic equations. See appendix B for details on derivation of Eq. (2.2).

At any scale Ω, Eq. (2.2) has $2^4 = 16$ solutions. Due to time reversal symmetry the interaction vertex should be a real quantity. This criterion can be used to rule out some of the non-physical solutions but it is usually not enough to identify the single physical one. In order to identify the physical solution we have to solve the equations for many intermediate scales and follow the trajectories of the couplings to limit $\Omega \to \infty$. In this limit the physical couplings converge to their bare values. Alternatively one can take a different limit, for example $U, V \to 0$ and choose the solution with vanishing couplings. The computational complexity remains the same.

A different approach for solving Eq. (2.2) consists of taking the derivative with respect to the scale parameter Ω, solving for $\dot{g}_i$ and then seeking the solution of the resulting differential equations using the v_i as initial conditions for the couplings g_i. At the stopping scale, the derivatives $\dot{g}_i$ diverge as in the previous approach the real valued physical solution would turn complex. In the case of the two patch model we can explicitly solve for $\dot{g}_i$ to obtain explicit ordinary differential solutions, but this is not possible in more complex patching schemes, which require other approximations, such as Katanin's scheme.

We proceed with the first method. Figure 2.2 shows the result for different values of the hopping parameter t'/t at van Hove filling for $U = 3t, V = 0t$. All real solution are shown in the plots. The thick solid curves are those satisfying $g_i \to v_i$ in the limit $\Omega \to \infty$. We observe that at some finite scale physical solutions stop to exist. At this point the solution branch turns complex. Even though the complex solution might become real again at smaller scales, as in the case of $t'/t = 0.33$, we will not consider it to be reliable or physical anymore. Thus, we define the largest scale at which a solution develops a nonzero imaginary part to be the stopping scale.

At $t'/t = 0.25$ growing couplings g_2, g_3 and declining g_4 signal antiferromagnetic and superconducting tendencies. At $t'/t = 0.45$ we see a clear trend toward ferromagnetic ordering as g_1 and g_4 significantly surpass other couplings. As we approach $t'/t = 0.34$ from smaller hopping parameters we observe how the gap generated by instabilities separating the two real peaces of the physical solution branch closes. At the critical hopping $t'/t = \theta^\star \approx 0.34$ the physical solution extents to arbitrary small scales and the limit $\Omega \to 0$ can be taken. Furthermore, all couplings remain small which signals a quantum critical point in agreement with previous results [42, 48].

The stopping scales we obtained for the two-patch model away from the QCP are rather large compared to more accurate computations. This is probably caused by the overestimation of the bubble integrals b_i as a result of projecting all momenta to van Hove points.

More sophisticated fRG studies show that unless the self-energy is taken into account it is not possible to take the limit $\Omega \to 0$ without encountering instabilities. The role of the self-energy on gap formation will be discussed in detail in Chapter 4. In the two-patch approximation this is possible both in the

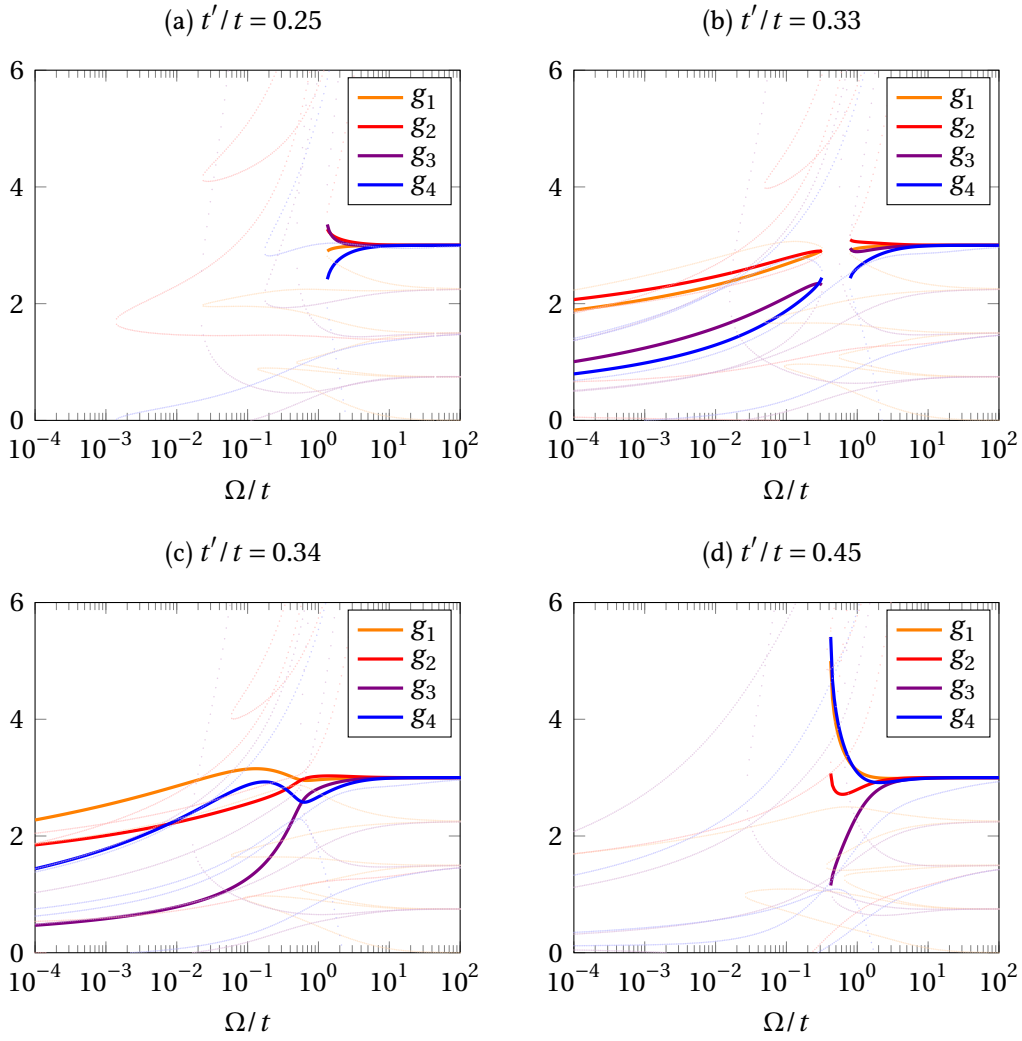

Figure 2.2: Real solutions of Eq. (2.2) for $U/t = 3, V/t = 0$ and for different values of the hopping parameter t'/t. The solid curves show the physical solutions where the couplings g_i fade to their bare values $v_i/t = 3$ in the limit $\Omega \to \infty$. The physical solution extents to arbitrary small scales in the vicinity of $t'/t = \theta^\star \approx 0.34$ which signals a quantum critical point.

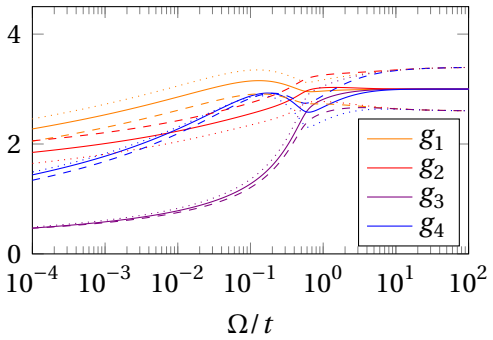

Figure 2.3: The stability of the QCP is tested by adding a small nearest-neighbor interaction $V = \pm 0.1t$ to the Hubbard model $(t'/t = 0.34, U/t = 3)$. The solid curves correspond to $V = 0t$, the dashed ones to $V = +0.1t$ and the dotted ones to $V = -0.1t$. The solutions remain stable and the QCP persists.

saddle-point and in Katanin's scheme for small enough bare interactions but should be considered as an artifact of this very simple patching-scheme. We test the stability of the solution at the critical hopping when the nearest-neighbor interaction V is switched on. The solutions corresponding to $U = 3t, V = \pm 0.1t$ are shown in Figure 2.3. Despite the added perturbation, the solutions remain stable and we can take the $\Omega \to 0$ limit.

2.3 Comparison to Schwinger-Dyson and Katanin's Flow Equations

We will compare the solutions obtained in the last section to those in two other truncations. First we consider the SD equation truncated at one loop, i.e.

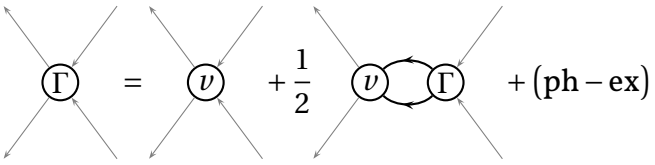

$$
\begin{aligned}
g_1 &= v_1 + b_4\left(2g_1v_1 - g_2v_1 - g_1v_2\right) + b_2\left(g_2v_1 + g_1v_2\right) + b_3\left(-g_4v_1 - g_1v_4\right), \\
g_2 &= v_2 + b_2\left(g_1v_1 + g_2v_2\right) + b_4\left(-g_2v_2 - g_3v_3\right) + b_3\left(-g_4v_1 + g_4v_2 - g_1v_4 + g_2v_4\right), \\
g_3 &= v_3 + b_4\left(g_3\left(v_1 - 2v_2\right) + \left(g_1 - 2g_2\right)v_3\right) + b_1\left(g_4v_3 + g_3v_4\right), \\
g_4 &= v_4 + b_3\left(-\left(g_1 + g_2\right)v_1 - \left(g_1 - 2g_2\right)v_2 - g_4v_4\right) + b_1\left(g_3v_3 + g_4v_4\right).
\end{aligned}
\tag{2.4}
$$

Second, 1PI-flow equation in Katanin's scheme,

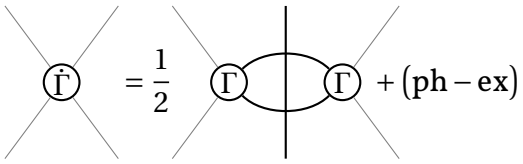

$$\begin{aligned}
\dot{g}_1 &= 2\dot{b}_4 g_1(g_1 - g_2) + 2\dot{b}_2 g_1 g_2 - 2\dot{b}_3 g_1 g_4 \,, \\
\dot{g}_2 &= \dot{b}_2(g_1^2 + g_2^2) + \dot{b}_4(-g_2^2 - g_3^2) + 2\dot{b}_3(-g_1 + g_2)g_4 \,, \\
\dot{g}_3 &= 2\dot{b}_4(g_1 - 2g_2)g_3 + 2\dot{b}_1 g_3 g_4 \,, \\
\dot{g}_4 &= \dot{b}_3(-g_1^2 + 2g_2(-g_1 + g_2) - g_4^2) + \dot{b}_1(g_3^2 + g_4^2) \,,
\end{aligned} \tag{2.5}$$

with initial conditions $\lim_{\Omega\to\infty} g_i = v_i$. The derivative with respect to the scale Ω is denoted by a dot. The truncation (2.4) is linear in g_i. In comparison to Eq. (2.2), the solution is unique, but it might be singular at some intermediate scales. Form a perturbative point of view Equations (2.4) and (2.2) are equivalent in the small v_i limit. More precisely the solution of these equations are the same up to $\mathcal{O}(v^2)$. Equations (2.5) can be derived from the system of quadratic equations (2.2) by taking the derivative with respect to Ω and dropping all term involving derivatives of the couplings on the right-hand side (c.f. Eq. (1.12)). From an analytic point of view these terms are of order g^2 and can be neglected when the couplings are small enough. As soon as the derivatives $\dot{g}_i$ become large we can expect a strong deviation between the solutions of Eq. (2.2) and Eq. (2.5). For intermediate interaction strengths we cannot simply conclude that the quadratic system is the best for summing up more diagrams. One has to consider that the neglected rest terms in all cases are of the same order of magnitude when expressed in powers of g or v. One has to check whether higher loop contributions in each case are small in the region of interest (see for example [68]). Note that only if self-energy is included, the saddle-point truncation will benefit from the fulfillment of the Ward identities (please refer to Chapter 1 for details).

Figure 2.4 shows the couplings in different truncations compared to each other for the critical hopping $t'/t = \theta^\star = 0.34$ and $U = 3t, V = 0t$. The solution of the linear Eq. (2.4) diverges rather quickly. The linear approximation might be good for identifying instabilities (in fact the approximation is similar to a ladder or random phase approximation when a specific bubble becomes dominant), but it does not seem to be suitable for investigating physics in the vicinity of a QCP. The solution of Eq. (2.5) deviates from our reference, i.e. the solution of Eq. (2.2), but it follows its trends. This simple example shows that the neglected terms involving derivatives of the couplings are not necessarily small. According to Chapter 1 the difference between these solutions would ensure the fulfillment of Ward identities if we would include the self-energy. Thus a stronger deviation between these solutions suggest a quantitatively significant violation of conservation laws.

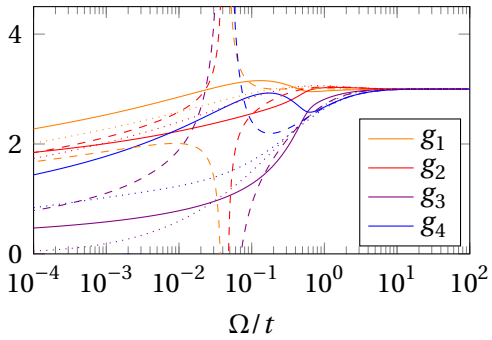

Figure 2.4: A comparison of solutions for $t'/t = 0.34, U/t = 3, V/t = 0$ in different truncations. The solid curve shows the physical solution of the system of quadratic equations (2.2), the dashed curves the solution of linear system of equations (2.4) and the dotted curves the solution of flow equations (2.5).

2.4 The Relation Between the Particle-Hole Bubble and the QCP

Due to its simplicity the two-patch model is a perfect candidate to investigate the phenomenology of the mechanisms leading to a QCP in the phase diagram of the Hubbard model. Since we have a phase transition at the QCP we compute the exchange propagators defined in Eq. (2.1). As noted a positive valued exchange propagator opens the possibility of a finite gap. In the limit $\Omega \to \infty$, B_{F} and B_{AF} start their flow with the positive initial value $2U$ while B_{dSC} is zero at the beginning. The evolution of the exchange propagators as a function of the scale parameter Ω is shown in Figure 2.5. For $t'/t = 0.33$ smaller than the critical hopping amplitude all exchange propagators are positive at the stopping scale. The anti-ferromagnetic coupling is known to function as a driving force for the superconducting tendencies so it is not surprising that B_{AF} and B_{dSC} grow together to some extent. At the critical hopping all couplings remain small. For $t'/t = 0.45$, a superconductor can be ruled out and the ferromagnet dominates.

As the phase transition happens we observe a sign change in B_{dSC} which encodes the ability of the system to be superconducting, according to Eq. (2.2),

$$\begin{aligned} B_{\mathrm{dSC}} = g_3 - g_4 = v_3 - v_4 - \frac{1}{2}\Pi^{\mathrm{pp}}(0,0)\big(g_3 - g_4\big)^2 \\ + \Pi^{\mathrm{ph}}(\pi,\pi)\big(g_1 - 2g_2\big)g_3 - \frac{1}{2}\Pi^{\mathrm{ph}}(0,0)\Big(-g_1^2 + 2g_2(-g_1 + g_2) - g_4^2\Big). \end{aligned}$$

Thus, the position of the QCP is closely related to the competition between $\Pi^{\mathrm{ph}}(0,0)$ and $\Pi^{\mathrm{ph}}(\pi,\pi)$. The difference is plotted in Figure 2.6. We expect the QCP to be located roughly where the contributions cancel and $B_{\mathrm{dSC}} \approx 0$.

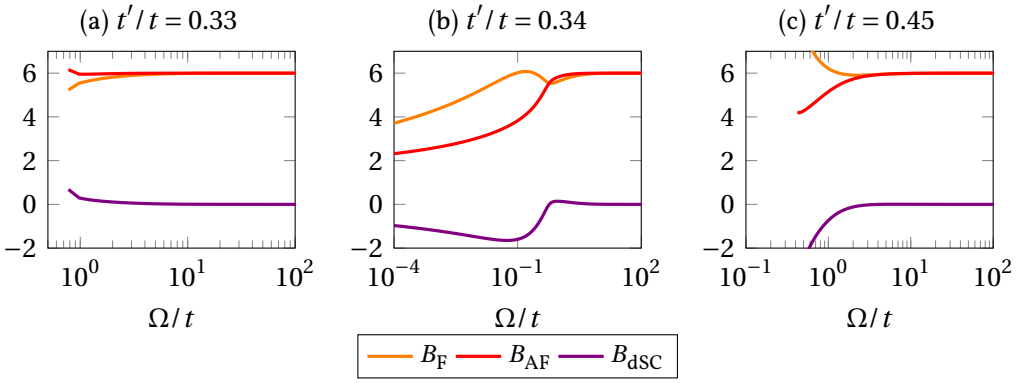

Figure 2.5: Exchange propagators defined in Eq. (2.1) as a function of scale based on the physical solution of Eq. (2.2).

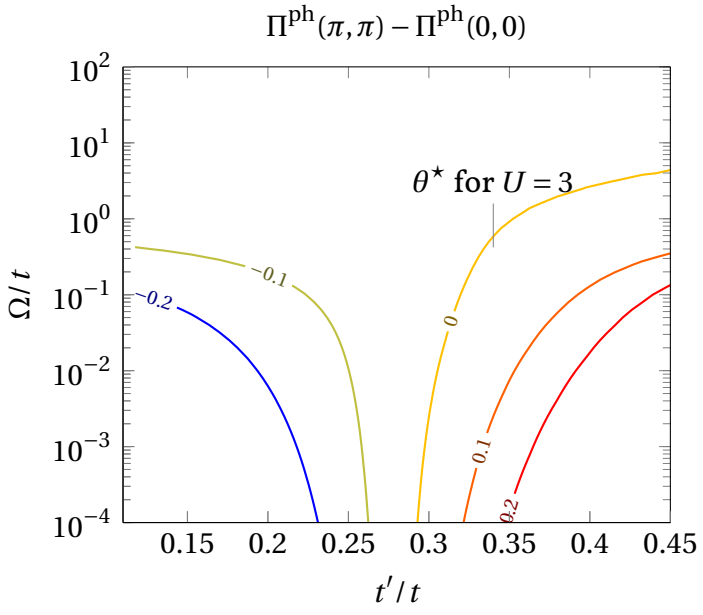

Figure 2.6: The difference $B^{\mathrm{ph}}(\pi,\pi) - B^{\mathrm{ph}}(0,0)$ as a function of hopping parameter t'/t and scales Ω. The QCP is roughly where the bubble contributions cancel out.

2.5 Final Remarks

A comparison of the solutions of saddle-point equations with the linear system of Schwinger-Dyson equations and Katanin's flow equations shows that the saddle-point formalism captures the physics around the QCP point very well. In the saddle-point formalism we can compute the solution beyond the stopping scale. As a result we can see traits of a QCP in a very unique way. For example in Figure 2.2.b at $t'/t = 0.33$ The QCP announces itself as the instabilities interrupt the physical solution only across a small scale interval.

With the inclusion of the self-energy, the saddle-point equations (1.9) have the advantage of being self-consistent, but at the cost of increased computational complexity compared to Katanin's flow equations. In a N-patch representation the equations will have 2^N solutions. When taking a direct approach, both solving the equations and finding the physical solution is difficult. For the general case we have tried an iterative solver. We start at a large scale Ω where the couplings $\boldsymbol{g}_\Omega$ are known, we then decrease the scale gradually and update the solution by means of iteration, i.e.

$$\boldsymbol{g}_{\Omega'}^{(n+1)} = f(\boldsymbol{g}_{\Omega'}^{(n)}),$$

starting with $\boldsymbol{g}_{\Omega'}^{(0)} = \lim_{n\to\infty} \boldsymbol{g}_{\Omega}^{(n)}$ for $\Omega' = \Omega - \mathrm{d}\Omega$. However, this method is not reliable because of convergence problems and the possibility of leaving the physical solution trajectory. One can avoid unphysical solutions by solving a differential equation starting with physical (bare) coupling but the equations would incorporate bubble integrals involving derivatives of the 1PI vertex on the right-hand side. These kind of implicit differential equations are tough to solve. The inclusion of the self-energy will increase the difficulties further. Katanin's scheme remains the method of choice, as long as the flow is not taken to very low scales or derivatives of the interaction vertex grow strongly during the flow, as it provides a good balance between accuracy and computational efficiency.

From the two-patch model we learn that the physics in the vicinity of the QCP is controlled strongly by the balance between the particle-hole bubbles at momenta (π,π) and $(0,0)$. The regularized bubble integrals and solutions of flow equations in Katanin's scheme dependent on the choice of the regulating function, which makes certain symmetry consideration necessary when choosing a regulator.

Chapter 3

Zero Temperature Instabilities of the 2D-Hubbard Model in Static Vertex Approximation

In this chapter we explain the fRG setup for the 2D Hubbard model, which is also relevant for chapters 4 and 5. We then give an overview on the instabilities of the model in a large parameter regime spanned by the chemical potential and hopping amplitude.

3.1 The 2D Hubbard Model

Let $\hat{c}_\sigma(\boldsymbol{x})$ and $\hat{c}^+_\sigma(\boldsymbol{x})$ be fermionic annihilation and creation operators in coordinate space $\boldsymbol{x} \in \mathbb{L}$ with a spin projection σ. The coordinate space

$$\mathbb{L} = \left\{ \boldsymbol{x} = (m_1, m_2) | 0 \leq m_i < L \; \forall i \in \{1,2\} \right\} = \mathbb{Z}^2 / (L\mathbb{Z})^2 \,,$$

corresponds to a two-dimensional periodic square lattice of side length $L \in \mathbb{N}$ in each dimension. For electrons, we denote the up and down spin projection with $\sigma = +$ and $-$, respectively. The particle number operator is defined as $n(\boldsymbol{x}) = \hat{c}^+_\sigma(\boldsymbol{x})\hat{c}_\sigma(\boldsymbol{x})$. In this notation, the Hubbard Hamiltonian including the chemical potential reads

$$H = \sum_{\sigma\in\{+,-\}} \sum_{\boldsymbol{x},\boldsymbol{y}\in\mathbb{L}} \hat{c}^+_\sigma(\boldsymbol{x})\hat{t}(\boldsymbol{x},\boldsymbol{y})\hat{c}_\sigma(\boldsymbol{y}) + U \sum_{\boldsymbol{x}\in\mathbb{L}} n_+(\boldsymbol{x}) n_-(\boldsymbol{x}) - \mu' \sum_{\sigma\in\{+,-\}} \sum_{\boldsymbol{x}\in\mathbb{L}} n_\sigma(\boldsymbol{x}) \,.$$

We restrict ourselves to the t, t' model, where the hopping matrix $\hat{t}(\boldsymbol{x},\boldsymbol{y})$ is equal to $t > 0$ if $\boldsymbol{x},\boldsymbol{y}$ are nearest neighbor sites, equal to $t' : 0 < t'/t < 1/2$ if they are

next-nearest neighbor sites, and equal to zero otherwise. The kinetic term being translational invariant is diagonal in momentum space while the interaction term is diagonal in coordinate space. The momentum space is given by

$$\mathbb{L}^* = \left\{ \boldsymbol{p} = \tfrac{2\pi}{L}(m_1, m_2) | m_i \in \mathbb{Z} \wedge -\pi \leq p_i < \pi \; \forall i \in \{1,2\} \right\} = \left(\tfrac{2\pi}{L}\mathbb{Z}\right)^2 / (2\pi\mathbb{Z})^2 .$$

With the Fourier transformed annihilation operator $c_\sigma(\boldsymbol{k}) = \frac{1}{L}\sum_{\boldsymbol{x}} \mathrm{e}^{-\mathrm{i}(\boldsymbol{x},\boldsymbol{p})}\, \hat{c}_\sigma(\boldsymbol{x})$ implying $c^+_\sigma(\boldsymbol{k}) = \frac{1}{L}\sum_{\boldsymbol{x}} \mathrm{e} + \mathrm{i}(\boldsymbol{x},\boldsymbol{p})\hat{c}^+_\sigma(\boldsymbol{x})$ we obtain

$$H = \sum_{\sigma\in\{+,-\}} \sum_{\boldsymbol{p}\in\mathbb{L}^*} \big(\epsilon(\boldsymbol{p}) - \mu\big) c^+_\sigma(\boldsymbol{p}) c_\sigma(\boldsymbol{p}) + \frac{U}{L^2} \sum_{\boldsymbol{p},\boldsymbol{q},\boldsymbol{\ell}\in\mathbb{L}^*} c^+_+(\boldsymbol{p}+\boldsymbol{\ell}) c^+_-(\boldsymbol{q}-\boldsymbol{\ell}) c_-(\boldsymbol{q}) c_+(\boldsymbol{p}) .$$

The dispersion relation is given by

$$\epsilon\big(\boldsymbol{k} = (x,y)\big) = -2t\big(\cos x + \cos y\big) + 4t'\big(\cos x \cos y + 1\big) .$$

We redefine the chemical potential as $\mu = \mu' + 4t'$ and introduce the abbreviation

$$\xi(\boldsymbol{p}) := \epsilon(\boldsymbol{p}) - \mu .$$

The dispersion relation has three saddle points $\{(0,0),(-\pi,0),(0,-\pi)\}$ in the Brillouin zone. In our notation at $\mu = 0$ the Fermi surface $\{\boldsymbol{k}|\epsilon(\boldsymbol{k}) = 0\}$ passes through the van Hove points $(-\pi,0)$ and $(0,-\pi)$. In the limit $L \to \infty$ the density of states,

$$\rho(e) = \int_{[-\pi,\pi)^2} \delta(\epsilon(\boldsymbol{k}) - e)\mathrm{d}^2\boldsymbol{k} = -\frac{2}{\sqrt{1-\theta^2}} \ln|e| + \mathcal{O}(e\ln|e|) \quad \text{for} \quad e \to 0 ,$$

exhibits a logarithmic divergence and the system is said to be at free van Hove filling.

The partition function at temperature $T = 1/\beta$ is given by

$$Z = \mathrm{tr}\,\mathrm{e}^{-\beta H} / \mathrm{tr}\,\mathrm{e}^{-\beta H|_{U=0}} . \tag{3.1}$$

3.2 Grassmann Integral Representation

Consider a discretization of the Euclidean time axis

$$\mathbb{T}_n := \left\{ \tau_k = \beta k/n | k \in \{0,\ldots,n-1\} \right\}$$

and let $\hat{\overline{\psi}}_{\boldsymbol{p},\sigma}(\tau), \hat{\psi}_{\boldsymbol{p},\sigma}(\tau)$ be Grassmann variables with $\sigma \in \{+,-\}$, $\boldsymbol{p} \in \mathbb{L}^*$ and $\tau \in \mathbb{T}$. In more compact notation we understand $\hat{\overline{\psi}}(\tau) = (\hat{\overline{\psi}}_{\boldsymbol{p},\sigma}(\tau))_{\boldsymbol{p}\in\mathbb{L}^*,\sigma\in\{+,-\}}$ as a column vector at time slice τ and similarly for $\hat{\psi}(\tau)$. We impose antiperiodic boundary conditions

$$\hat{\overline{\psi}}(\tau+\beta) = -\hat{\overline{\psi}}(\tau) \quad \text{and} \quad \hat{\psi}(\tau+\beta) = -\hat{\psi}(\tau)\,.$$

Let $:H:(\hat{\overline{\psi}}(\tau'), \hat{\psi}(\tau))$ stand for the normal ordered Hamilton operator with creation and annihilation operators $c^+_\sigma(\boldsymbol{p})$ and $c_\sigma(\boldsymbol{p})$ replaced with their corresponding Grassmann variable $\hat{\overline{\psi}}_{\sigma,\boldsymbol{p}}(\tau')$ and $\hat{\psi}_{\sigma,\boldsymbol{p}}(\tau)$, respectively. The partition function (3.1) then has the Grassmann integral representation

$$Z = \lim_{n\to\infty} \int \prod_{k=0}^{n-1} \mathrm{d}(\hat{\overline{\psi}}(\tau_k))\mathrm{d}(\hat{\overline{\psi}}(\tau_k))\, \mathrm{e}^{-\frac{\beta}{n}\sum_{k=0}^{n-1}\left[\left(\hat{\overline{\psi}}(\tau), \frac{\hat{\psi}(\tau_k)-\hat{\psi}(\tau_{k-1})}{\beta/n}\right)+:H:(\hat{\overline{\psi}}(\tau_k),\hat{\psi}(\tau_{k-1}))\right]}\,.$$

It is convenient to diagonalize the discrete derivative $\frac{\hat{\psi}(\tau_k)-\hat{\psi}(\tau_{k-1})}{\beta/n}$ by means of Fourier transform. We consider the fields over the domain $\mathbb{T}^{(2)}_n = (\mathbb{T}-\beta)\cup\mathbb{T}$ on which they are periodic. The dual space is given by $\mathbb{T}^{(2)\,*}_n = \left\{\frac{\pi}{\beta}k | k \in \{-n, \cdots, n-1\}\right\}$ and Fourier transform is defined as

$$\hat{f}(\tau) = \frac{1}{2\beta}\sum_{\omega\in\mathbb{T}^{(2)\,*}_n} f(\omega)\,\mathrm{e}^{-\mathrm{i}\omega\tau}\,.$$

Since the Grassmann fields are antiperiodic with respect to $\tau \to \tau+\beta$, their Fourier coefficients are zero if $\omega\beta/\pi$ is even. Thus

$$\hat{\psi}(\tau) = \frac{1}{\beta}\sum_{\omega\in\mathbb{M}_n} \psi(\omega)\,\mathrm{e}^{-\mathrm{i}\omega\tau}\,,$$

where the summation is over *fermionic Matsubara frequencies*,

$$\mathbb{M} = \left\{\tfrac{\pi}{\beta}k | k \in (2\mathbb{Z}-1)\cap[-n,n)\right\}$$

and the factor $1/2$ is absorbed into the definition of the Fourier coefficients. The discrete derivative now reads

$$\frac{\hat{\psi}(\tau_k)-\hat{\psi}(\tau_{k-1})}{\beta/n} = \frac{1}{\beta}\sum_{\omega\in\mathbb{M}_n}(-\mathrm{i})\breve{\omega}\psi(\omega)\,\mathrm{e}^{-\mathrm{i}\omega\tau_k}\,,$$

where

$$\breve{\omega} = -\mathrm{i}\frac{n}{\beta}\left(1-\mathrm{e}^{-\mathrm{i}\omega\beta/n}\right) \xrightarrow{n\to\infty} \omega\,.$$

When taking the limit $n \to \infty$ of a sum or integral over Matsubara frequencies involving $\check{\omega}$ one has to keep in mind that the definition imposes a contour integration in the complex plane. The partition function in momentum space is given by

$$Z = \lim_{n\to\infty} \int \mathrm{d}\mu_C \, \mathrm{e}^{-U \int_{p,q,\ell} \overline{\psi}_+(p+\ell)\overline{\psi}_-(q-\ell)\psi_-(q)\psi_+(p)} , \tag{3.2}$$

where

$$\mathrm{d}\mu_C = \prod_\sigma \prod_p \mathrm{d}\overline{\psi}_\sigma(p)\,\mathrm{d}\psi_\sigma(p)\,\frac{\beta L^2}{\mathrm{i}\check{p}_0 - \mathrm{i}\xi(\boldsymbol{p})}\,\mathrm{e}^{\sum_\sigma \int_p (\mathrm{i}\check{p}_0 - \mathrm{i}\xi(\boldsymbol{p}))\overline{\psi}_\sigma(p)\psi_\sigma(p)} .$$

In the derivation of Eq. (3.2) we have rescaled the Grassmann variables by a factor L^{-1}. So that in our notation $\int_x$ represents a sum over Matsubara frequencies or momenta with appropriate scaling such that

$$\begin{aligned}
\int_{\boldsymbol{p}} \bullet &= \frac{1}{\mathrm{V}} \sum_{\boldsymbol{p}\in\mathbb{L}^*} \bullet \xrightarrow{|\mathbb{L}|\to\infty} \frac{1}{(2\pi)^2} \int_{-\pi}^{\pi} \mathrm{d}p_x \int_{-\pi}^{\pi} \mathrm{d}p_y \bullet , \\
\int_{p_0} \bullet &= \frac{1}{\beta} \sum_{p_0\in\mathbb{M}_n} \bullet \xrightarrow{n,\beta\to\infty} \frac{1}{2\pi} \int_{-\infty}^{\infty} \bullet \, \mathrm{d}p_0 ,
\end{aligned}$$

where $\mathrm{V} := \#\mathbb{L} = \#\mathbb{L}^* = L^2$. Whenever the spin index is included, e.g. $\int_\sigma$, it simply represents a sum over the two possibilities $\sigma \in \{+,-\}$.

3.3 fRG Flow Equations

Suppose we decompose the propagator $C = (C - C_\Omega) + C_\Omega$ into two contributions, C_Ω regular in IR and the rest $C - C_\Omega$. It follows from the semigroup property of the Gaussian measure that the partition function can be written as [68]

$$\begin{aligned}
Z = \int \mathrm{d}\mu_C(\psi,\overline{\psi})\,\mathrm{e}^{V(\psi,\overline{\psi})} &= \int \mathrm{d}\mu_{C-C_\Omega}(\psi,\overline{\psi}) \int \mathrm{d}\mu_{C_\Omega}(\eta,\overline{\eta})\,\mathrm{e}^{V(\psi+\eta,\overline{\psi}+\overline{\eta})} \\
&= \int \mathrm{d}\mu_{C-C_\Omega}(\psi,\overline{\psi})\,\mathrm{e}^{-\mathscr{A}_\Omega(\psi,\overline{\psi})} ,
\end{aligned} \tag{3.3}$$

where

$$\mathscr{A}_\Omega(\eta,\overline{\eta}) = -\ln \int \mathrm{d}\mu_{C_\Omega}(\psi,\overline{\psi})\,\mathrm{e}^{V(\psi+\eta,\overline{\psi}+\overline{\eta})} ,$$

is the generator of the amputated connected green functions.

The amputated connected Green functions and the connected ones are linked

by the relation $\mathscr{G}_\Omega(\eta,\overline{\eta}) = -(\overline{\eta}C_\Omega\eta) + \mathscr{A}_\Omega(C_\Omega\eta, C_\Omega^T\overline{\eta})$. In Chapter 1 we derived flow equations for the self-energy and the four-point irreducible vertex which allow us to compute these quantities for the regularized propagator C_Ω. The two- and four-point amputated connected Green functions are given by

$$A_\Omega^{(2)} = -C_\Omega^{-1} + C_\Omega^{-1}G_\Omega C_\Omega^{-1} = \Sigma_\Omega + \Sigma_\Omega C_\Omega \Sigma_\Omega + \Sigma_\Omega C_\Omega \Sigma_\Omega C_\Omega \Sigma_\Omega + \cdots , \tag{3.4}$$

$$A_\Omega^{(4)}(x_1,\cdots,x_4) = \Gamma_\Omega^{(4)}(x_1,\cdots,x_4)\prod_{i=1}^4 \frac{G_\Omega(k_i)}{C_\Omega(k_i)} \text{ with } x_i = (\sigma_i, k_i)\,. \tag{3.5}$$

The two-point function $A_\Omega^{(2)} \approx \Sigma_\Omega$ is the contribution from the fRG to the inverse covariance of the remaining integral. While the covariance $C - C_\Omega$ is suppressed at high energy or high frequencies due to the regulator, the self-energy remains finite and carries the necessary information accumulated from the flow.

In the case of a sharp cutoff, the short-scale degrees of freedom are effectively absent in the measure $\mathrm{d}\mu_{C-C_\Omega}$ in the sense of the Wilson renormalization group equation.

In the symmetric phase, the effective two-particle interaction at a scale Ω takes the general SU(2) and U(1) symmetric form[1]

$$V(\overline{\psi},\psi) = \frac{1}{2}\int_{p_1\cdots p_4} \delta(p_2 + p_2 - p_3 - p_4)\, v(p_1,p_2,p_3) \sum_{\sigma,\tau} \overline{\psi}_{\sigma\, p_1}\overline{\psi}_{\tau\, p_2}\psi_{\tau\, p_3}\psi_{\sigma\, p_4}\,. \tag{3.6}$$

For the purpose of numerics and to capture the singular momentum dependence of the vertex in an efficient parametrization the interaction vertex (3.6) is decomposed into different channels according to [67],

$$\begin{aligned} V &= V_B + V_K + V_M + V_C\,, \\ V_K(\overline{\psi},\psi) &= -\frac{1}{4}\int_\ell \sum_{m,n=1}^\infty K_{m,n}(\ell)\, S_m^{(0)}(\ell) S_n^{(0)}(-\ell)\,, \\ V_M(\overline{\psi},\psi) &= -\frac{1}{4}\int_\ell \sum_{m,n=1}^\infty M_{m,n}(\ell) \sum_{j=1}^3 S_n^{(j)}(\ell) S_m^{(j)}(-\ell)\,, \\ V_C(\overline{\psi},\psi) &= +\int_\ell \sum_{m,n=1}^\infty D_{m,n}(\ell) \sum_{j=0}^3 \bar{C}_m^{(j)}(\ell) C_n^{(j)}(\ell)\,, \end{aligned} \tag{3.7}$$

[1] From the context, it is clear that the bare propagator, the full propagator, and the effective interaction depend on the scale parameter. However, to avoid overloading the notation we may drop the subscript Ω.

where V_B is the bare Hubbard interaction and $S_\ell^{(j)}, C_\ell^{(j)}, \bar{C}_\ell^{(j)}$ stand for the fermionic bilinears

$$\begin{aligned} S_m^{(j)}(\ell) &= \int_q f_m(\boldsymbol{q}) \overline{\psi}_q^T \sigma^{(j)} \psi_{q+\ell}\,, \\ \bar{C}_m^{(j)}(\ell) &= \frac{\mathrm{i}}{2} \int_q f_m(\boldsymbol{q}) \overline{\psi}_q^T \sigma^{(j)} \overline{\psi}_{\ell-q}\,, \\ C_m^{(j)}(\ell) &= \frac{\mathrm{i}}{2} \int_q f_m(\boldsymbol{q}) \psi_q^T \sigma^{(j)} \psi_{\ell-q}\,, \end{aligned} \tag{3.8}$$

where $\psi(p) = (\psi_+(p), \psi_-(p))^T$, similarly for $\overline{\psi}(p)$, $\sigma^{(j)}$ are the Pauli matrices and f_m are scale independent form factors, in particular

$$\begin{aligned} f_1(\boldsymbol{q}) &= 1\,, \\ f_2(\boldsymbol{q}) &= \cos\left(q_x\right) - \cos\left(q_y\right). \end{aligned}$$

In the case $m = 1$ we drop the subscript from the bilinear, i.e. $S^{(0)} = S_1^{(0)}$. The full interaction vertex is then given by

$$\begin{aligned} v(p_1, p_2, p_3) = U + \sum_{m,n=0}^{\infty} \Big(& f_m(p_1 + \frac{p_3 - p_1}{2}) M_{m,n}(p_3 - p_1) f_n(p_2 - \frac{p_3 - p_1}{2}) \\ & + \frac{1}{2} f_m(p_1 + \frac{p_2 - p_3}{2}) M_{m,n}(p_2 - p_3) f_n(p_2 - \frac{p_2 - p_3}{2}) \\ & - \frac{1}{2} f_m(p_1 + \frac{p_2 - p_3}{2}) K_{m,n}(p_2 - p_3) f_n(p_2 - \frac{p_2 - p_3}{2}) \\ & - f_m(\frac{p_1 + p_2}{2} - p_1) D_{m,n}(p_1 + p_2) f_n(\frac{p_1 + p_2}{2} - p_3) \Big) \end{aligned}$$

in terms of the bosonic propagators $K_{m,n}$, $M_{m,n}$, $D_{m,n}$. In Eq. (3.7) we decided to keep the initial interaction separate[2], the exchange propagators are zero at the beginning of the flow.

Previous studies have shown that the major contributions come from $M_{1,1}$, $K_{1,1}$, $D_{1,1}$ and $D_{2,2}$ [67]. We keep only these terms and neglect the rest. Plugging the

[2] We could have absorbed the constant on-site interaction into $M_{1,1}, K_{1,1}$ or even in $D_{1,1} < 0$ without affecting the overall result.

ansatz (3.6) into the one-loop flow equation (1.12) yields

$$\begin{aligned}
\dot{D}_{m,m}(p) &= +\int_\ell \Pi\big(-\big(\ell-\tfrac{p}{2}\big),\ell+\tfrac{p}{2}\big)F_m^2\big(-D_{m,m}(p),\tfrac{3M-K}{2}\big)(\ell,\boldsymbol{p})\,,\\
\dot{M}_{1,1}(p) &= -\int_\ell \Pi\big(\ell-\tfrac{p}{2},\ell+\tfrac{p}{2}\big)F_1^2\big(+M_{1,1}(p),\tfrac{-2D+M-K}{2}\big)(\ell,\boldsymbol{p})\,,\\
\dot{M}_{1,1}(p) &= -\int_\ell \Pi\big(\ell-\tfrac{p}{2},\ell+\tfrac{p}{2}\big)F_1^2\big(-K_{1,1}(p),\tfrac{-2D+3M+K}{2}\big)(\ell,\boldsymbol{p})\,.
\end{aligned}$$

for the bosonic propagators. Similarly from Equation (1.14) we obtain the self-energy flow equation

$$\begin{aligned}
\dot{\Sigma}(p) =&\big(U-K_{1,1}(0)\big)\int_\ell s(\ell)+\frac{1}{2}\int_\ell s(\ell+p)\big(K_{1,1}(\ell)+3M_{1,1}(\ell)\big)\\
&-\int_\ell s(\ell-p)\Big(D_{1,1}(\ell)+D_{2,2}(\ell)f_2\Big(\tfrac{\ell}{2}-\boldsymbol{p}\Big)\Big)\,.
\end{aligned}\tag{3.9}$$

For a detailed derivation please refer to [67] or [49].

The bare propagator at scale Ω is given by

$$c_\Omega(p)=\frac{\chi_\Omega(p)}{\mathrm{i}\check{p}_0-\xi(\boldsymbol{p})}\,.\tag{3.10}$$

$\chi_\Omega(p)$ is a regulator which will be specified. The full propagator follows from the Dyson equation

$$g_\Omega(p)=\Big(c_\Omega^{-1}(p)-\Sigma_\Omega(p)\Big)^{-1}\,,$$

$s_\Omega(p)$ is the single scale propagator and L is given by

$$\Pi(p_1,p_2)=\frac{\mathrm{d}}{\mathrm{d}\Omega}\big(g_\Omega(p_1)g_\Omega(p_2)\big)\,.$$

The feedback functions F_1 and F_2 are defined as

$$F_1(A,B)(\ell,\boldsymbol{p})=U+A+\int_{\boldsymbol{u}}\big(B_{1,1}(\ell_0,\boldsymbol{u})+B_{2,2}(\ell_0,\boldsymbol{u})f_2\big(\tfrac{\boldsymbol{u}}{2}+\boldsymbol{\ell}-\tfrac{\boldsymbol{p}}{2}\big)f_2\big(\tfrac{\boldsymbol{u}}{2}+\boldsymbol{\ell}+\tfrac{\boldsymbol{p}}{2}\big)\big)$$

and

$$F_2(A,B)(\ell,\boldsymbol{p})=Af_2(\boldsymbol{\ell})+\int_{\boldsymbol{u}}B_{1,1}(\ell_0,\boldsymbol{u})f_2(\boldsymbol{u}-\boldsymbol{\ell})\,.$$

3.4 Regulator and Initial Conditions

Through this thesis, unless stated otherwise, we will use the frequency based Ω-regulator proposed in by Husemann and Salmhofer in [67],

$$\chi_\Omega(p) = \chi_\Omega(\check{p}_0) = \frac{\check{p}_0^2}{\check{p}_0^2 + \Omega^2}\,. \tag{3.11}$$

In the limit $n = \#\mathbb{T}_n \to \infty, \beta \to \infty$ the scale dependent bare propagator c_Ω given in Eq. (3.10), will have three poles in the complex plane. Two of them due to the regulator χ_Ω. The pole $\mathrm{i}\Omega$ in the upper-half plane contributes a residue to the tadpole integral,

$$\oint_{p_0} c_\Omega(p) = \frac{\epsilon(\boldsymbol{p})^2}{\epsilon(\boldsymbol{p})^2 - \Omega^2}\Theta(-\epsilon(\boldsymbol{p})) + \frac{\Omega}{2(\epsilon(\boldsymbol{p}) + \Omega)} = \frac{1}{2} - \frac{\epsilon(\boldsymbol{p})}{|\epsilon(\boldsymbol{p})| + \Omega}\,. \tag{3.12}$$

So even though $\forall p : \lim_{\Omega\to\infty} c_\Omega(p) = 0$, the tadpole remains finite. The initial condition for the flow equation of the self-energy is given by the solution of (1.10b) in the limit $\Omega \to \infty$. Thus with this choice of the regulating function, due to the tadpole term we obtain

$$\lim_{\Omega\to\infty} \Sigma_\Omega(p) = \frac{U}{2}\,.$$

The bubble integrals converge to zero in the limit $\Omega \to \infty$ and don't contribute to the initial condition of the self-energy or the 1PI vertex. The initial condition for the four-point irreducible vertex is simply the initial interaction.

3.5 Fixing the Fermi Surface

The static self-energy cannot generally be assumed to be small. An initial value can trivially be compensated by the chemical potential. However, the static self-energy flows and is not constant as a function of the scale parameter. Nevertheless, we can compensate any static (and momentum independent) self-energy during the flow. This allows us to control the density, e.g. to stay at van Hove filling. This is desirable since certain states are very sensible to the position of the Fermi surface; for example, the ferromagnetic state benefits strongly from van Hove filling or the anti-ferromagnet from nesting. By fixing the Fermi surface, we gain control over the final state of the flow and can investigate physics at vHF more accurately. Results obtained from flow equations with fixed Fermi surface are also easier to interpret.

We decompose the self-energy $\Sigma_\Omega = \sigma_\Omega + \Sigma'_\Omega$ into a static part σ_Ω and the rest Σ'_Ω. Let $S_\Omega(p) = \chi_\Omega(p)\sigma_\Omega$. S_Ω is not known prior, but can be computed at any scale Ω during the flow. We define a new regulating function

$$\tilde{\chi}_\Omega(p) = \chi_\Omega(p)\frac{\mathrm{i}\check{p}_0 - \epsilon(\boldsymbol{p}) + \mu + S_\Omega}{\mathrm{i}\check{p}_0 - \epsilon(\boldsymbol{p}) + \mu},$$

such that

$$\tilde{\chi}_\Omega(p)c(p) = \chi_\Omega(p)\frac{\mathrm{i}\check{p}_0 - \epsilon(\boldsymbol{p}) + \mu}{\mathrm{i}\check{p}_0 - \epsilon(\boldsymbol{p}) + \mu + S_\Omega(p)} \cdot \frac{1}{\mathrm{i}\check{p}_0 - \epsilon(\boldsymbol{p}) + \mu} = \frac{\chi_\Omega(p)}{\mathrm{i}\check{p}_0 - \epsilon(\boldsymbol{p}) + \mu + S_\Omega(p)}.$$

The full propagator at scale Ω is then given by

$$\begin{aligned} g_\Omega(p) &= \left(\frac{\mathrm{i}\check{p}_0 - \epsilon(\boldsymbol{p}) + \mu + S_\Omega(p)}{\chi_\Omega(p)} - \Sigma_\Omega(p)\right)^{-1} \\ &= \frac{\chi_\Omega(p)}{\mathrm{i}\check{p}_0 - \epsilon(\boldsymbol{p}) + \mu + S_\Omega(p) - \sigma\chi_\Omega(p) - \Sigma'_\Omega(p)\chi_\Omega(p)}, \end{aligned}$$

where S_Ω cancels the term $\sigma\chi_\Omega(p)$ and we obtain

$$g_\Omega(p) = \frac{\chi_\Omega(p)}{\mathrm{i}\check{p}_0 - \epsilon(\boldsymbol{p}) + \mu - \Sigma'_\Omega(p)\chi_\Omega(p)}. \tag{3.13}$$

The regulator enters the flow equations only through the full propagator (3.13), its derivative $\dot{g}_\Omega$ and through the single scale propagator

$$s_\Omega(p) = \frac{\mathrm{d}}{\mathrm{d}\Omega} g_\Omega(p)\Big|_{\Sigma=\text{const.}}.$$

Thus, remarkably the final result looks the same as if we had naively ignored the static self-energy. The details will not concern us again until Chapter 4.

3.6 Parameterization of the Interaction and the Self-energy

For the purpose of numerics, we have to project the bosonic propagators onto a finite set of numbers. We take advantage of the following symmetries to reduce the size of the data set. All exchange propagators and the self-energy are invariant under spatial reflection $x \to -x$, $y \to -y$ and $x \leftrightarrow y$ due to the

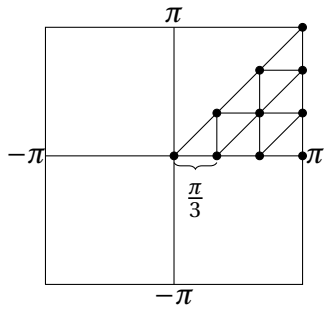

Figure 3.1: A $\frac{\pi}{3}$-patching of the Brillouin zone. Black circles show the position of representative momentums. Since all exchange propagators and the self-energy are invariant under $x \to -x$, $y \to -y$ and $x \leftrightarrow y$ we only need to consider one-eighth of the Brillouin zone in the patching.

symmetries of the underlying lattice. Furthermore, their real (imaginary) part is symmetric (antisymmetric) under $\omega \to -\omega$ due to time reversal symmetry. We compute representative values in one-eighth of the Brillouin zone and deduce values for any other momentum through symmetries and interpolation. In static approximations we project all frequencies to $\omega = 0$. In frequency dependent calculations, we consider a logarithmic grid along positive frequencies. Figure 3.1 shows an example of our Brillouin zone patching scheme. We will refer to a patching by specifying its resolution (distance between neighbor representative points).

3.7 Summary of Over Sixty Thousand Flows

The static vertex approximation has been used by Honerkamp, Husemann, Giering and Salmhofer [66, 71, 67, 49] to study the Hubbard model at van Hove filling. With extensive optimization (see appendix C for details) we increased the numerical performance of our integration routine by almost two orders of magnitude compared to older implementations which allows us to explore a much larger parameter regime in reasonable time.

We compute the flow of the static exchange propagators neglecting the self-energy in a $\frac{\pi}{5}$-patching. We follow the flow until the largest coupling reaches $20t$ which is already much larger than the bandwidth ($8t$), or until the scale drops below $10^{-6}/t$. We refer to the scale at the end of the integration as the stopping scale Ω^*. We identify the dominant instability from the largest coupling. In practice one of the following scenarios is the case:

- $B_{2,2}$ at zero transfer momentum signaling a d-wave superconductor.
- $M_{1,1}$ at zero transfer momentum signaling a ferromagnet.

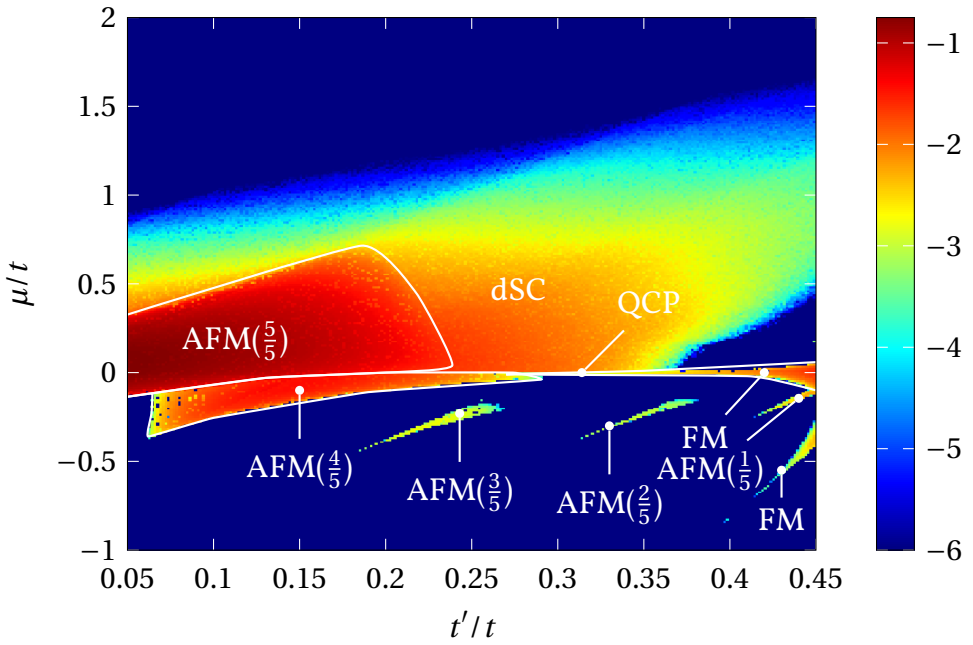

Figure 3.2: Leading instabilities and decadic logarithm of the stopping scale Ω^* within the stationary vertex approximation. The lower bound is due to the hard coded termination of the algorithm at $\Omega = 10^{-6}t$. These results were obtained using a $\frac{\pi}{5}$-patching and AMF(k/n) means that the instability was found in the magnetic channel at the momentum exchange $(\pi, k\pi/n)$.

- $M_{1,1}$ at transfer momentum (π,π) signaling a commensurate antiferromagnet.
- $M_{1,1}$ at transfer momentum $(\pi, k\frac{\pi}{5}), 0 < k < 5$ signaling an incommensurate antiferromagnet.

The incommensurate antiferromagnetic order is affected by the finite resolution of the patching. We refer to a phase with the largest coupling at $(\pi, k\frac{\pi}{5})$ in $M_{1,1}$ as AFM(k/5).

Figure 3.2 summarizes the result of 65536 flows for an initial interaction $U = 3t$. For $\mu/t > 0$, i.e. when the van Hove points are all inside the Fermi surface, Cooper pairing is the dominant instability in large parts of the phase diagram. At almost full band the stopping scale drops below our numerical limit, but we still expect superconducting tendencies due to the Kohn-Luttinger effect [68]. For $t'/t < 0.25$ commensurate antiferromagnet AFM(5) takes over. A coexistence

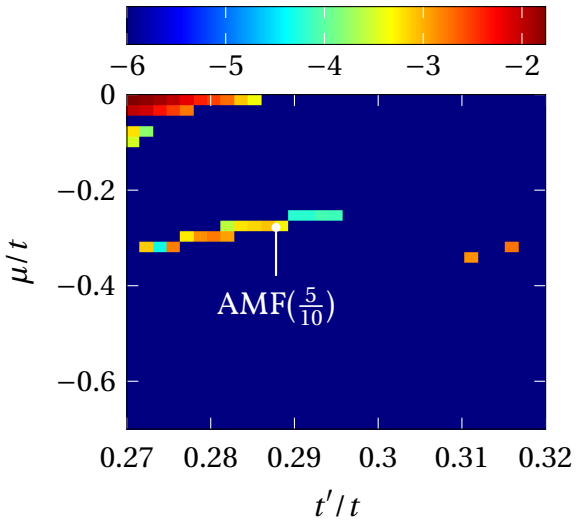

Figure 3.3: Stopping scale within the stationary vertex approximation in a $\frac{\pi}{10}$-patching. A region with antiferromagnetic instabiblity corresponding to a transverse wace vector $(\pi, \pi/5)$ is identifed which was missed by calculations in the $\frac{\pi}{5}$-patching, c.f. Figure 3.2.

of antiferromagnetic and superconducting phase is generally possible. A small ferromagnetic region shows itself close to van Hove filling and extends in the region with hopping amplitudes $t'/t > 0.34$ and $\mu/t < 0$, i.e. at small fillings. This is not surprising since in the first case the van Hove points are known to be crucial for the ferromagnetic ordering and in the latter case the Hubbard model at a small filling maps to a continuum repulsive Fermi gas which is known to exhibit a stoner instability.

We find several *islands* in the region $\mu/t < 0$ with dominant incommensurate antiferromagnet instabilities. We believe that in between the islands the dominant instability is also the antiferromagnetic one although with a transverse wave vector, which cannot be captured due to the finite resolution of the patching. Increasing the resolution leads to a large number of islands which verifies this claim. Figure 3.3 shows the result for flows computed suing a $\frac{\pi}{10}$-patching. As expected, a new island with a transverse vector $(\pi, \pi/2)$ appears between instability regions corresponding to AFM(2/5) and AFM(3/5).

We know that antiferromagnetic ordering is triggered by Fermi surface nesting. Figure 3.5 shows the shape of the Fermi surface for two different combinations of hopping parameter and chemical potential in the AFM(3/5) regime. The associated points have been labeled by (a) and (b) in Figure 3.4. The point (a) is roughly the transition point between a concave Fermi surface for smaller hopping parameters and a convex one at larger hopping parameters. A concave Fermi surface disfavors nesting and the antiferromagnetic instability disappears.

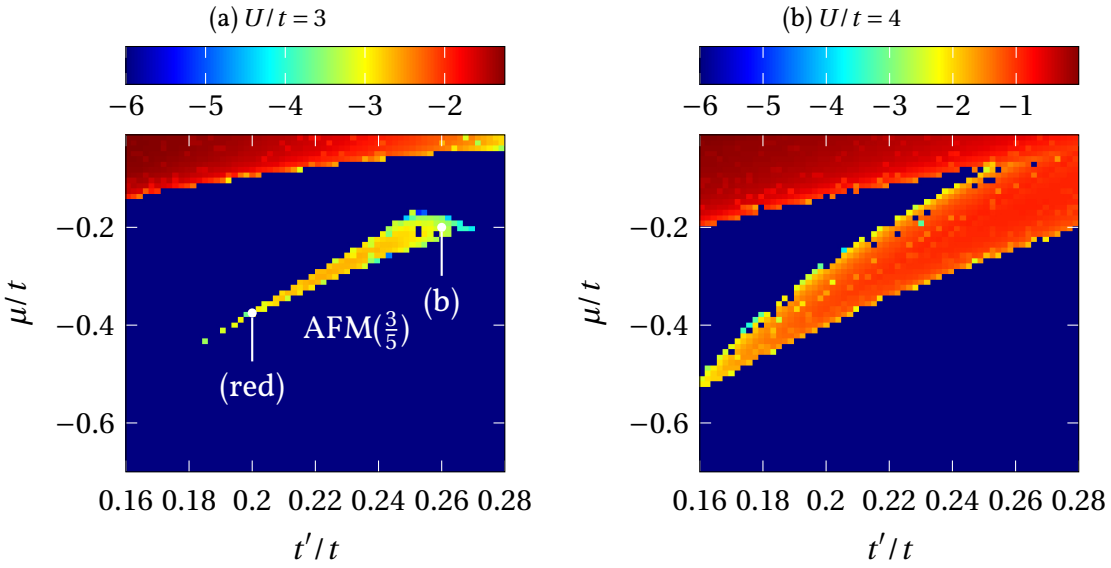

Figure 3.4: Decadic logarithm of the stopping scale within the stationary vertex approximation for (a) $U/t = 3$ and (b) $U/t = 4$. The antiferromagnetic ordering becomes much more pronounced with increased interaction strength.

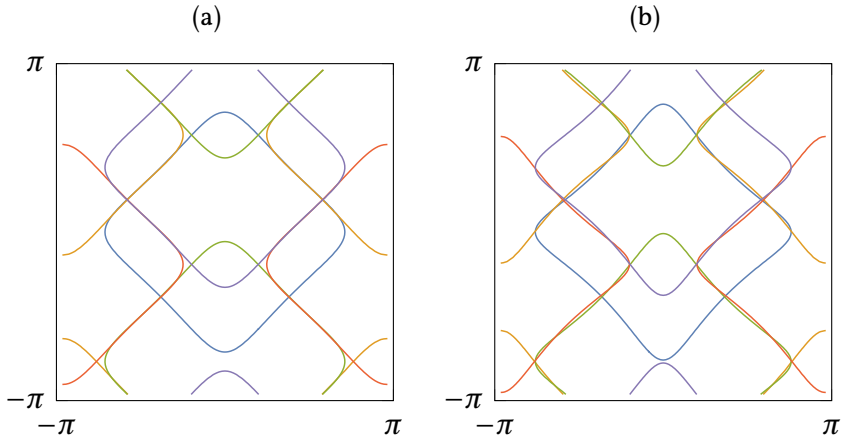

Figure 3.5: Fermi surface and few translates $\{\boldsymbol{p}|\xi(\boldsymbol{p}+\boldsymbol{k}q) = 0\}$, $k \in \{0..4\}$ with $q = (\pi, 3\pi/5)$. Hopping parameter and chemical potentials correspond to points (a) and (b) marked in Figure 3.4.

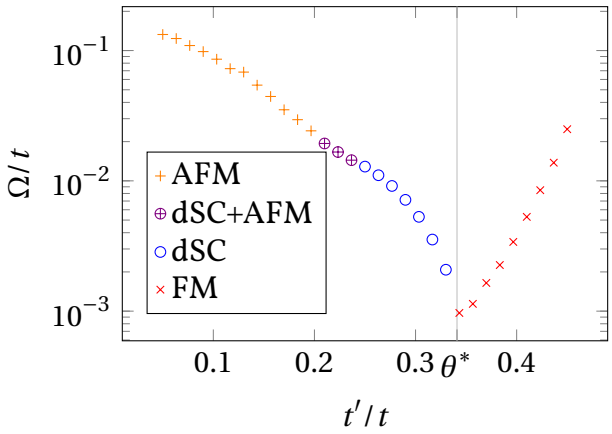

Figure 3.6: Decadic logarithm of the stopping scale as a function of hopping parameter at van Hove filling. The drastic drop of the stopping scale at $\theta^\star = 0.341$ signals a quantum critical point.

At larger hopping amplitudes, e.g. in point (b) the nesting is less notable but still present, due to the convex shape of the Fermi surface. Increasing the interaction strength makes up for imperfect nesting by allowing states in a larger shell around the Fermi surface to participate in the dynamics. Figure 3.4 shows a side-by-side comparison between results for initial interactions $U/t = 3$ and $U/t = 4$. In the case $U/t = 4$ the AFM(3/5) instability is much more pronounced in the phase diagram. As anticipated states with a convex Fermi-surfaces benefit more from increased interaction strength.

At van Hove filling and at $t'/t = \theta^\star := 0.341$ the stopping scale drops significantly as the system undergoes a phase transition from superconducting ($\theta < \theta^\star$) to ferromagnetic ($t'/t > \theta^\star$). This can best be seen in Figure 3.6.

3.8 Final Remarks

After extensive optimization, we are able to compute an fRG flow in the static vertex approximation within only a few minutes on a single CPU core. This allowed us to gain an overview on the instabilities of the 2D-Hubbard model in a large parameter space. The incommensurate antiferromagnetic instability is hard to capture in our parametrization.

An instability predicts a symmetry broken ground state. However, one needs to compute the gaps and the free-energy to certify the result. From a mean-field point of view, gap formation requires a minimal interaction strength. If not granted one might find a paramagnetic phase. Increasing the bare interaction strength makes the instabilities more pronounce and will usually lead to a

symmetry broken ground state. In this sense the instabilities, in particular when the stopping scale is large, forecast the phase diagram of the Hubbard model.

There are few regions in the phase diagram where static vertex approximation might be insufficient. In particular, we have to check for self-energy effects in three regions. First, in the vicinity of the potential QCP at $\theta^\star = 0.341$ and vHF. This parameter region has been analyzed by Giering and Salmhofer with frequency dependent flows including the imaginary part of the self-energy as a frequency dependent but momentum independent function. [49, 48]. They found that the self-energy shows a non-Fermi-liquid-like frequency dependency. Furthermore, the inclusion of the self-energy suppresses the growth of the couplings, leading to an even stronger decline of the stopping scale. In the next chapter we continue their work by means of mean-field calculations, and in chapter 5 we will consider the effects of the full self-energy on the flow at this point in the phase diagram. Second, in the region of large hopping parameter and small but positive chemical potential where the self-energy might lead to a deformation of the Fermi surface which might enhance the ferromagnetic instability. Third, in the vicinity of $\theta^\star$ and for $\mu/t > 0$. In Chapter 5 we will investigate the matter.

In Section 3.4 we pointed out that the pole $\mathrm{i}\Omega \in \mathbb{H}_+$ of the Ω-regulator affects the tadpole frequency integral. This does not seem to be an issue, yet it is possible to preserve the analytic structure of the propagator in the upper-half complex plane by using a regulator such as

$$\chi^{\mathrm{c}}_{\Omega}(\omega) = \frac{\omega}{\omega + \mathrm{i}\Omega}\,. \tag{3.14}$$

Although complex, this regulator does not break time reversal symmetry. But it has other disadvantages which, at least for now, make it less preferable compared to the Ω-regulator. Please refer to Chapter 5 for details.

Chapter 4

Quantum Criticality in fRG + Mean-Field Calculations

4.1 Introduction

This work continues previous fRG studies of the two-dimensional repulsive Hubbard model by Giering, Husemann and Salmhofer, which have been published in [48], [45] and [49]. The flow of the 1PI two and four-point Green function were computed in the Ω-scheme [67]. The setup is very similar to the last chapter, although in this instance frequency dependence of the exchange propagators and self-energy were taken into account, assuming the self-energy to be purely imaginary and momentum independent, with all momenta projected to the van Hove point $(\pi, 0)$. The fRG calculations provide the effective action at some finite stopping scale Ω^*. The dominant instabilities can be read out of the structure of the four-point Green function, which indicate a quantum critical point in the vicinity of the hopping amplitude $t'/t = \theta^\star = 0.341$ at van Hove filling ($\mu = 0$), c.f. Table 4.1. Instabilities found in RG flows don't guarantee gap formation, nor is the absence of instabilities at some finite scale sufficient to rule out a symmetry broken ground state. Furthermore, at the QCP the self-energy shows a non-Fermi-liquid-like (NFLL) frequency behavior. In this chapter we want to investigate the effects of this self-energy on gap formation. We complement the fRG calculation by computing the relevant gap parameters in a mean-field approximation using Hubbard-Stratonovich transformation.

Hubbard-Stratonovich (HS) transformation is based on the following elementary integral equations. For $a, b \in \mathbb{C}$ or commuting element of some Grassmann

algebra

$$e^{a^2/4} = \frac{1}{\sqrt{\pi}} \int_{\mathbb{R}} e^{-\phi^2 + \phi a} \, d\phi \,, \tag{4.1}$$

$$e^{ab} = \int_{\mathbb{C}} e^{-|\phi|^2 + a\phi + b\overline{\phi}} \, \frac{d\phi \wedge d\overline{\phi}}{2\pi i} \,. \tag{4.2}$$

After *bosonization* we can evaluate the path integral in the saddle-point, i.e. mean-field approximation. This combination makes for a conceptually simple and valuable tool in understanding symmetry breaking in interacting fermion systems. It has been used to study the magnetic phase diagram of the two dimensional repulsive Hubbard model [14]. Due to the sign of the interaction at the bare level, Cooper pairing is not accessible without taking into account the fluctuations. However, during the fRG flow the effective interaction develops a long-range attractive tail, which is believed to be responsible for superconductivity [72]. In order to compute the gaps we stop the flow after the dominant instability has shown itself and compute the gaps in a mean-field approximation using the effective interaction and the self-energy at the stopping scale. First, we investigate the effect of the NFLL self-energy on electron ordering and pairing. Then we will study the relation between the frequency dependent interaction and the emergence of such a self-energy.

4.2 Quantum Critical Behavior in a Minimal Toy Model

Before diving into the fRG+MF formalism we may begin with a minimal toy model. Consider the mixed action

$$S = -\int_{k,\sigma} (i\,k_0 - \epsilon_{\boldsymbol{k}} - \Sigma(k_0)) \overline{\psi}_{k,\sigma} \psi_{k,\sigma} + \Delta_{\mathrm{x}} \cdot \widehat{O}_{\mathrm{x}} + \beta V \frac{|\Delta_{\mathrm{x}}|^2}{U_{\mathrm{x}}} \,,$$

where $\epsilon_{\boldsymbol{k}}$ is the Hubbard dispersion relation at van Hove filling, Σ is purely imaginary self-energy and $\widehat{O}_{\mathrm{x}}$ is an operator quadratic in the fields $\psi, \overline{\psi}$ corresponding to some type of order. In particular we will use extrapolation of the self-energy obtained in fRG calculations [48],

$$\Sigma(\omega) = -0.39\, i\, \mathrm{sgn}(\omega) |\omega|^{0.74} \tag{4.3}$$

and

$$\widehat{O}_{\mathrm{FM}} = \int_{k,\sigma} \sigma\, \overline{\psi}_{k,\sigma} \psi_{k,\sigma} \,,$$
$$\widehat{O}_{\mathrm{dSC}} = \frac{1}{2} \int_{k,\sigma} \sigma\, f_2(\boldsymbol{k}) \overline{\psi}_{k,\sigma} \overline{\psi}_{-k,-\sigma} \,.$$

The expectation values of these operators $O_{\mathrm{x}} := \langle \widehat{O}_{\mathrm{x}} \rangle$, $\mathrm{x} \in \{\mathrm{FM}, \mathrm{dSC}\}$ then define order parameters for the ferromagnetic and d-wave superconducting phases. The gap parameter Δ_{x} is the static part of the bosonic Hubbard–Stratonovich field. $U_{\mathrm{x}} > 0$ denotes the corresponding interaction strength. In Section 4.5 we will make the relation to the repulsive Hubbard model explicit.

Integrating out the fermions leaves us with a determinant whose logarithm enters in the remaining bosonic action as a non-trivial potential. The self-consistency equation for the gap parameter is then given by the saddle point equation of the bosonic action,

$$\Delta_{\mathrm{FM}} = \frac{U_{\mathrm{FM}}}{2} \int_{k,\sigma} \frac{\sigma}{\mathrm{i}(k_0 - \mathrm{Im}\,\Sigma(k_0)) - \epsilon_{\boldsymbol{k}} + \sigma \Delta_{\mathrm{FM}}} \,,$$
$$1 = U_{\mathrm{dSC}} \int_{k} \frac{f_2^2(\boldsymbol{k})}{(k_0 - \mathrm{Im}\,\Sigma(k_0))^2 + \epsilon_{\boldsymbol{k}}^2 + f_2^2(\boldsymbol{k}) \left|\Delta_{\mathrm{dSC}}\right|^2} \,,$$

and the order parameter is given by $O_{\mathrm{x}} = 2\Delta_{\mathrm{X}} / U_{\mathrm{x}}$. Let F_Σ be the Fermi function

$$F_\Sigma(\xi) = \int_{\omega} \frac{1}{\mathrm{i}(\omega - \mathrm{Im}\,\Sigma(\omega)) - \xi}$$

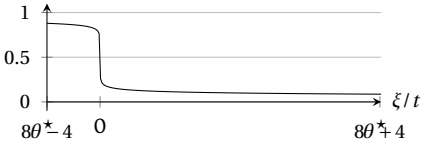

,

then we can express the self-consistency equations also in the form

$$1 = \frac{U_{\mathrm{FM}}}{2} \int_{\boldsymbol{k},\sigma} \frac{\sigma\, F_\Sigma(\epsilon_{\boldsymbol{k}} - \sigma \Delta_{\mathrm{FM}})}{\Delta_{\mathrm{FM}}} \,, \tag{4.5a}$$

$$1 = \frac{U_{\mathrm{dSC}}}{2} \int_{\boldsymbol{k},\sigma} \frac{f_2^2(\boldsymbol{k})}{E_{\boldsymbol{k}}} \sigma F_\Sigma(-\sigma E_{\boldsymbol{k}}) \quad \text{with} \quad E_{\boldsymbol{k}} = \sqrt{\epsilon_{\boldsymbol{k}}^2 + f_2^2(\boldsymbol{k}) \left|\Delta_{\mathrm{dSC}}\right|^2} \,. \tag{4.5b}$$

The self-energy (4.3) is known to suppress the quasiparticle weight [48]. As a result we expect and find suppressed gap formation in our toy model. The

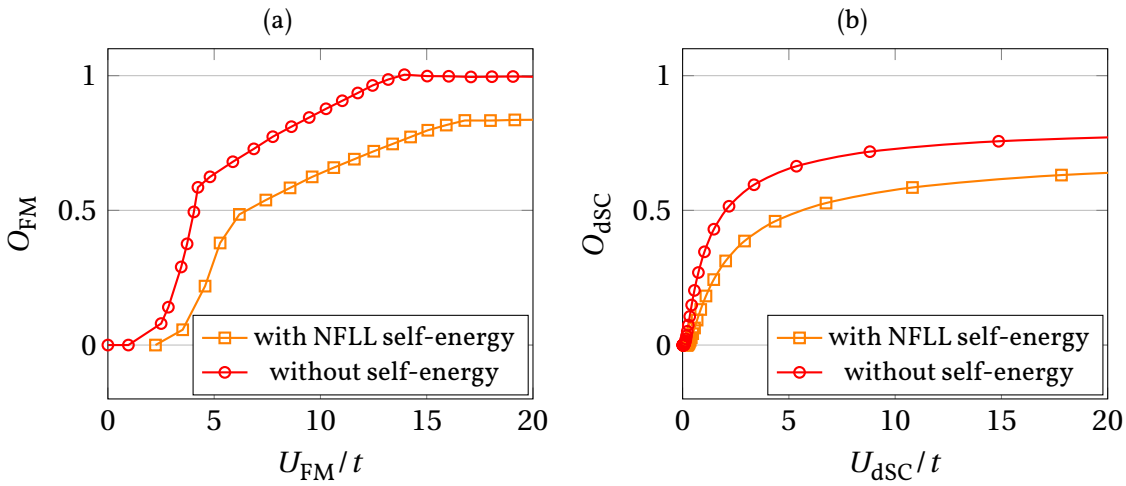

Figure 4.1: Zero temperature expectation values O_{FM} and O_{dSC} as a function of interaction strength with and without self-energy. The NFLL self-energy (4.3) suppresses gap formation.

suppression of the expectation values O_{FM} and O_{dSC} at fixed interaction strength due to self-energy is shown in Figure 4.1. The kinks in Figure 4.1a are due to the integrand in Eq. (4.5a), $F(\epsilon_{\boldsymbol{k}} - \sigma\Delta_{\mathrm{FM}})$ becoming approximately independent of Δ_{FM} when $\Delta_{\mathrm{FM}} < \min_{\boldsymbol{k}} \epsilon_{\boldsymbol{k}}$ or $\Delta_{\mathrm{FM}} > \max_{\boldsymbol{k}} \epsilon_{\boldsymbol{k}}$. In the zero temperature limit the self-energy imposes an important constrain on gap formation which is not obvious from Figure 4.1. Without the self-energy, the integrals in Eq. (4.5a,4.5b) are divergent in the limit $\Delta_{\mathrm{X}} \to 0$, and as a result the gap equations have solutions for arbitrary small values of the interaction. In the presence of the NFLL self-energy, this is no longer the case. The integrals converge and a minimal required interaction strength is needed for a gap to form. In our case

$$\begin{aligned} U_{\mathrm{FM}}^{\min}/t &= \left(-\int_{\boldsymbol{k}} F_\Sigma'(\epsilon_{\boldsymbol{k}}) \right)^{-1} \approx 2.05\,, \\ U_{\mathrm{dSC}}^{\min}/t &= \left(\frac{1}{2}\int_{\boldsymbol{k}} \frac{f_2^2(\boldsymbol{k})}{|\epsilon_{\boldsymbol{k}}|} \big(F_\Sigma\big(-|\epsilon_{\boldsymbol{k}}|\big) - F_\Sigma\big(|\epsilon_{\boldsymbol{k}}|\big) \big) \right)^{-1} \approx 0.18\,. \end{aligned} \tag{4.6}$$

This simple calculation verifies that the NFLL self-energy we observe at van Hove filling and $t'/t = \theta^\star$ during the flow can indeed suppress ordering and lead to a quantum critical behavior.

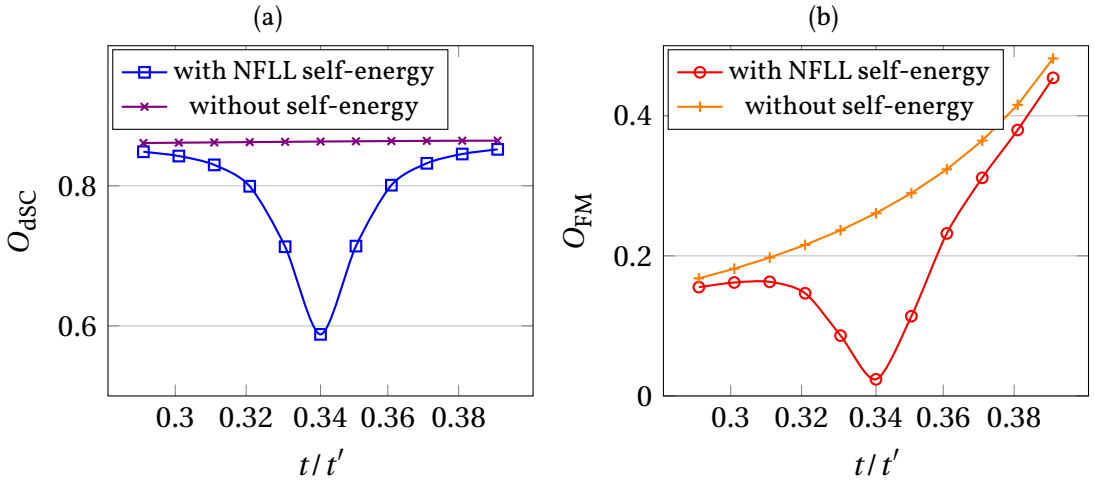

Figure 4.2: O_{FM} and O_{dSC} as a function of the hopping parameter t'/t with the self-energy (4.7), and without the inclusion of self-energy. The bare interaction is $U_{\mathrm{FM}} = U_{\mathrm{dSC}} = 3t$ and $a = 100$.

The NFFL self-energy is restricted to hoppings close to $\theta^\star$. In our toy model we may simulate this by using the self-energy

$$\Sigma(\omega) = \frac{-0.39\mathrm{i}}{1 + a^2(t/t' - \theta^\star)^2}\mathrm{sgn}(\omega)|\omega|^{0.74}, \tag{4.7}$$

with a falloff $(1 + a^2(\theta - \theta^\star)^2)^{-1}$ based on the difference between the hopping parameter t'/t and the critical hopping $\theta^\star$. Figure 4.2 shows the effect of this self-energy on gap formation as a function of the hopping amplitude. The inclusion of the NFFL self-energy has clearly a strong impact on the order parameter, keeping them small.

The lower bounds (4.6) we have found here are insufficient to prevent gap formation for our typical interaction strengths during the flow for a bare repulsive interaction $U/t = 3$. However, the toy model overestimates the gaps compared to a more sophisticated calculation where the regulator is still present and the mean-field calculation approximates the functional integral left over after the flow has stopped. In the following section we will include the regulator and compute the gaps starting with fRG data at the stopping scale.

4.3 fRG+MF Setup

While the *exact* RG flow is enough to determine the statistical properties of Hubbard model, in practice we have to content ourselves with certain approximation. In our case singularities emerging as a result of the truncation and the restriction of the flow to the symmetric phase force us to stop the flow at some intermediate scale. In the vicinity of a possible QCP we can drive the flow to scales as low as $\Omega/t \sim 10^{-5}$. Lower scales are hardly accessible as the accurate evaluation of bubble integrals becomes challenging. In order to manifest the existence of QCP we have to show that even if we carry out the remaining integral over low-frequency modes no gaps emerge. So, even though we have gained access to an effective action which accommodates the behavior of the high frequency degrees of freedom, there is still a difficult path integral involved in the computation of the partition function and consequently in the computation of every statistical expectation value. The simplest tool to proceed from this point is a mean-field treatment which involves bosonization of fermionic bilinears followed by a saddle point approximation.

The fRG flow provides us the effective 1PI interaction at some scale Ω. The partition function is given by (c.f. (3.3))

$$Z = \int \mathrm{d}\mu_{C-C_\Omega}(\psi,\overline{\psi})\, \mathrm{e}^{-\mathscr{A}_\Omega(\psi,\overline{\psi})}\,,$$

where the two- and four-point amputated connected Green functions are given by

$$A^{(2)}_\Omega = -C_\Omega^{-1} + C_\Omega^{-1} G_\Omega C_\Omega^{-1} = \Sigma_\Omega + \Sigma_\Omega C_\Omega \Sigma_\Omega + \Sigma_\Omega C_\Omega \Sigma_\Omega C_\Omega \Sigma_\Omega + \cdots\,, \qquad \text{(3.4 revisited)}$$

$$A^{(4)}_\Omega(x_1,\cdots,x_4) = \Gamma^{(4)}_\Omega(x_1,\cdots,x_4) \prod_{i=1}^{4} \frac{G_\Omega(k_i)}{C_\Omega(k_i)} \text{ with } x_i = (\sigma_i, k_i)\,. \qquad \text{(3.5 revisited)}$$

For the next section it is beneficial to absorb the self-energy corrections in Eq. (3.5) on the external legs into the definition of a new set of Grassmann variables

$$(\overline{\Psi}_{k,\sigma}, \Psi_{k,\sigma}) := \frac{G_\Omega(k)}{C_\Omega(k)} (\overline{\psi}_{k,\sigma}, \psi_{k,\sigma})\,,$$

so we can write the partition function as

$$Z \propto \int \mathrm{d}\mu_T(\overline{\Psi},\Psi)\, \mathrm{e}^{-V_\Omega(\Psi,\overline{\Psi})}\,, \qquad (4.8)$$

where V_Ω includes the four-point 1PI vertex $\Gamma^{(4)}_\Omega$ at the scale Ω and $(T_\Omega)_{k,k'} = \delta_{k,k'} T_\Omega(k)$ is the covariance in the new base with

$$\begin{aligned} T_\Omega^{-1}(k) &= \frac{C_\Omega(k)}{G_\Omega(k)}\left(\frac{\chi_\Omega(k_0)G_\Omega^{-1}(k)}{1-\chi_\Omega(k_0)} - \Sigma_\Omega(k)\right) \\ &= \frac{1}{1-\chi_\Omega(k_0)}\Big(C^{-1}(k) - \Sigma_\Omega(k) - \chi_\Omega(k)\Sigma_\Omega(k) + \chi_\Omega(k)C(k)\Sigma_\Omega^2(k)\Big)\,. \end{aligned} \tag{4.9}$$

The latter expression is exact and not based on a truncation of Eq. (3.4) to second order in Σ. V_Ω is decomposed into different channels according to Eq. (3.7).

In the numerical treatment of the repulsive Hubbard model, only $K_{1,1}$, $M_{1,1}$, $D_{1,1}$ and $D_{2,2}$ were included. These exchange propagators remain positive during the flow with exception of $K_{1,1}$. The static part of $K_{1,1}$ is positive while it develops a negative peak at finite frequency. At the first glance, the positive static part signals an attractive density-density interaction but since the vertex decomposition is not unique we shall take into account all channels and judge based on the overall sing of v as defined in Eq. (3.6).

We will dedicate a section to the effects of the frequency dependent interaction on the self-energy which is of particular interest at the QCP. Elsewhere we assume approximate static homogeneous density and proceed as follows.

4.4 Nonlocal Interaction in Mean-Field Calculations

We will use the output of the fRG flow as the starting point for mean-field calculations. Even though we start with a local on-site interaction, the effective interaction vertex is nonlocal. Here we introduce meaningful approximations to estimate the gaps using only the dominant part of the interaction in each channel.

We will use the notation defined in Chapter 3. The bilinears $S^{(j)}$, $C^{(j)}$ are defined in Eq. (3.8).

4.4.1 Ferromagnetic State

In order to estimate the free-energy of an ferromagnetic state we start with the effective spin-spin interaction in position space[1]

$$V_M = -\frac{1}{4}\int_{x,y} \hat{M}(x-y)\,\hat{\boldsymbol{S}}(x)\cdot\hat{\boldsymbol{S}}(y)$$

and write the interaction as

$$\begin{aligned} V_M &= -\frac{1}{8}\int_{x,y} \hat{M}(x-y)\left[-\left(\hat{\boldsymbol{S}}(x)-\hat{\boldsymbol{S}}(y)\right)^2+\hat{\boldsymbol{S}}^2(x)+\hat{\boldsymbol{S}}^2(y)\right] \\ &= \underbrace{\frac{1}{4}\int_{\{x,y\}} \hat{M}(x-y)\left(\hat{\boldsymbol{S}}(x)-\hat{\boldsymbol{S}}(y)\right)^2}_{V_M^{\text{non-local}}} \underbrace{-\frac{1}{4}M(0)\int_x \hat{\boldsymbol{S}}^2(x)}_{V_M^{\text{local}}} . \end{aligned}$$

The local and nonlocal terms are now separate. For the moment, consider only the nonlocal part of Eq. (4.4.1). A Hubbard-Stratonovich transformation would lead to the bosonic action

$$V_M^{\text{non-local}} \xrightarrow{\text{H.S.}} S_M^{\text{non-local}} = -\int_{\{x,y\}} \frac{\boldsymbol{\Phi}_{x,y}^2}{M(x-y)} + \mathrm{i}\int_{\{x,y\}} \boldsymbol{\Phi}_{x,y}\cdot\left(\hat{\boldsymbol{S}}_x-\hat{\boldsymbol{S}}_y\right) ,$$

where the expectation value of $\Phi_{x,y}$ is given by

$$\langle\Phi_{x,y}\rangle = \frac{\mathrm{i}}{2}\hat{M}(x-y)\,\langle\hat{\boldsymbol{S}}_x-\hat{\boldsymbol{S}}_y\rangle .$$

It is reasonable to assume that in the ferromagnetic phase $\langle\hat{\boldsymbol{S}}_x-\hat{\boldsymbol{S}}_y\rangle$ vanishes due to translational invariance. So $\Phi_{x,y}$ does not contribute to the free-energy in the saddle-point approximation where one neglects fluctuations. Thus if we are only interested in estimating the free-energy of a possible ferromagnetic state and obtaining a lower bound, in particular, we may neglect the nonlocal term. Of course with this ansatz we are only going to obtain an estimate for the free-energy of a possible ferromagnetic state we are testing for. We will have to compare this free-energy to that of other possible phases.

[1] $\hat{\boldsymbol{S}} = (\hat{S}^{(1)}, \hat{S}^{(2)}, \hat{S}^{(3)})^T$ with $\hat{S}^{(j)}$ being the counterpart of $S^{(j)}$ is position space. In this section we drop the subscript of the exchange propagator $M_{1,1}$ and its Fourier transform $\hat{M}$ to keep the notation unencumbered. The symbol $\int_x$ stands for the sum $\frac{1}{\mathrm{V}}\sum_{x\in\mathbb{L}}$ and $\int_{\{x,y\}}$ defines a sum over pairs $\{x,y\}$. In our case $\int_{\{x,y\}} = \frac{1}{2\mathrm{V}^2}\sum_{x,y\in\mathbb{L}}$ •.

Under the assumption of a small external field in the z-direction we will break the spin rotation invariance of the local term by writing it as

$$V_M^{\text{local}} = -\frac{1}{4}M(0)\int_x \hat{\boldsymbol{S}}^2(x) = -\frac{1}{4}M(0)\int_x \left(\hat{S}^{(3)}(x)\right)^2 + \frac{1}{2}M(0)\int_x \left(\hat{S}^{(0)}(x)\right)^2 \tag{4.10}$$

before performing a Hubbard-Stratonovich transformation. It is easier to make this ansatz before bosonization. This way we obtain an isolated extrema later on in the saddle point approximation.

4.4.2 Antiferromagnetic State

In order to estimate the free-energy of an antiferromagnetic state we define

$$\begin{aligned}\zeta^{(1)}_{(i,j)} &= \zeta^{(2)}_{(i,j)} = 1\,,\\ \zeta^{(3)}_{(i,j)} &= (-1)^{i+j}\,,\end{aligned}$$

and write the spin-spin interaction term as

$$\begin{aligned}V_M(\hat{\bar{\psi}},\hat{\psi}) &= -\frac{1}{4}\int_{x,y}\hat{M}(x-y)\,\hat{\boldsymbol{S}}(x)\cdot\hat{\boldsymbol{S}}(y)\\ &= -\frac{1}{8}\int_{x,y}\hat{M}(x-y)\sum_{j=1}^{3}\zeta^{(j)}_{\boldsymbol{x}-\boldsymbol{y}}\Big[-\left(\hat{S}^{(j)}(x)-\zeta^{(j)}_{\boldsymbol{x}-\boldsymbol{y}}\hat{S}^{(j)}(y)\right)^2\\ &\qquad\qquad + \left(\hat{S}^{(j)}(x)\right)^2 + \left(\hat{S}^{(j)}(y)\right)^2\Big] \qquad (4.11)\\ &= \frac{1}{4}\int_{\{x,y\}}\hat{M}(x-y)\sum_{j=1}^{3}\zeta^{(j)}_{\boldsymbol{x}-\boldsymbol{y}}\left(\hat{S}^{(j)}(x)-\zeta^{(j)}_{\boldsymbol{x}-\boldsymbol{y}}\hat{S}^{(j)}(y)\right)^2\\ &\quad -\frac{1}{4}M(Q)\int_x\left(\zeta^{(3)}_{\boldsymbol{x}}\hat{S}^{(3)}(x)\right)^2 + \frac{1}{2}M(0)\int_x\left(\hat{S}^{(0)}(x)\right)^2\,,\end{aligned}$$

where $M(Q) = \int_y \zeta^{(3)}_{\boldsymbol{y}}\hat{M}(y)$ and $Q := (0,\pi,\pi)$. Analogous to the arguments we used for the ferromagnetic state, the nonlocal term can now be assumed to be small if the ground state shows Néel order. In the last line we have made use of $(S^{(j)}(x))^2 = (S^{(0)}(x))^2$. Note the similarity between and, in particular, the presence of the same density-density term in Eq. (4.11) and Eq. (4.10). The factor $\zeta^{(3)}_{\boldsymbol{x}}$ in $(\zeta^{(3)}_{\boldsymbol{x}}\hat{S}^{(3)}(x))^2$ may look irrelevant but we include it to emphasize that the Hubbard-Stratonovich field corresponding to bilinear $\zeta^{(3)}_{\boldsymbol{x}}\hat{S}^{(3)}(x)$ is the gap parameter of the AFM state.

4.4.3 Superconducting State

The fRG calculations signal an instability only in the d-wave superconducting channel and according to [73, 74] in two dimensional case, the dominating part of the interaction in terms of spherical harmonics, determines the global minimum of the mean field free-energy. In our case it is $D_{2,2}$, which may lead to a d-wave superconducting phase in mean-field calculations. Thus, the only relevant term for the Cooper pairing channel at mean-field level is

$$V_C(\bar{\psi},\psi) \approx \int_\ell D_{2,2}(\ell)\bar{C}_2^{(2)}(\ell)C_2^{(2)}(\ell)\,.$$

During the flow, the bosonic propagator $D_{2,2}$ either remains negligible or becomes singular with a sharp peak at the origin in momentum space. Thus we approximate,

$$V_C(\bar{\psi},\psi) \approx \frac{1}{\beta \mathrm{V}} D_{2,2}(0)\bar{C}_2^{(2)}(0)C_2^{(2)}(0)\,.$$

Even though the bare interaction was repulsive, in position space the sharp peak of $D_{2,2}$ at the origin translates to a long-range attractive interaction which is crucial for gap formation in Cooper channel.

4.4.4 The Density-Density Interaction

The contribution of the exchange propagator $K_{1,1}$ to the effective density-density interaction in position space is given by

$$V_K(\hat{\bar{\psi}},\hat{\psi}) = -\frac{1}{4}\int_{x,y} \hat{K}_{1,1}(x-y)\,\hat{S}^{(0)}(x)\hat{S}^{(0)}(y)\,,$$

We write the interaction in the following way, which involves the difference between the density at two different sites and the local interaction,

$$\begin{aligned} V_K &= -\frac{1}{8}\int_{x,y} \hat{K}_{1,1}(x-y)\left[-\left(\hat{S}^{(0)}(x)-\hat{S}^{(0)}(y)\right)^2+\left(\hat{S}^{(0)}(x)\right)^2+\left(\hat{S}^{(0)}(y)\right)^2\right] \\ &= \frac{1}{4}\int_{\{x,y\}} \hat{K}_{1,1}(x-y)\left(\hat{S}^{(0)}(x)-\hat{S}^{(0)}(y)\right)^2+\frac{1}{4}K_{1,1}(0)\int_x\left(\hat{S}^{(0)}(x)\right)^2\,. \end{aligned}$$

Assuming that the density is homogeneous, the first term should be negligible compared to the local one. The onsite density-density interaction can be countered by a shift in chemical potential to maintain van Hove filling. During the flow this is done as described in Section 3.5.

4.4.5 Mean Field Ambiguity

The local interaction vertex can be decomposed into different channels in many different ways. For example, nothing prevents us from writing the s-wave superconducting channel as a pure spin-spin or density-density interaction. This doesn't mean that mean-field theory leads to ambiguous results. Various combination may result in different saddle-points, but in the zero temperature limit the deepest one settles the state. In practice, we don't even compute the free-energy for arbitrary field configurations, but only for few configurations which we suspect to be close to the actual ground state. In our case, these configurations are the ferromagnetic and d-wave superconducting ones. We keep the interaction in different channels as they are after the fRG flow has been stopped and perform Hubbard-Stratonovich transformations. Eq. (4.10) is not an exception from this rule but rather a part of the ferromagnetic ansatz. We cannot test for this state without breaking the spin rotational symmetry. But since the magnetic exchange propagator is rather large, we cannot neglect its contribution to the density-density channel. Note that the decomposition of the interaction does not rely on properties of the Grassmann fields. With this treatment, our results are consistent with generalized Hartree-Fock approximation [75, 14] (see also section 4.6.2). In our calculations, we ignore the bare interaction and the s-wave superconducting exchange propagator which are small compared to the rest.

4.5 Effects of a NFLL Self-Energy on Gap Formation

In keeping with the spirit of the preceding section, we will test for gap formation in the vicinity of the critical hopping parameter at van Hove filling, starting with the simplified local 4-point vertices,

$$\mathcal{V}_{\text{local}}^{\text{FM}} = -\frac{1}{4} M_{1,1}(0) \int_{\ell} S^{(3)}(\ell) S^{(3)}(-\ell) \,,$$
$$\mathcal{V}_{\text{local}}^{\text{dSC}} = \frac{1}{\beta \mathrm{V}} D_{2,2}(0) \bar{C}_2^{(2)}(0) C_2^{(2)}(0) \,,$$

where compared to last section we have Fourier transformed back to momentum space. To keep the notation clean we drop the subscript Ω wherever the scale dependence is clear from the definition of a quantity. The partition function is given by

$$Z \propto \int \mathrm{d}\mu_T(\overline{\Psi}, \Psi)\, \mathrm{e}^{-\mathcal{V}_{\text{local}}^{\text{State}}(\Psi, \overline{\Psi})} \,,$$

similar to Eq. (4.8).

In the FM case we can write the action as $(S^3, AS^{(3)})$, where $(A)_{p,q} = \frac{-M(0)}{4}\delta(p+q)$. However, since A is not positive definite we cannot use a real HS Transformation based on Eq. (4.1). Instead we split the diagonal from the rest, and perform both a real and a complex HS transformation according to Eq. (4.1) and Eq. (4.2) respectively,

$$Z \propto \int \mathrm{d}\phi_0 \prod_{p\neq 0} \mathrm{d}\phi_p \overline{\phi}_p \, \mathrm{e}^{-\frac{\beta \mathrm{V}}{M_{1,1}(0)}\phi_0^2 - \frac{1}{M_{1,1}(0)}\int_{p\neq 0}\phi_p\overline{\phi}_p} \int \mathrm{d}\mu_T(\overline{\psi},\psi)\, \mathrm{e}^{\int_{p\neq 0}(\phi_p+\overline{\phi}_{-p})S^{(3)}(p)+\phi_0 S^{(3)}(0)} .$$

We now approximate the field ϕ by its static value $\Delta_{\mathrm{FM}} = \phi_0$ and neglect fluctuations in the following saddle-point approximation. After integrating out the fermions we obtain,

$$Z \propto \int \mathrm{d}\Delta_{\mathrm{FM}}\, \mathrm{e}^{-\beta \mathrm{V} F_{\mathrm{FM}}} ,$$

where the exponent is given by

$$F_{\mathrm{FM}} = \frac{1}{M_{1,1}(0)}\Delta_{\mathrm{FM}}^2 - \sum_{\sigma\in\{+,-\}}\int_p \ln\bigl(1+\sigma\Delta_{\mathrm{FM}}T(p)\bigr) .$$

For the Cooper interaction a complex HS transformation yields,

$$Z \propto \int \mathrm{d}\Delta_{\mathrm{dSC}} \wedge \mathrm{d}\overline{\Delta}_{\mathrm{dSC}}\, \mathrm{e}^{-\beta \mathrm{V} F_{\mathrm{dSC}}} ,$$

with

$$F_{\mathrm{dSC}} = \frac{1}{D_{2,2}(0)}|\Delta_{\mathrm{dSC}}|^2 - \int_p \ln\Bigl(1+|\Delta_{\mathrm{dSC}}|^2 f_2^2(\boldsymbol{p})\,T(p)\,T(-p)\Bigr) .$$

F_{dSC} and F_{FM} play the role of the free-energy per degree of freedom relative to the free-energy of the paramagnetic phase. In the thermodynamic limit and at zero temperature the saddle point with the dominant exponent (smallest free-energy) determines the phase of the system.

$T(k)$ is given in Eq. (4.9). The self-energy entering the equations is the self-energy at scale Ω which in the vicinity of the critical hopping and at van Hove filling, can be parametrized as [2]

$$\mathrm{Im}\,\Sigma_\Omega(\omega)/\omega = -\frac{a}{(1+b^2\omega^2)^{\gamma/2}} , \tag{4.12}$$

[2] The difference in minus sign lies in different definitions of self-energy compared to [48].

where a, b and γ depend on the hopping amplitude and the scale parameter [48]. The right-hand side blends into a constant approximately as the frequencies drop below the stopping scale. Within the static mean-field approximation we cannot calculate the small frequency behavior of the self-energy and incorporate it. To compensate for the loss we can use the extrapolation of the fRG data. By assuming that the extrapolation is the correct asymptotic behavior, we compute the gaps also using

$$\operatorname{Im}\Sigma^{\text{ext.}}_{\Omega}(\omega)/\omega = -a(b^2\omega^2)^{-\gamma/2}\,. \tag{4.13}$$

At small stopping scales the difference we see in the order parameter using either version becomes negligible. If we remove the regulator we recover the toy-model of Section 4.2 (c.f. Eq. (4.13) and Eq. (4.3)).

The saddle point conditions are,

$$\begin{aligned}\Delta_{\text{FM}} &= \frac{M_{1,1}(0)}{2}\int\limits_{k,\sigma}\frac{\sigma}{T^{-1}(k)+\sigma\Delta_{\text{FM}}}\,,\\ 1 &= D_{2,2}(0)\int\limits_{k}\frac{f_2^2(\boldsymbol{k})}{T^{-1}(k)T^{-1}(-k)+f_2^2(\boldsymbol{k})\left|\Delta_{\text{dSC}}\right|^2}\,,\end{aligned}$$

and the order parameter $O_{\text{dSC}} = 2\Delta_{\text{dSC}}/D_{2,2}(0)$, $O_{\text{FM}} = 2\Delta_{\text{FM}}/M_{1,1}(0)$ are the expectation values of the bilinears

$$\begin{aligned}\widehat{O}_{\text{FM}} &= \int\limits_{k,\sigma}\sigma\,\overline{\Psi}_{k,\sigma}\Psi_{k,\sigma}\,,\\ \widehat{O}_{\text{dSC}} &= \frac{1}{2}\int\limits_{k,\sigma}\sigma\,f_2(\boldsymbol{k})\overline{\Psi}_{k,\sigma}\overline{\Psi}_{-k,-\sigma}\,,\end{aligned}$$

defined in terms of the scaled Grassmann variables 4.3.

For the numerics we use the fRG data given in Table 4.1. The corresponding order-parameters are shown in Table 4.3 and Figure 4.3. In the range $t'/t \in (0.34, 0.38)$, where $\gamma \lessapprox 0.26$, both order parameters vanish within numerical tolerance which confirms the existence of a QCP in this parameter region. Within the numerics two effects are responsible for the QCP: on the one hand the self-energy pushes the development of the pairing interaction to very small scales in flow, and on the other hand it hinders gap formation in MF calculations as we already saw in the toy-model of Section 4.2. Of course these effects are tightly coupled since in the absence of symmetry breaking we should be able to

drive the flow to arbitrary small scales as long as higher order loop interaction remain negligible.

The free energies at the saddle points are listed in Table 4.2. Up to $t'/t \approx 0.34$ the superconducting phase is clearly dominant. For $t'/t > 0.38$ even tough it was not evident from fRG data, there is a strong competition between the superconducting phase and the ferromagnetic one. Only in the calcualtions with the extrapolated self-energy, the free-energy of the ferromagnetic phase becomes significantly smaller and settles the state.

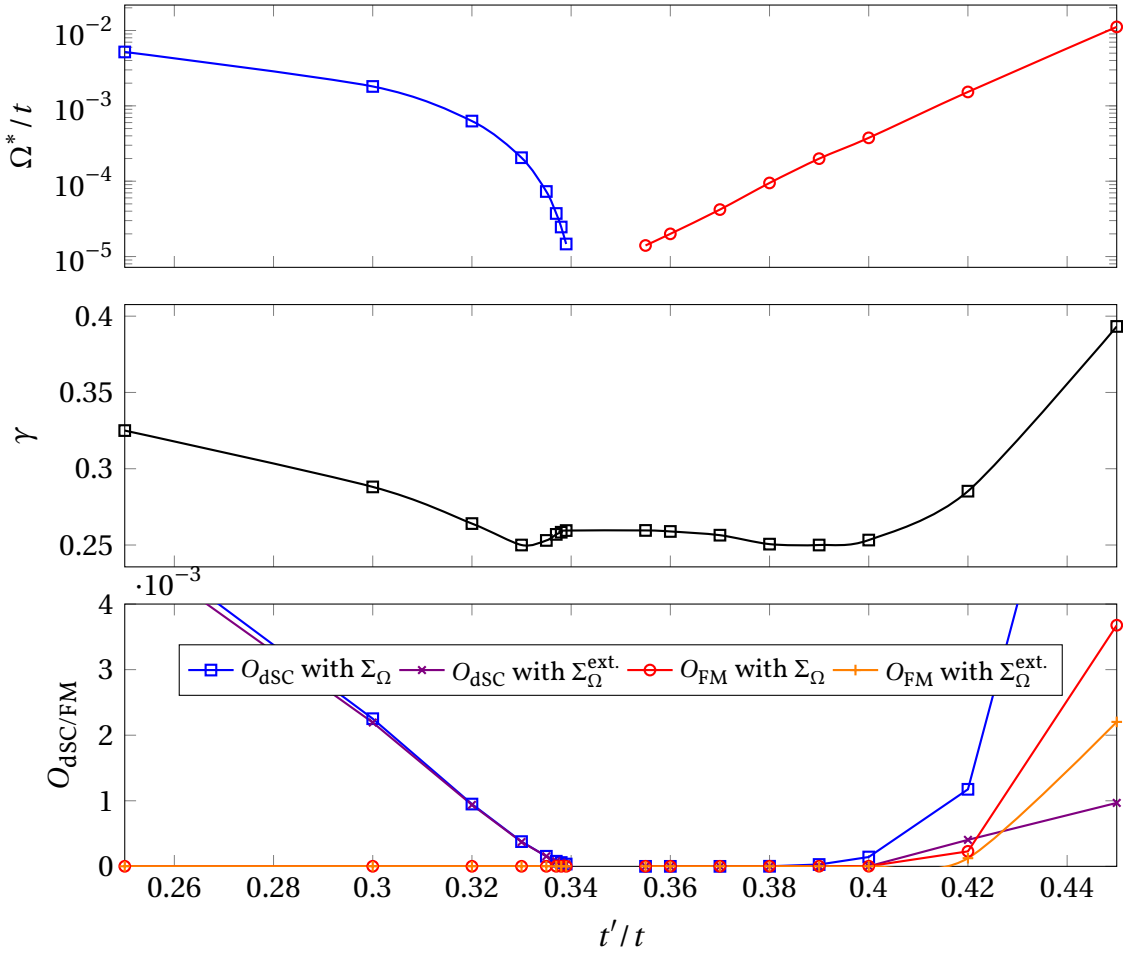

Figure 4.3: The stopping scale Ω^*, critical exponent of the free-energy γ and order parameters O_{dSC}, O_{FM} as a function of hopping parameter t'/t. In the range $(0.34, 0.38)$ the order parameters vanish.

t'/t	$\log_{10}\Omega^*/t$	a	$\log_{10} b$	γ	$D_{2,2}(0)/t$	$M_{1,1}(0)/t$
0.250	−2.28	1.19	1.83	0.325	20.0	4.18
0.300	−2.74	1.60	2.34	0.288	20.0	5.75
0.320	−3.20	2.17	2.89	0.264	20.0	7.44
0.330	−3.69	2.93	3.42	0.250	20.0	9.54
0.335	−4.14	4.30	4.20	0.253	20.0	11.8
0.337	−4.43	5.49	4.49	0.257	20.0	13.3
0.338	−4.61	5.91	4.56	0.258	20.0	14.4
0.339	−4.83	6.24	4.61	0.259	20.0	15.7
0.355	−4.85	6.27	4.62	0.260	0.05	20.0
0.360	−4.70	6.07	4.59	0.259	0.06	20.0
0.370	−4.38	5.33	4.47	0.256	0.09	20.0
0.380	−4.02	3.57	3.81	0.251	0.17	20.0
0.390	−3.70	2.95	3.43	0.250	0.26	20.0
0.400	−3.42	2.42	3.04	0.253	0.36	20.0
0.420	−2.82	1.67	2.40	0.285	0.55	20.0
0.450	−1.95	0.88	1.09	0.393	0.64	20.0

Table 4.1: Data from the fRG flow at the stopping scale Ω^* for various hopping parameters t'/t and bare interaction $U = 3/t$. This results have been computed in previous studies by K. Giering, C. Husemann and M. Salmhofer and partially published in [48], [45] and [49] (we use the same notation as in [67] which differs by factor two in the definition of the bosonic propagators from the other references.). a, b and γ parametrize the self-energy according to Eq. (4.12). $D_{2,2}$ and $M_{1,1}$ are the exchange propagators describing the d-wave Cooper and magnetic interaction, c.f. Eq. (3.7).

t'/t	O_{dSC} with Σ_Ω	O_{dSC} with $\Sigma_\Omega^{\mathrm{ext.}}$	O_{FM} with Σ_Ω	O_{FM} with $\Sigma_\Omega^{\mathrm{ext.}}$
0.250	$5.1\cdot10^{-3}$	$4.9\cdot10^{-3}$	$<10^{-6}$	$<10^{-6}$
0.300	$2.3\cdot10^{-3}$	$2.2\cdot10^{-3}$	$<10^{-6}$	$<10^{-6}$
0.320	$9.5\cdot10^{-4}$	$9.4\cdot10^{-4}$	$<10^{-6}$	$<10^{-6}$
0.330	$3.8\cdot10^{-4}$	$3.7\cdot10^{-4}$	$<10^{-6}$	$<10^{-6}$
0.335	$1.5\cdot10^{-4}$	$1.5\cdot10^{-4}$	$<10^{-6}$	$<10^{-6}$
0.337	$7.8\cdot10^{-5}$	$7.8\cdot10^{-5}$	$<10^{-6}$	$<10^{-6}$
0.338	$5.8\cdot10^{-5}$	$5.7\cdot10^{-5}$	$<10^{-6}$	$<10^{-6}$
0.339	$3.5\cdot10^{-5}$	$3.4\cdot10^{-5}$	$<10^{-6}$	$<10^{-6}$
0.355	$<10^{-10}$	$<10^{-10}$	$<10^{-6}$	$<10^{-6}$
0.360	$<10^{-10}$	$<10^{-10}$	$<10^{-6}$	$<10^{-6}$
0.370	$<10^{-10}$	$<10^{-10}$	$<10^{-6}$	$<10^{-6}$
0.380	$1.4\cdot10^{-6}$	$<10^{-10}$	$<10^{-6}$	$<10^{-6}$
0.390	$2.8\cdot10^{-5}$	$<10^{-10}$	$2.1\cdot10^{-6}$	$<10^{-6}$
0.400	$1.4\cdot10^{-4}$	$1.2\cdot10^{-6}$	$2.1\cdot10^{-6}$	$<10^{-6}$
0.420	$1.2\cdot10^{-3}$	$4.\cdot10^{-4}$	$2.3\cdot10^{-4}$	$1.2\cdot10^{-4}$
0.450	$9.7\cdot10^{-3}$	$9.7\cdot10^{-4}$	$3.7\cdot10^{-3}$	$2.2\cdot10^{-3}$

Table 4.2: Order parameters computed from the fRG data listed in Table 4.1. Upper bounds are given when the quantity is too small to be computed reliably due to finite numerical precision.

t'/t	F_{dSC}/t with Σ_Ω	F_{dSC}/t with $\Sigma_\Omega^{\mathrm{ext.}}$	F_{FM}/t with Σ_Ω	F_{FM}/t with $\Sigma_\Omega^{\mathrm{ext.}}$
0.250	$-1.2\cdot10^{-4}$	$-1.\cdot10^{-4}$	≈ 0	≈ 0
0.300	$-2.3\cdot10^{-5}$	$-2.\cdot10^{-5}$	≈ 0	≈ 0
0.320	$-4.\cdot10^{-6}$	$-3.6\cdot10^{-6}$	≈ 0	≈ 0
0.330	$-5.9\cdot10^{-7}$	$-5.3\cdot10^{-7}$	≈ 0	≈ 0
0.335	$-9.2\cdot10^{-8}$	$-8.9\cdot10^{-8}$	≈ 0	≈ 0
0.337	$-2.5\cdot10^{-8}$	$-2.3\cdot10^{-8}$	≈ 0	≈ 0
0.338	$-1.3\cdot10^{-8}$	$-1.2\cdot10^{-8}$	≈ 0	≈ 0
0.339	$-4.2\cdot10^{-9}$	$-3.7\cdot10^{-9}$	≈ 0	≈ 0
0.355	≈ 0	≈ 0	≈ 0	≈ 0
0.360	≈ 0	≈ 0	≈ 0	≈ 0
0.370	≈ 0	≈ 0	≈ 0	≈ 0
0.380	≈ 0	≈ 0	≈ 0	≈ 0
0.390	$-5.9\cdot10^{-12}$	≈ 0	$-1.2\cdot10^{-12}$	≈ 0
0.400	$-3.1\cdot10^{-10}$	≈ 0	$-5.3\cdot10^{-11}$	≈ 0
0.420	$-6.\cdot10^{-8}$	$-2.2\cdot10^{-9}$	$-5.2\cdot10^{-8}$	$-1.\cdot10^{-8}$
0.450	$-5.8\cdot10^{-6}$	$-7.6\cdot10^{-9}$	$-8.5\cdot10^{-6}$	$-2.\cdot10^{-6}$

Table 4.3: Mean-field free-energy per degree of freedom at the saddle point of the bosonic action normalized to the free-energy of a gap-less state.

4.6 Mean-Field Calculations in the Density-Density Channel

In Section 4.5 we showed that in the vicinity of the QCP magnetic ordering and Cooper pairing both become negligible. In this section we assume that we are in the quantum critical regime and investigate the effects of the density-density interaction on the propagator. As shown in Figure 4.4 during the flow the effective interaction develops a strong peak in the scattering channel at a finite frequency. In the simplest approximation we project the effective interaction to a sum of delta distributions at zero frequency and finite frequencies $\pm\tilde{\omega}$. The zero frequency part will give rise to a Hartree self-energy, which we compensate by appropriate choice of the chemical potential to ensure van Hove filling.

4.6.1 Introduction

In the density-density channel, depending on the sing of the interaction, the bosonic action obtained from a HST according to Eq. (4.1) may not have a saddle point on the real axis. Provided that the action is holomorphic in the HS field we may be able to find a saddle point in the complex plane and deform the integration contour to pass through the saddle point without altering its result. The zero temperature asymptotic of the partition and correlation functions would then follow from the following lemma. For holomorphic functions f and S, consider the Laplace transform,

$$F(\lambda) = \int_\gamma f(z)\, \mathrm{e}^{\lambda S(z)}\, \mathrm{d}z \,.$$

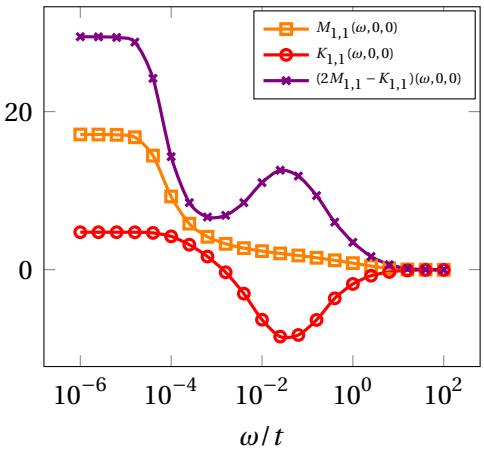

Figure 4.4: Effective interaction in magnetic and scattering channel at the scale $\Omega/t = 3\times10^{-5}$ for the bare interaction $U/t = 3$ at van Hove filling and the critical hopping amplitude. Combining two channels, the overall density-density interaction $U + (2M_{1,1} - K_{1,1})(\omega,0,0)$ is peaked at some finite frequency. Presented data are from calculations performed by the author. In contrast to those used in previous section, they take the momentum dependence of self-energy into account.

If S has a single simple saddle point at an interior point z_0 of the integration contour γ, then the $\lambda \to \infty$ asymptotic of $F(\lambda)$ is given by

$$F(\lambda) = \sqrt{\frac{2\pi}{-S''(z_0)}}\lambda^{-1/2}\,\mathrm{e}^{\lambda S(z_0)}\left(f(z_0) + \mathcal{O}\left(\lambda^{-1}\right)\right).$$

Hence the saddle-point method consists of a *topological* part, which is finding a suitable contour γ which may not exist, and an *analytic* part which involves the evaluation of the asymptotic behavior of the Laplace transform $F(\lambda)$.

For our purpose a constant shift of the integration contour is sufficient to make sure that the contour passes through the saddle point of the exponent. In particular we can formulate the HST (4.1) in the more general form

$$\mathrm{e}^{a^2/4} = \frac{1}{\sqrt{\pi}}\int_{\mathbb{R}} \mathrm{e}^{-(\phi+\mathrm{i}c)^2+(\phi+\mathrm{i}c)a}\,\mathrm{d}\phi\,, \tag{4.15}$$

where c is an arbitrary real number. Since the integrand $f : \phi \to \exp(-\phi^2 + \phi a)$ has no poles Eq. (4.15) follows from the identity

$$\int_{-R}^{R} f(\phi)\mathrm{d}\phi + \int_0^c f(R+\mathrm{i}\,t)\mathrm{d}t - \int_{-R}^{R} f(\phi+\mathrm{i}\,c)\mathrm{d}\phi - \int_0^c f(-R+t)\mathrm{d}t = 0\,.$$

in the limit $R \to \infty$.

In the case of a complex HST the generalization is as follows,

$$\mathrm{e}^{ab} = \int_{\mathbb{C}} \mathrm{e}^{-(\phi+\mathrm{i}\psi)(\overline{\phi}+\mathrm{i}\overline{\psi})+a(\phi+\mathrm{i}\psi)+b(\overline{\phi}+\mathrm{i}\overline{\psi})}\,\frac{\mathrm{d}\phi\wedge\mathrm{d}\overline{\phi}}{2\pi\,\mathrm{i}}\,, \tag{4.16}$$

where $\psi \in \mathbb{C}$ is an arbitrary complex number. The proof is simple, let $\phi = u + \mathrm{i}\,v$, $\psi = x + \mathrm{i}\,y$ with $u, v, x, y \in \mathbb{R}$, then

$$\begin{aligned} I &= \int_{\mathbb{C}} \mathrm{e}^{-(\phi+\mathrm{i}\psi)(\overline{\phi}+\mathrm{i}\overline{\psi})+a(\phi+\mathrm{i}\psi)+b(\overline{\phi}+\mathrm{i}\overline{\psi})}\,\frac{\mathrm{d}\phi\wedge\mathrm{d}\overline{\phi}}{2\pi\,\mathrm{i}} \\ &= \int_{\mathbb{R}^2} \mathrm{e}^{-(u+\mathrm{i}x)^2-(v+\mathrm{i}y)^2+(a+b)(u+\mathrm{i}x)+\mathrm{i}(a-b)(v+\mathrm{i}y)}\,\frac{\mathrm{d}u\wedge\mathrm{d}v}{\pi}\,, \end{aligned}$$

Eq. (4.16) now follows from Eq. (4.15),

$$I = \mathrm{e}^{(a+b)^2/4-(a+b)^2/4} = \mathrm{e}^{ab}\,.$$

As long as the integrals in Eq. (4.15) and Eq. (4.16) are considered exactly they are

independent of c and ψ, but only for suitable values of these quantities —lets call them c' and ψ'— can the integrals be evaluated in saddle point approximation. Through the analytic structure of the interand, the integral then depdedns on this specific values c' and ψ'.

4.6.2 Connection to Generalized Hartree-Fock Theory

For the mean density per site q and the mean magnetization m it is known from generalized Hartree-Fock theory [75] that the minimization of the grand canonical free-energy of the Hubbard model is equivalent to the min-max problem

$$F_{\mathrm{HF}} = \min_m \max_q F(q,m)\,,$$

where in the limit $\beta \to \infty$ (c.f. [14, Eq. 14]),

$$F = -\frac{U}{4}(q-1)^2 + \frac{U}{4}m^2 - \frac{1}{2}\int_{\boldsymbol{k},\sigma}\left|\epsilon(\boldsymbol{k}) - \mu + \frac{U}{2}(q+\sigma m)\right|. \tag{4.17}$$

In the following we will demonstrate how these equations can be derived using the HST and how the maximization prescription emerge in our case.

The partition function of the bare Hubbard model is given by

$$Z \propto \int \mathrm{d}\phi_0 \mathrm{d}\Delta_0 \prod_{p\neq 0} \mathrm{d}\phi_p \overline{\phi}_p \mathrm{d}\Delta_p \overline{\Delta}_p \, \mathrm{e}^{-\frac{\beta \mathrm{V}}{U}(\phi_0+\mathrm{i}c)^2 - \frac{1}{U}\int_{p\neq 0}\phi_p\overline{\phi}_p - \frac{\beta \mathrm{V}}{U}\Delta_0^2 - \frac{1}{U}\int_{p\neq 0}\Delta_p\overline{\Delta}_p}$$
$$\int \mathrm{d}\mu_C(\overline{\psi},\psi)\, \mathrm{e}^{\mathrm{i}\int_{p\neq 0}(\phi_p+\overline{\phi}_{-p})S^{(0)}(p) + \mathrm{i}(\phi_0+\mathrm{i}c)S^{(0)}(0) + \int_{p\neq 0}(\Delta_p+\overline{\Delta}_{-p})S^{(3)}(p) + \Delta_0 S^{(3)}(0)}\,,$$

where $U/t > 0$ is the onsite repulsive interaction. In a saddle point approximation the density is given by

$$q = -\frac{1}{\beta \mathrm{V}}\langle S^{(0)}(0)\rangle = -\mathrm{i}\,\frac{2}{U}(\phi_0 + \mathrm{i}\,c) \tag{4.18}$$

which depends on c. Assuming that $\Delta(p \neq 0) \approx 0$, $\phi(p \neq 0) \approx 0$ and taking into account only the static part of the bosonic fields we deduce

$$Z \propto \int \mathrm{d}\phi_0 \mathrm{d}\Delta_0 \, \mathrm{e}^{-\frac{\beta \mathrm{V}}{U}(\phi_0+\mathrm{i}c)^2 - \frac{\beta \mathrm{V}}{U}\Delta_0^2 + c + \frac{1}{2}\sum_{\sigma=\pm 1}\sum_{\boldsymbol{p}}|\epsilon(\boldsymbol{p})-\mu+c+\sigma\Delta_0|}\,.$$

It is evident that the saddle point is at $\phi_0 = 0$, which is desirable since the density (4.18) should be a real quantity. Since we are not integrating over c the positive

sign of the quadratic term c^2 in the exponent does not cause any harm. Finally the mean-field solution is given by the saddle point of the function

$$F = -\frac{1}{U}\left(c - \frac{U}{2}\right)^2 + \frac{1}{U}\Delta_0^2 - \frac{1}{2}\int_{\boldsymbol{p},\sigma} \left|\epsilon(\boldsymbol{p}) - \mu + c + \sigma\Delta_0\right| + \text{const.}\,, \tag{4.19}$$

which, due to the sign of the c^2 term, poses a min-max problem rather than a pure minimization problem. By taking the derivative with respect to c we obtain

$$c = \frac{U}{4}\sum_{\sigma=\pm1}\int_{\boldsymbol{p}} \left(-\text{sgn}\big(\epsilon(\boldsymbol{p}) - \mu + c + \sigma\Delta_0\big) + 1\right) = \frac{U}{2}\int_{\boldsymbol{p},\sigma} \Theta\big(-\epsilon(\boldsymbol{p}) - \mu - c - \sigma\Delta_0\big)\,,$$

which is the Hartree self-energy. The optimization function (4.19) coincides with Eq. (4.17) with $c = \frac{U}{2}q$ and $\Delta_0 = \frac{U}{2}m$.

4.6.3 Mean-Field Equation for a Frequency and Momentum Dependent Density-Density Interaction

We consider an action involving a density-density interaction of the form [3]

$$S(\widetilde{\psi},\psi) = -\int_{\omega\boldsymbol{p}s} \overline{\psi}_{\omega\boldsymbol{p}s}(\mathrm{i}\omega - \epsilon_{\boldsymbol{p}} + \mu)\psi_{\omega\boldsymbol{p}s} + \frac{1}{4}\int_p K(p)S^{(0)}(p)S^{(0)}(-p)\,, \tag{4.20}$$

which does not depend on the non-transfer frequency and momenta. In the following we assume K to be real and symmetric with respect to $\omega \to -\omega$. For the bare Hubbard model K would be positive and constant. Next we write the interaction term from Eq. (4.20) as

$$-\frac{1}{4}\int_p K(p)S^{(0)}(p)S^{(0)}(-p) = -\frac{1}{4}\frac{1}{\beta V}K(0)S^{(0)}(0)^2 - \frac{1}{2}\frac{1}{\beta V}\sum_{p>0} K(p)S^{(0)}(p)S^{(0)}(-p)\,,$$

where ">" denotes the lexicographical order on the product space $\mathbb{M}_{\text{Bosonic}} \times \Gamma^*$. Making the reflection symmetry explicit is not strictly necessary but it reduces the number of HS fields we need to define. Proceeding according to Eq. (4.15,4.16) we obtain the mixed action

$$\begin{aligned}
&S_{\text{H.S.}} = \\
&-\frac{1}{\beta \mathrm{V}}\sum_{\omega\boldsymbol{p}s} \widetilde{\psi}_{\omega\boldsymbol{p}s}(\mathrm{i}\omega - \epsilon_{\boldsymbol{p}} + \mu)\psi_{\omega\boldsymbol{p}s} \\
&+ \beta \mathrm{V}\frac{\Phi_0^2}{|K(0)|} - \mathrm{i}\, I_K(0)\Phi_0 S^{(0)}(0) \\
&+ 2\beta \mathrm{V}\sum_{p>0}\frac{\Phi(p)\widetilde{\Phi}(p)}{|K(p)|} - \mathrm{i}\sum_{p>0}\left(I_K(p)S^{(0)}(p)\Phi(p) + I_K(-p)S^{(0)}(-p)\widetilde{\Phi}(p)\right),
\end{aligned}$$

[3] K is some generic density-density interaction and should not be confused with $K_{1,1}$.

where

$$I_f(x) = \mathrm{e}^{\mathrm{i}\arg(\mathrm{f}(\mathrm{x}))/2} = 1 \quad \text{if} \quad f(x) \geq 0 \quad \text{else} \quad \mathrm{i} \quad \text{for} \quad f(x) \in \mathbb{R}\,.$$

The field Φ includes a possible shift of the integration contour. To be precise $\Phi_0 = \phi_0 + \mathrm{i}\psi_0$ with $\phi_0, \psi_0 \in \mathbb{R}$ and for $p > 0$, $\Phi(p) = \phi(p) + \mathrm{i}\psi(p), \widetilde{\Phi}(p) = \overline{\phi}(p) + \mathrm{i}\overline{\psi}(p)$ with $\phi(p), \psi(p) \in \mathbb{C}$. ϕ is the HS field and the field ψ has to be chosen such that the integration contours pass through saddle points of the action.

Integrating out the fermions leads to the free-energy,

$$\begin{aligned} F = & \frac{\Phi_0^2}{|K(0)|} + 2\sum_{p>0} \frac{\Phi(p)\widetilde{\Phi}(p)}{|K(p)|} \\ & - \frac{2}{\beta \mathrm{V}} \ln\det\Big[(\mathrm{i}\, p_0 - \epsilon_{\boldsymbol{p}} + \mu + \mathrm{i}\, I_K(0)\Phi_0)\delta_{p,p'} \\ & - \mathrm{i}\big(I_K(p-p')\Phi(p-p')\Theta(p-p'>0) + I_K(p'-p)\widetilde{\Phi}(p'-p)\Theta(p'-p>0)\big)\Big]_{p,p'} \\ & + C\,, \end{aligned} \tag{4.21}$$

where $C = \frac{2}{\beta \mathrm{V}} \ln\det\Big[(\mathrm{i}\, p_0 - \epsilon_{\boldsymbol{p}} + \mu)\delta_{p,p'} \Big]_{p,p'}$ is a normalziation constant.

In the general case the determinant is too complex to be computed. The usual ansatz is to keep only the static part of the bosonic field. We will go a step further and take into account the field at some finite frequency $\tilde{\omega}$. The determinant can be computed efficiently using the following technique.

4.6.4 The Determinant of a Tridiagonal Matrix and its Generalization

It is well known that the determinant $f_n = \det T_n$ of a tridiagonal matrix

$$T_n = \begin{pmatrix} a_1 & b_1 & & & \\ c_1 & a_2 & b_2 & & \\ & c_2 & \ddots & \ddots & \\ & & \ddots & \ddots & b_{n-1} \\ & & & c_{n-1} & a_n \end{pmatrix}$$

satisfied the recurrence relation

$$\begin{aligned} f_{-1} &= 0\,, \\ f_0 &= 1\,, \\ f_n &= a_n f_{n-1} - c_{n-1} b_{n-1} f_{n-2}\,. \end{aligned}$$

This relation can can be generalized as follows. Let T_n be a matrix of order $n \times n$ of the form

$$(T_n)_{ij} = \begin{cases} a_i & \text{if} \quad i = j \\ b_i & \text{if} \quad j = i + k \\ c_j & \text{if} \quad i = j + k \\ 0 & \text{otherwise} \end{cases}.$$

For each n let $d = \gcd(k, n)$, $n' = n/d$ and $k' = k/d$. The map

$$[m]_{n,k} := \left\lfloor \frac{m-1}{n'} \right\rfloor + \big(k(m-1) \bmod n\big) + 1 \tag{4.22}$$

defines a permutation which can be used to transform T_n into a tridiagonal matrix. This transformation can be used to compute the determinant of T_n efficiently. In particular if,

$$\begin{aligned} f_{-1} &= 0\,, \\ f_0 &= 1\,, \\ f_m &= a_{[m]_{n,k}} f_{m-1} - c_{[m-1]_{n,k}} b_{[m-1]_{n,k}} f_{m-2}\,, \end{aligned} \tag{4.23}$$

then $\det T_n = f_n$.

Proof: Every element $m \in \{1, 2, \ldots, n\}$ can be represented as $m = \ell n' + r + 1$ where $\ell = \left\lfloor \frac{m-1}{n'} \right\rfloor$ and $r = ((m-1) \bmod n')$. We define an isomorphism $m \mapsto [m]_{n,k} = (\ell + kr \bmod n) + 1$. The matrix elements of $(T'_n)_{i,j} := (T_n)_{[i]_{n,k},[j]_{n,k}}$ can only be nonzero if $((i-j) \bmod n') \le 1$. Thus $T'_n = \mathrm{diag}(A_0, A_1, \ldots, A_{d-1})$ is block diagonal and each block is of the form

$$A_\ell = \begin{pmatrix} \tilde{a}_1^{(\ell)} & \tilde{b}_1^{(\ell)} & & & \tilde{c}_{n'}^{(\ell)} \\ \tilde{c}_1^{(\ell)} & \tilde{a}_2^{(\ell)} & \tilde{b}_2^{(\ell)} & & \\ & \tilde{c}_2^{(\ell)} & \ddots & \ddots & \\ & & \ddots & \ddots & \tilde{b}_{n'-1}^{(\ell)} \\ \tilde{b}_{n'}^{(\ell)} & & & \tilde{c}_{n'-1}^{(\ell)} & \tilde{a}_{n'}^{(\ell)} \end{pmatrix},$$

where

$$\tilde{b}^{(\ell)}_{n'} = (T_n)_{[\ell n'+n']_{n,k},[\ell n'+1]_{n,k}} = (T_n)_{\ell+n-k+1,\ell+1}\,,$$
$$\tilde{c}^{(\ell)}_{n'} = (T_n)_{[\ell n'+1]_{n,k},[\ell n'+n']_{n,k}} = (T_n)_{\ell+1,\ell+n-k+1}\,.$$

Either $n \neq 2k$, then both $\tilde{b}^{(\ell)}_{n'}$ and $\tilde{c}^{(\ell)}_{n'}$ are zero or $n = 2k$, then the blocks A_ℓ are 2×2 matrices. In both cases T'_n is tridiagonal and its determinant which is equal to the determinant of T_n is given by Eq. (4.22).

4.6.5 Numerical Setup

We make the following ansatz for Φ,

$$\Phi(p) = \Phi_{\tilde{\omega}}\delta_{p_0,\tilde{\omega}}\delta_{\boldsymbol{p},0}\,,$$
$$\widetilde{\Phi}(p) = \widetilde{\Phi}_{\tilde{\omega}}\delta_{p_0,\tilde{\omega}}\delta_{\boldsymbol{p},0}\,.$$

So in addition to the static field Φ_0 at zero frequency the free-energy depends on $\Phi_{\tilde{\omega}}$ and $\widetilde{\Phi}_{\tilde{\omega}}$, which incorporates a dependence on K at the finite frequency $\tilde{\omega}$. The free-energy (4.21) now reads

$$\begin{aligned} F =& \frac{\Phi_0^2}{|K(0)|} + 2\frac{\Phi_{\tilde{\omega}}\widetilde{\Phi}_{\tilde{\omega}}}{|K(\tilde{\omega})|} \\ & - \frac{2}{\beta \mathrm{V}}\sum_{\boldsymbol{p}} \ln\det\Big[(\mathrm{i}\,p_0 - \epsilon_{\boldsymbol{p}} + \mu + \mathrm{i}\,I_K(0)\Phi_0)\delta_{p_0,p_0'} \\ & \qquad - \mathrm{i}\,I_K(\tilde{\omega})\left(\Phi_{\tilde{\omega}}\,\delta_{p_0-p_0',\tilde{\omega}} + \widetilde{\Phi}_{\tilde{\omega}}\,\delta_{p_0'-p_0,\tilde{\omega}}\right)\Big]_{p_0,p_0'} \\ & + C\,. \end{aligned} \tag{4.24}$$

Independent of whether $K(0)$ is positive or negative we can adjust the chemical potential to ensure van Hove filling. Then at the saddle point of Φ_0 we have $\mu + \mathrm{i}\,I_K(0)\Phi_0 = 0$. At fixed density we only need to find the saddle point of F as a function of $\Phi_{\tilde{\omega}}$ and $\widetilde{\Phi}_{\tilde{\omega}}$. We evaluate the determinant using Eq. (4.23) on the discretized Euclidean time axis $\mathbb{T}_n := \{-\beta/2 + \beta k/n : k \in \{0,\dots,n-1\}\}$ (c.f. 3.2). For fixed Φ_0 and at van Hove Filling F is then up a constant given by the $n\to\infty$ limit of

$$\begin{aligned} F_n =& 2\frac{\Phi_{\tilde{\omega}}\widetilde{\Phi}_{\tilde{\omega}}}{|K(\tilde{\omega})|} - \frac{2}{\beta}\int_{\boldsymbol{p}} \ln\det\Big[(\mathrm{i}\check{\omega}_k - \epsilon_{\boldsymbol{p}})\delta_{k,k'} - \mathrm{i}\,I_K(\tilde{\omega})\left(\Phi_{\tilde{\omega}}\,\delta_{k-k',m} + \widetilde{\Phi}_{\tilde{\omega}}\,\delta_{k'-k,m}\right)\Big]_{k,k'} \\ & + C\,, \end{aligned}$$

where

$$\breve{\omega}_k = -\mathrm{i}\frac{n}{\beta}\left(1-\mathrm{e}^{-\mathrm{i}\pi(2k-1)/n}\right) \qquad \text{(3.2 revisited)}$$

and $\tilde{\omega} = \frac{2\pi}{\beta}m$, for some fixed $m \in \{1,\dots,n-1\}$.

F_n depends on the HS fields $\Phi_{\tilde{\omega}}$ and $\widetilde{\Phi}_{\tilde{\omega}}$ only through their product. For the determinant this follows from Eq. (4.23). As a result any non-trivial saddle point of F as a function of $\Phi_{\tilde{\omega}}$ or $\widetilde{\Phi}_{\tilde{\omega}}$ is a saddle point of F as a function of $\Phi_{\tilde{\omega}}\widetilde{\Phi}_{\tilde{\omega}}$,

$$\frac{\partial F}{\partial \Phi_{\tilde{\omega}}} = \widetilde{\Phi}_{\tilde{\omega}}\frac{\partial F}{\partial(\Phi_{\tilde{\omega}}\widetilde{\Phi}_{\tilde{\omega}})} \stackrel{!}{=} 0\,.$$

To summarize, we need to find the saddle point of $F_n(K(\tilde{\omega}), z)$ as a function of $z = \Phi_{\tilde{\omega}}\widetilde{\Phi}_{\tilde{\omega}}$ given through

$$\begin{aligned}
F_n(\tilde{K};z) &= 2\frac{z}{|K(\tilde{\omega})|} - f_n^{\mathrm{sgn}(\tilde{K})}(z)\,,\\
f_n^{\pm}(z) &= \frac{2}{\beta}\int\frac{\mathrm{d}\epsilon}{(2\pi)^2}\rho(\epsilon)\ln f_n^{\pm}(z,\epsilon)\,,\\
f_{-1}^{\pm}(z,\epsilon) &= 0 \quad , \quad f_0^{\pm}(\epsilon) = 1\,,\\
f_m^{\pm}(z,\epsilon) &= f_{m-1}^{\pm}(z,\epsilon) \pm z\frac{\delta_{|[i]_{n,k}-[j]_{n,k}|,m}\, f_{m-2}^{\pm}(z,\epsilon)}{\left(\mathrm{i}\breve{\omega}(2[i]_{n,k})-\epsilon\right)\left(\mathrm{i}\breve{\omega}(2[j]_{n,k})-\epsilon\right)}\,,
\end{aligned} \qquad (4.25)$$

where $\rho(e) = \int_{[-\pi,\pi)^2}\delta(\epsilon(\boldsymbol{k})-e)\mathrm{d}^2\boldsymbol{k}$ is the density of states.

The following symmetry considerations can greatly reduce the numerical effort. First, since

$$f_n^{+}(z) = f_n^{-}(-z)\,,$$

if z_0 is a saddle point of $F_n(\tilde{K},z)$ then $-z_0$ is a saddle point of $F_n(-\tilde{K};z)$. So we may restrict ourselves to case $\tilde{K} = K(\tilde{\omega}) > 0$ in the following.

Second, it easy to show that

$$\overline{F_n(\tilde{K},z)} = F_n(\tilde{K},\overline{z})\,. \qquad (4.26)$$

Thus, for fixed $\tilde{K}$, if $z \in \mathbb{R}$ then $F_n(\tilde{K};z)$ is real.

Let $z = x+\mathrm{i}\,y$ and $f : z \mapsto F_n(\tilde{K};z) = u(x,y)+\mathrm{i}\,v(x,y)$ with $x,y,u,v \in \mathbb{R}$. Let $z_0 = x_0+\mathrm{i}\,0$ and f be holomorphic at z_0 then if $\frac{\partial u}{\partial x}(x_0,0) = 0$ since $\frac{\partial v}{\partial x}(x_0,0) = 0$ (becasue of Eq. (4.26)), it follows from Cauchy-Riemann equations that $f'(z_0) = 0$, i.e. z_0 is a saddle point of f if x_0 is a saddle point of $f|_{\mathbb{R}}$.

4.6.6 The Quasiparticle Lifetime

Since we are interested in saddle points of the free-energy F_n in the limit $n \to \infty$ we will first study how f_n^+ (c.f. Eq. (4.25)) depends on n. Let us fix $m = 1$. Figure 4.5a shows $f_n^+(z)$ as a function of z for different values of n. As n grows we notice a convergence and for $-50 < z < 0$ we consider $n = 10^4$ to be large enough to represent the $n \to \infty$ limit with reasonably small error. This applies also to different choices of m.

Now we fix $n = 10^4$ and explore the dependence on m or equivalently the finite bosonic frequency $\tilde{\omega} = 2\pi m/\beta$ at which we consider a finite density-density interaction $\tilde{K} > 0$. Fig. 4.5b depicts $f_n^+(z)$. In order to find a saddle point of F_n we need to solve the equation

$$2\frac{1}{|K(\tilde{\omega})|} \stackrel{!}{=} \left(f_n^{\mathrm{sgn}(\mathrm{K}(\tilde{\omega}))}\right)'(z)\,. \tag{4.27}$$

At first glance for large enough $K > 0$ the equation might have a single negative and in addition several positive solutions if $m > 1$. Recalling that $z = \Phi\widetilde{\Phi}$ and that $\Phi = \phi + \mathrm{i}\psi, \widetilde{\Phi} = \overline{\phi} + \mathrm{i}\overline{\psi}$, a negative value would correspond to a saddle point where the HS field ϕ is equal to zero and the integration contours of the integrals over $\mathrm{Re}\,\phi$ and $\mathrm{Im}\,\phi$ have been shifted into the complex plane by the offsets $\mathrm{Re}\,\psi$ and $\mathrm{Im}\,\psi$ (c.f. Eq. (4.16)). A positive value corresponds to a saddle point where $\psi = 0$. Since all saddle points with a specific sign of z lie on the same integration contour it is much easier to evaluate the integral at the one negative solution of Eq. (4.27). According to our symmetry considerations in the case $\tilde{K} < 0$ we would have one positive solution. With this choice in both cases $\tilde{K} < 0$ and $\tilde{K} > 0$ the off-diagonal elements of the matrix in Eq. (4.21) are real at the saddle point.

The derivatives $\left(f_n^{\pm}\right)'(0^{\mp})$ are finite. Furthermore the inequality $\left(f_n^+\right)'(z) \leq \left(f_n^+\right)'(0^-)$ holds for $z < 0$. Similarly we have $\left|\left(f_n^-\right)'(z)\right| \leq \left|\left(f_n^-\right)'(0^+)\right|$ for $z \geq 0$. Thus, according to Eq. (4.27) the existence of a non-trivial saddle point requires a minimal interaction strength

$$|K(\tilde{\omega})| \geq \lim_{\substack{z\uparrow 0 \text{ if } K(\tilde{\omega})>0 \\ z\downarrow 0 \text{ if } K(\tilde{\omega})<0}} \frac{2}{\left(f_n^{\mathrm{sgn}(\tilde{K})}\right)'(z)}\,.$$

The dependence of the position of the saddle-point as a function of interaction strength $K(\tilde{\omega})$ is shown in Figure 4.5c. It shows only a weak dependence on m for small $m \leq 10$.

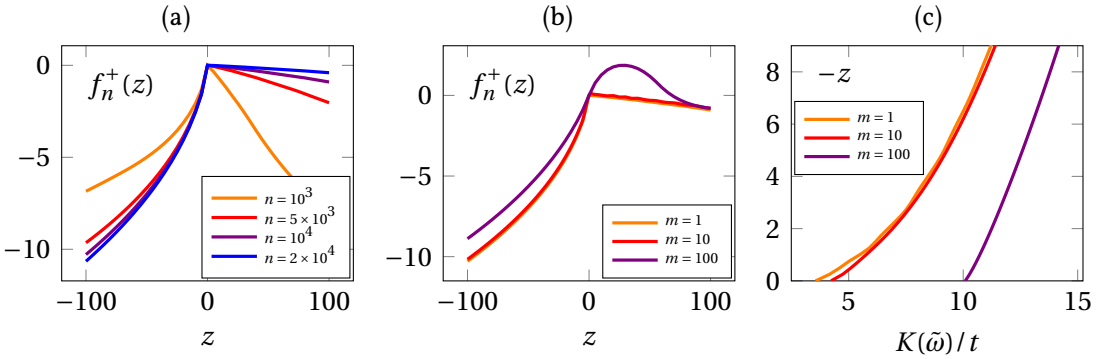

Figure 4.5: (a) f_n^+ defined in Eq. (4.25) for $\beta = 100/t$, $\tilde{\omega} = 2\pi/\beta$ (i.e. $m = 1$) and different values of $n = \#\mathbb{T}_n$. For $-50 < z < 0$, $n = 10^4$ seems to be sufficient to assume that we are numerically in the large n limit. (b) f^+ for $n = 10^4$, $\beta = 100/t$ and different values of $\tilde{\omega} = 2\pi m/\beta$. (c) Position of the saddle point as a function of $K(\tilde{\omega})$ according to Eq. (4.27). The curves corresponding to $m = 1$ and $m = 10$ lie almost on top of each other.

All measurable quantities should be independent of the sign of $K(\tilde{\omega})$ for a finite frequency $\tilde{\omega}$ because of translational invariance along the Euclidean time axis and the periodicity of the interaction. This is of course also the case for the fermionic propagator. Let $\zeta = \sqrt{|z|}$ at the saddle point of the free-energy. In terms of the fields $\Phi_{\tilde{\omega}}, \widetilde{\Phi}_{\tilde{\omega}}$ for $K(\tilde{\omega}) \leq 0$ the saddle point is at $\Phi_{\tilde{\omega}} = \zeta, \widetilde{\Phi}_{\tilde{\omega}} = \zeta$ and for $K(\tilde{\omega}) > 0$ at $\Phi_{\tilde{\omega}} = \mathrm{i}\zeta, \widetilde{\Phi}_{\tilde{\omega}} = \mathrm{i}\zeta$. We will show that the propagator is the same in both cases.

Imagine adding a source term $-\frac{1}{2}\int_{p\sigma} j_p \overline{\psi}_{p\sigma}\psi_{p\sigma}$ to the action (4.20) in the beginning. j would then enter the free-energy (4.24) as an additive term to the dispersion,

$$F = \frac{-2}{\beta \mathrm{V}} \sum_{\boldsymbol{p}} \ln\det \Bigg[\Big(\mathrm{i}\, p_0 - \epsilon_{\boldsymbol{p}} + \frac{j_p}{2} + \mu + \mathrm{i}\, I_K(0)\Phi_0 \Big)\delta_{p_0,p_0'} - \mathrm{i}\, I_K(\tilde{\omega}) \Big(\Phi_{\tilde{\omega}}\, \delta_{p_0 - p_0', \tilde{\omega}} + \widetilde{\Phi}_{\tilde{\omega}}\, \delta_{p_0' - p_0, \tilde{\omega}} \Big) \Bigg]_{p_0, p_0'} + j\text{-independent terms}\,.$$

The fermionic propagator is then given by the expectation value of the derivative of the partition function with respect to the source term j. In a saddle point

approximation it is the diagonal of

$$G = \left[(\mathrm{i}\, p_0 - \epsilon_{\boldsymbol{p}}) \delta_{p,p'} + \zeta \left(\delta_{p_0 - p_0', \tilde{\omega}} + \delta_{p_0' - p_0, \tilde{\omega}} \right) \right]^{-1}_{p,p'} =$$
$$\left[\delta_{p_0,p_0'} + \zeta \frac{\left(\delta_{p_0 - p_0', \tilde{\omega}} + \delta_{p_0' - p_0, \tilde{\omega}} \right)}{\sqrt{\mathrm{i}\, p_0 - \epsilon_{\boldsymbol{p}}} \sqrt{\mathrm{i}\, p_0' - \epsilon_{\boldsymbol{p}'}}} \delta_{\boldsymbol{p},\boldsymbol{p}'} \right]^{-1}_{p,p'} \cdot \left[\frac{\delta_{p,p'}}{\sqrt{\mathrm{i}\, p_0 - \epsilon_{\boldsymbol{p}}} \sqrt{\mathrm{i}\, p_0' - \epsilon_{\boldsymbol{p}'}}} \right]_{p,p'} . \tag{4.28}$$

As expected it does not depend on the sign of $K(\tilde{\omega})$. If we consider the propagator G as a function of the sum and difference of the two involved frequencies, i.e. $\omega_\pm = p_0 \pm p_0'$, i.e. $G_{p,p'} = \delta_{\boldsymbol{p},\boldsymbol{p}'} G_{\epsilon(\boldsymbol{p})}(\omega_-, \omega_+)$. Then $G_\epsilon(\omega_-, \omega_+)$ is non-zero only when ω_- is a multiple of $\tilde{\omega}$. For fixed ϵ and ω_+, $G_\epsilon(\omega_-, \omega_+)$ decays as $|\omega_-|$ grows.

The fermionic propagator $g(p) = g_{\epsilon(\boldsymbol{p})}(p_0)$ is given by $g_\epsilon(\omega) := G_\epsilon(0, 2\omega)$. For $\zeta = 0$ according to Eq. (4.28), $g^{-1} = \mathrm{i}\check{\omega} - \epsilon$. This result already includes the static self-energy which cancels out the chemical potential. For finite values of ζ or equivalently corresponding interaction strength $K(\tilde{\omega})$ the propagator develops some non-trivial structure most prominent around $\omega = \tilde{\omega}$. $\tilde{\omega}$ is itself not on the frequency lattice as it is a bosonic frequency. An example of the imaginary part of the Dyson self-energy $\Sigma = c^{-1} - g^{-1}$ with $c = (\mathrm{i}\check{\omega} - \epsilon)^{-1}$ is shown in Figure 4.6. The behavior of the self-energy changes at multiples of $\tilde{\omega}$. The strongest peak between $\tilde{\omega}$ and $2\tilde{\omega}$ can be fitted well with a model $a(\omega - \tilde{\omega})^\alpha$ with $\alpha \approx -1$. A pole at $\omega = \pm\tilde{\omega}$ would translate to a discontinuity in time domain,

$$\mathscr{F}_\omega^{-1} \left[-\mathrm{i} \left(\frac{1}{\omega - \tilde{\omega}} + \frac{1}{\omega + \tilde{\omega}} \right) \right] (\tau) = -\sqrt{(2\pi)} \cos(\tilde{\omega}\tau) \mathrm{sgn}(\tau) .$$

The inverse Fourier transform of the free propagator to Euclidean time in the limit $\zeta \to 0$ is given by

$$\frac{1}{\beta} \sum_n \mathrm{e}^{-\mathrm{i}\omega_n \tau} c_\epsilon(\omega) = \begin{cases} \mathrm{e}^{-\epsilon\tau} f_\beta(\epsilon) & \text{if} \quad -\beta < \tau \leq 0 \\ -\mathrm{e}^{-\epsilon\tau} (1 - f_\beta(\epsilon)) & \text{if} \quad 0 < \tau < \beta \end{cases} .$$

In the interacting case with $\zeta = 0.5$ and $m = 8$ $(\tilde{\omega}/t \approx 0.5)$ the result is shown in figure 4.7a. The effect of the periodic density-density interaction $K(\tilde{\omega})$ is evident in the correlation function which now shows m distinct peaks. The inverse Fourier transform of the self-energy is shown in Figure 4.7b. It is remarkably simple compared to the self-energy in frequency space. Taking the limit $n \to \infty$ numerically it has a single discontinuity at $\tau = 0$ in the interval $[-\beta, \beta)$.

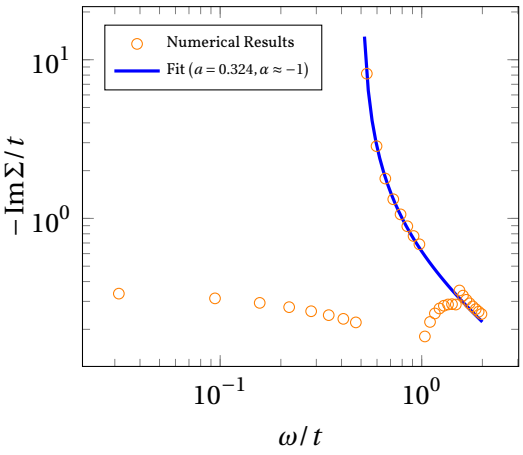

Figure 4.6: Imaginary part of the Dyson self-energy computed with $\zeta = 0.5, m = 8, n = 10^4$. The plot shows only the low frequency regime for $\epsilon = 0$. The data points in the range $\tilde{\omega} < \omega < 2\tilde{\omega}$ define the most prominent structure in the self-energy. They can be fitted well by $a(\omega - \tilde{\omega})^{\alpha}$ with an $\alpha \approx -1$.

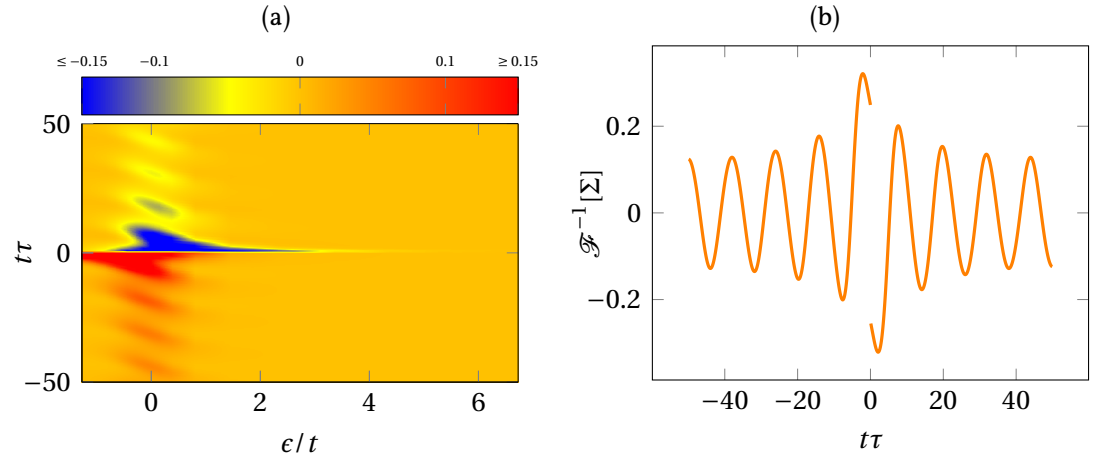

Figure 4.7: (a) Full propagator as a function of Euclidean time for $\zeta = 0.5, m = 8, n = 10^4$. The periodic density-density interaction generated a pattern with m peaks in the correlation function. (b) Fourier transform of the self-energy at $\epsilon = 0$.

To understand the overall effect of the self-energy better, we integrate over frequency to obtain the spin resolved density

$$n(\epsilon) = \frac{1}{\beta} \sum_n g_\epsilon(\omega_n)$$

as a function of the energy. The result is shown in Figure 4.8a for multiple values of ζ which are equivalent to different values of the interaction $K(\tilde{\omega})$. In the limit

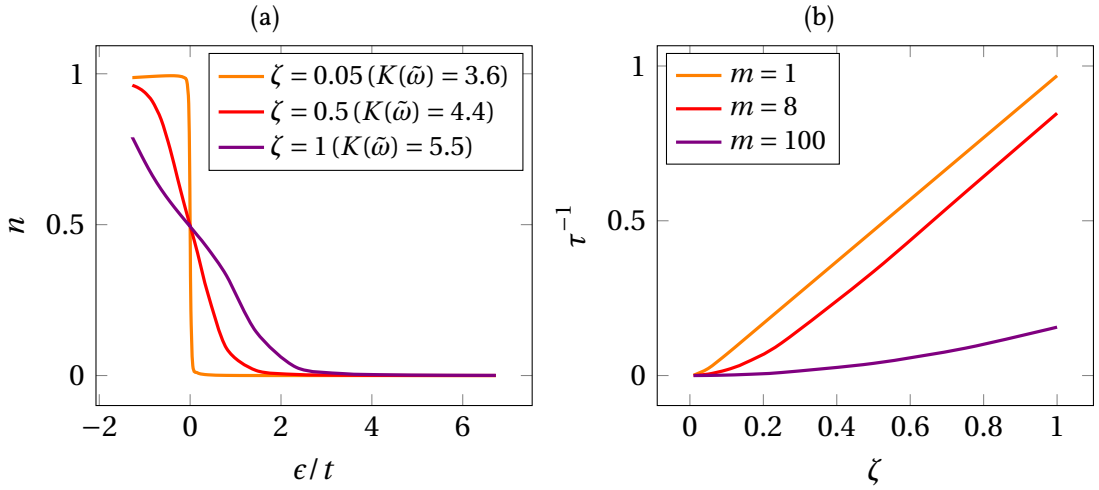

Figure 4.8: (a) Spin resolved density for $m = 8, n = 10^4$ and various values of ζ. Due to the self-energy the density gets smeared out. The effect becomes more evident as we increase ζ which is equivalent to choosing a stronger interaction $K(\tilde{\omega})$. (b) Inverse quasiparticle weight as a function of ζ for different values of m.

$\zeta \to 0$ we obtain a Fermi distribution while increasing ζ smeared out the density strongly around the Fermi level.

For small frequencies the imaginary part of the self-energy is approximately constant but discontinuous at the origin. Close to the Fermi surface and for small frequencies the full propagator behaves as

$$g \approx \frac{1}{\mathrm{i}\breve{\omega} - \epsilon_p + \mathrm{i}\,\mathrm{sgn}(\omega)\tau^{-1}}$$

where τ can be interpreted as the quasiparticle lifetime. Figure 4.8b shows τ^{-1} as a function of the ζ. In the limit $\zeta \to 0$ the quasiparticle lifetime diverges but as ζ or equivalently the interaction strength grows the quasiparticle lifetime becomes finite and drops rapidly. This is in full agreement with the assumption of criticality in this parameter regime.

4.7 Final Remarks

We showed that in the repulsive 2D-Hubbard model gap formation is suppressed in the vicinity of the critical hopping parameter $\theta^\star = 0.341$ and at van Hove

filling. The quantum-critical behavior is tightly related to the low-frequency asymptotic of the self-energy around the van Hove points. Previous fRG studies suggest a power-law behavior $\sim (-)\mathrm{sgn}(\omega)|\omega|^{\alpha}$ with $\alpha \approx 0.74$. The fRG fining is based on the extrapolation of the self-energy at some finite stopping scale. In principle it could be possible to recover the low-frequency structure of the self-energy from mean-field calculations but the involved determinant is very challenging. We computed the self-energy in a rough approximation taking into account only a single frequency density-density interaction and showed the such a feature in the interaction is in agreement with a short quasiparticle lifetime.

Taking the full frequency dependence of density-density interaction account, in principle it seems possible to compute the free-energy at $T = 0$ using the Nyström equation for the Fredholm determinant [76]. We have performed some tests which show that the computational cost is reasonably small if the momentum sums are performed on a small enough grid. But we encountered hard problems which require investigation. First, the Nyström method implies certain assumptions of the solution which might be false. Second, finding the extrema of the free-energy in a high dimensional space is challenging.

Chapter 5

Complementary Considerations and Conclusions

Before we draw conclusions, there are some important points to investigate. Some points are directed towards answering open questions posed by our studies so far. Others aim to address what might be of concern for future analysis.

5.1 Consistency of the NFLL Self-Energy

As mentioned in Section 1.3 the solution of the self-energy flow equation (1.13) is an approximation which solves the exact self-energy SDE (1.3) (c.f. (3.9)) up to third order in the four-point 1PI vertex. Thus, it should include contributions from the two-loop sun-set diagram. At this point it is useful to run through the the details and reveal how two-loop self-energy corrections are encoded in our one-loop flow equation. The scale derivative of the self-energy is given by

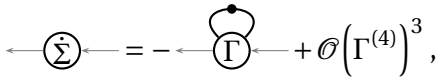

where the curve with the dot in the middle represents the single scale propagator S. Substituting $S = \dot{G} + G\dot{\Sigma}G$ and replacing $\dot{\Sigma}$ by means of iteration yields

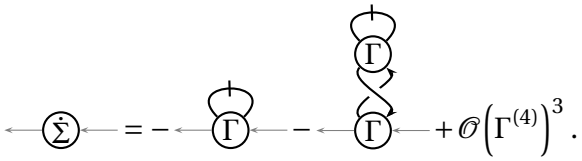

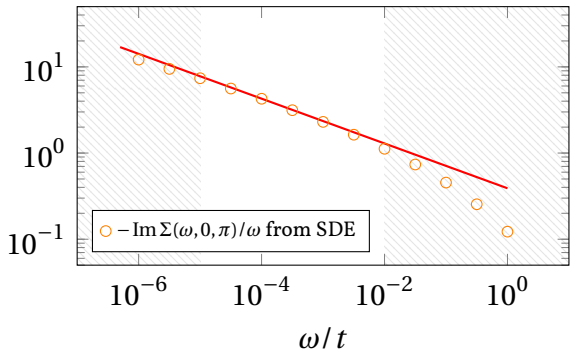

Figure 5.1: The imaginary part of the self-energy as a function of frequency. The fit to the fRG data and the self-energy calculated from the SDE (1.3) match reasonably well in an intermediate frequency region.

Now if we substitute the four-point 1PI vertex in the first term on the right-hand side according to

$$\Gamma^{(4)} = v + \mathbb{S}\left\{\frac{1}{2}\Gamma^{(4)} \circ \Pi_G \circ \Gamma^{(4)} - 2\Gamma^{(4)} * \Upsilon_G * \Gamma^{(4)}\right\} + \mathcal{O}\left(\Gamma^{(4)}\right)^3, \qquad \text{(1.10a revisited)}$$

we obtain

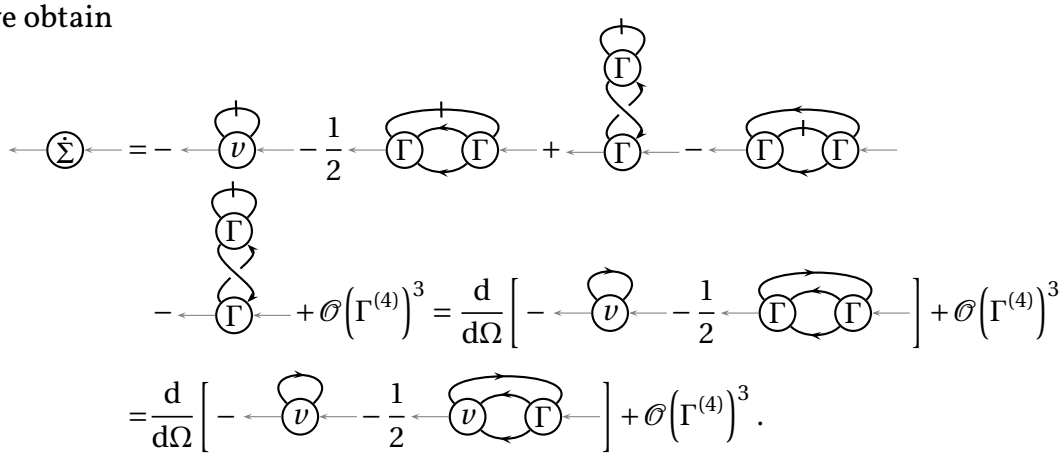

So the solution of the one-loop flow equation includes contributions from the sun-set diagram. The NFLL frequency behavior of the self-energy in our fRG calculations originates from the two-loop diagram and is consistent with the exact SDE up to $\mathcal{O}\left(\Gamma^{(4)}\right)^3$. Note that,

$$\frac{1}{2}G[\![v \circ \Pi_G \circ \Gamma^{(4)}]\!] - \frac{1}{2}G[\![\Gamma^{(4)} \circ \Pi_G \circ \Gamma^{(4)}]\!] = \mathcal{O}\left(\Gamma^{(4)}\right)^3.$$

The magnetic exchange propagator is approximated by $M_{1,1}(\omega,0,0) \approx m|\omega|^{-\kappa}$ with $\kappa \approx 0.13$ in some intermediate frequency regime $10^{-3} < \omega/t < 10^{-1}$ [49].

For a simple consistency check, we neglecting the momentum dependence of the magnetic exchange propagator. Figure 5.1 then shows the self-energy calculated numerically from SD equation (1.3) compared to the extrapolated fRG asymptotic. Recalling that $M_{1,1}(\omega,0,0) \sim |\omega|^{-\kappa}$ is only valid in some finite interval, the behavior of the vertex and self-energy are consistent in the relevant frequency regime.

5.2 fRG with Frequency and Momentum Dependent Self-Energy

Alongside the highly optimized fRG integration routine used in Chapter 3 we developed a new program which allows the computation of the full self-energy during the flow. The momentum and frequency dependence of the exchange propagators and the feedback of the self-energy to the flow is taken into account. The inclusion of the imaginary self-energy requires Matsubara integrals to be evaluated numerically, which increases the computational complexity by about a factor of hundred. The real part of the self-energy lead to deformation of the Fermi surface and increases the numerical cost for reliable evaluation of momentum integrals by at least one more order of magnitude.

The momentum dependence of the imaginary part of the self-energy is merely an improvement over previously obtained results [48], [45] and [49]. The real part of the self-energy even though it was estimated to be small in [49], is of great interest. In particular at van Hove filling the deformation of the Fermi surface may have a strong effect on the instabilities. We will check the stability of the solution at the QCP and the effect of the self-energy on the ferromagnetic instability which is susceptible to changes in density (c.f. Chapter 3, Figure 3.2).

The setup is similar to Chapter 3. The exchange propagators are computed at representative points. The momentum variables are discretized in the same way as in the static case and for the frequency variable we use a logarithmic grid $\{10^k | k \in c\mathbb{Z}, a \leq k \leq b\}$. a is chosen so that 10^a is much smaller than the stopping scale, typically -6 and $b = 2$ is large enough to capture the momentum dependence of the interaction vertex and the self-energy.

5.3 Full Self-Energy at the QCP

The momentum dependence of self-energy at the scale [1] $\Omega/t = 1.4 \times 10^{-4}$ in the limit of small frequencies is shown in Figure 5.2. The absolute value of the imaginary part of the self-energy is the largest at the van Hove points and drops by a factor of over two towards the center and the corners of the Brillouin zone. The frequency dependence of the self-energy at three points $\{(\pi,0),(0,0),(\pi,\pi)\}$ is shown in Figure 5.3. At the van Hove Point $(\pi,0)$ we observe the NFLL asymptotic $-\mathrm{sgn}(\omega)|\omega|^{0.74}$ but not at other momenta.

The real part of the self-energy lead to a small deformation of the Fermi-surface as shown in Figure 5.4. It is important to consider that the deformation of the Fermi surface at the van Hove points is induced by the second derivative of the self-energy at these points. The accuracy of these derivatives is limited due to the patching. In fact, based on the estimations by Feldman and Salmhofer [69] the derivatives are divergent in the limit $\beta \to \infty$. We can verify this numerically by computing the derivatives with the regulator removed as a function of inverse temperature. The result is shown in Figure 5.5. As far as the fRG is concerned, the derivatives are finite at finite scales, and the impact of the deformation on the flow seems negligible within our patching scheme and approximations.

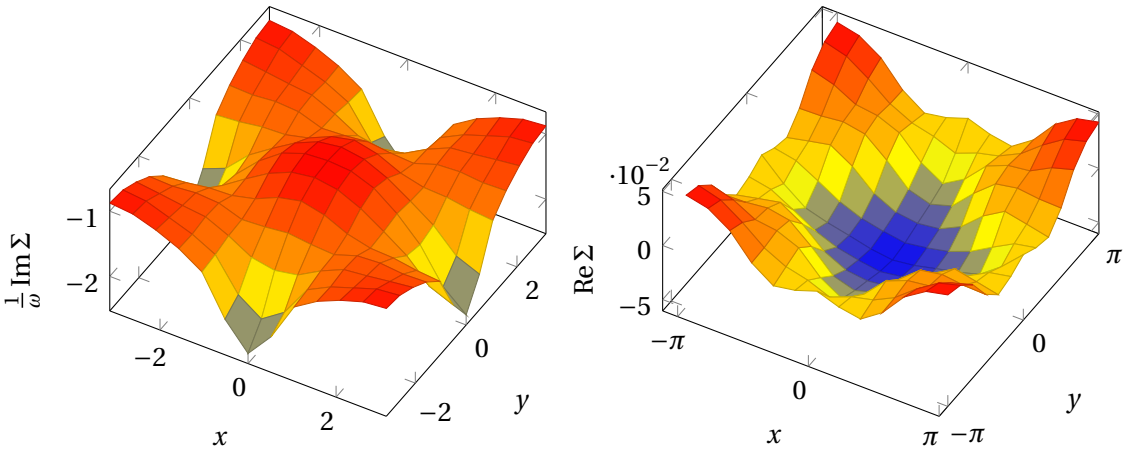

Figure 5.2: Momentum dependence of real and imaginary parts of the self-energy at the stopping scale $\Omega/t = 1.7 \times 10^{-4}$ and for $\omega/t = 10^{-6}$.

[1] At smaller scales we cannot evaluate the bubble integrals reliably anymore.

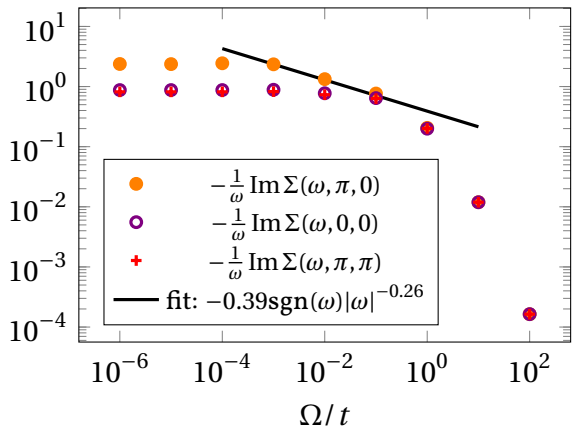

Figure 5.3: Frequency dependence of the imaginary part of the self-energy at the scale $\Omega/t = 1.4 \times 10^{-4}$. At the van Hove point $(\pi,0)$ the frequency dependence converges to the NFLL behavior $\mathrm{Im}\,\Sigma \sim (-)\mathrm{sgn}(\omega)|\omega|^{0.74}$. The flat part $\omega < \Omega^*$ is due to the regulator.

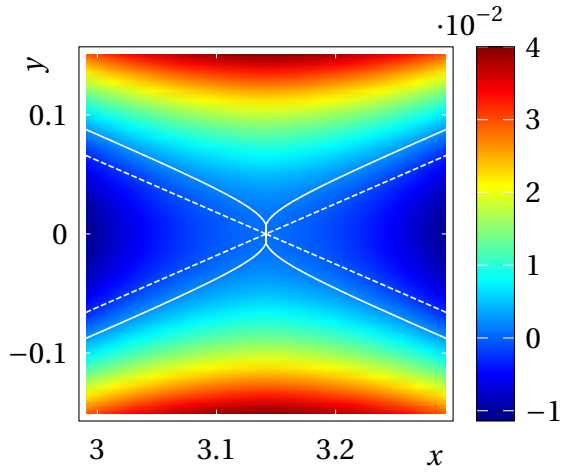

Figure 5.4: The color map shows $\epsilon(x,y) + \mathrm{Re}\,\Sigma(\omega = 0, x, y)$ in the vicinity of the van Hove point $(\pi,0)$ at the stopping scale $\Omega/t = 1.7 \times 10^{-4}$. The dashed curve shows the Fermi-surface without and the solid line with self-energy.

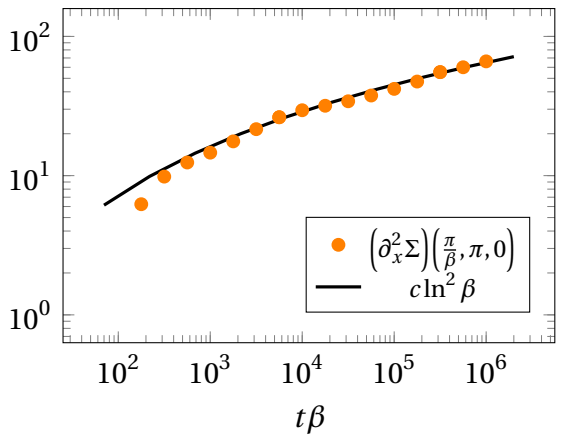

Figure 5.5: Second derivative of self-energy up to a constant as a function of inverse temperature. The curvature diverges logarithmically in the limit $\beta \to \infty$.

5.4 Density-Density Interaction Away From the QCP

In conjunction with Section 4.6 one may ask whether the particular form of the density-density interaction with a notable peak at some finite frequency (c.f. Figure 4.4) is specific to the QCP or not. Figure 5.6 shows the density-density interaction strength $(2M_{1,1} - K_{1,1})(\omega, 0, 0)$ for different values of the hopping parameter at vHF. There is always a peak at some finite frequency in the forward scattering channel descried by $K_{1,1}$ which finds its way into the overall density-density interaction, but mean-field treatments in the manner of Section 4.6 do not apply directly to points away from the QCP since they were based on the assumption that the ground state is not symmetry broken. For mean-field calculations one would have to incorporate possibly frequency dependent gap parameters and take into account their interplay with the density wave. Right now this is beyond our numerical capacities.

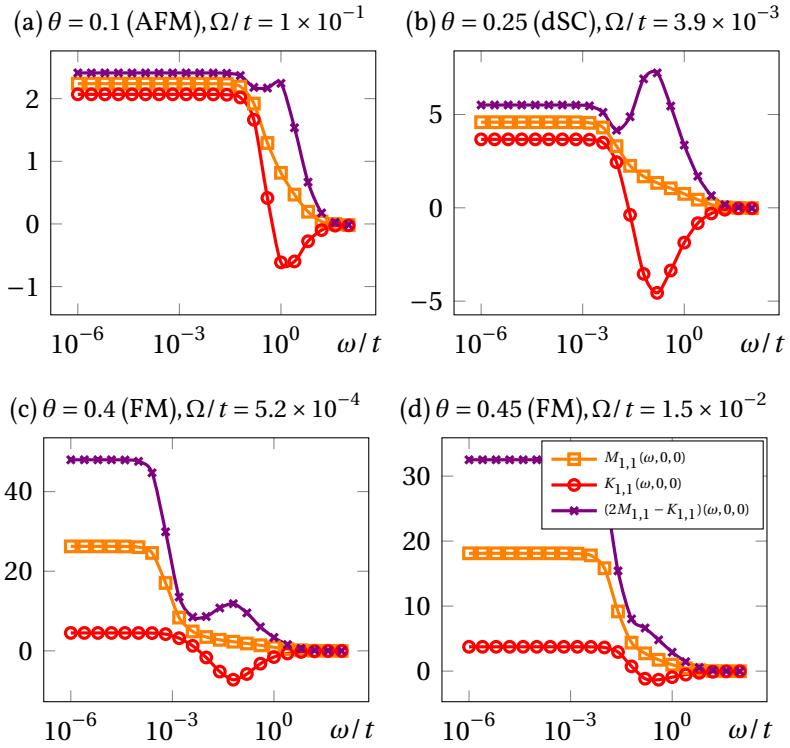

Figure 5.6: Density-Density interaction at vHF but away from the QCP. There is always a peak at some finite frequency at low scales.

5.5 Ferromagnetic Instability Away From van Hove Filling

In Chapter 3 we showed that within the stationary vertex approximation the ferromagnetic instability is confined to a narrow region close to van Hove filling and large next-nearest-neighbor hopping amplitudes. The phase diagram was given in Figure 3.2. We already pointed out that the $\mu < 0$ region is most likely dominated by Antiferromagnetic tendencies. For $\mu > 0$ and $t > 0.37$ we see no divergence in the flow up to $\Omega/t = 10^{-6}$ and assume a superconducting ground state due to the Kohn-Luttinger effect. In this region we have to check for self-energy effects. In particular the real-part of the self-energy may affect the instabilities here. Furthermore, close to the critical point and for $\mu > 0$ one may also suspect the self-energy effects to be important. In this case the imaginary part might affect ordering, for instance suppress the Cooper instability. We have checked that both are not the case. Figure 5.7.a shows the ferromagnetic coupling during the flow for $t'/t = 0.45$ and $\mu/t \in \{0, 0.05, 0.1\}$. The results for smaller hopping parameters look similar. $M_{1,1}$ diverges for $\mu = 0$, and the instability disappears quickly as we move away from van Hove filling. Figure 5.7.b shows the exchange propagators $M_{1,1}(0,0,0)$ and $D_{2,2}(0,0,0)$ close to the critical point for $\mu/t = 0.05$ at $\Omega/t = 10^{-3}$. Compared to Chapter 3 we cannot follow the flow to lower scales without loosing too much numerical precision. But from the flow up to $\Omega^*/t = 10^{-3}$ we can deduce that the ferromagnetic coupling remains stable. The Cooper interaction strength decreases for growing hopping amplitudes but as long as it is positive it will most likely diverge at some smaller scale. We conclude that the dominant instability is the d-wave superconductor and the instability diagram 3.2 remains unchanged (although the scale at which the couplings would diverge is much smaller than in the static vertex approximation).

5.6 An Alternative Regulating Function

In Section 3.4 we mentioned that the regulator in the Ω-scheme has a pole in the upper-half complex plane which contributes a residue to the frequency integral of the tadpole term. Similarly one has to be careful when evaluating the mean-field free-energy or other Matsubara sums where the summand decays like $\check{\omega}^{-1}$ in the limit $\omega \to \infty$. When all integrals are treated carefully the results are consistent, yet we may explore the possibility of choosing a regulator which is analytic in the upper-half complex plane. Since real valued functions have

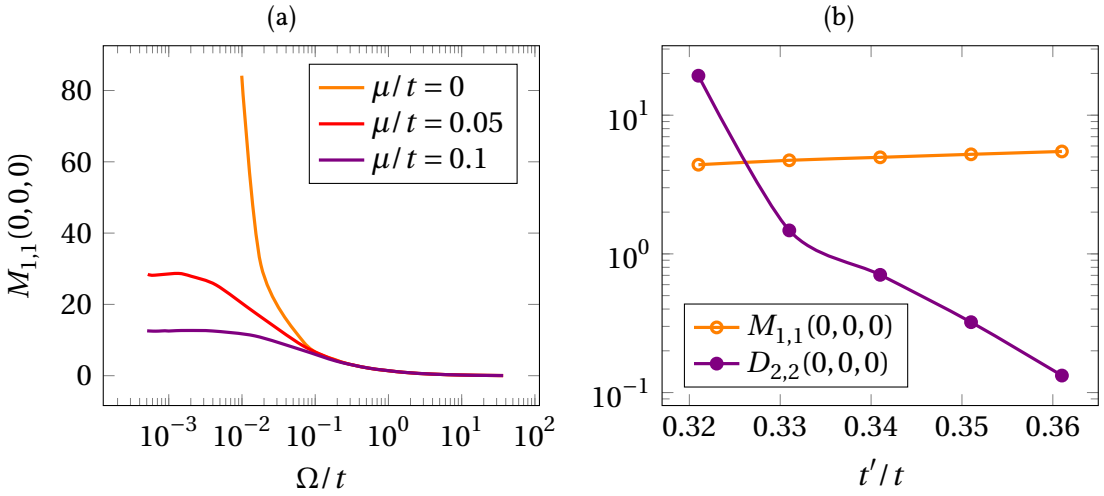

Figure 5.7: (a) The ferromagnetic coupling as a function of scale during the flow for $t'/t = 0.45$ and various values of $\mu > 0$. (b) The superconducting and ferromagnetic couplings for $\mu/t = 0.05$ and $\Omega/t = 10^{-3}$.

a symmetric pole structure, the sought regulating function has to be complex valued. As an alternative to the Ω-regulator (3.11) one might consider the regulator

$$\chi^{\mathrm{c}}_{\Omega}(\omega) = \frac{\omega}{\omega + \mathrm{i}\Omega}\,, \qquad \text{(3.14 revisited)}$$

which indeed has the benefit of being analytic in the upper-half complex plane. Even though the regulator is complex, the time reversal symmetry is preserved. This is the case whenever the action $S(\psi, \overline{\psi})$ is invariant under the involution $\#$,

$$S(\psi_k, \overline{\psi}_k)^{\#} = S(\psi_k, \overline{\psi}_k)\,,$$

defined by $\psi^{\#}_{\omega,\boldsymbol{k}} = \mathrm{i}\sigma_2\psi_{-\omega,-\boldsymbol{k}}, \overline{\psi}^{\#}_{\omega,\boldsymbol{k}} = \overline{\psi}_{-\omega,-\boldsymbol{k}}\mathrm{i}\sigma_2^t$ and by complex conjugation of scalars. Since the regulator satisfies

$$\chi^{\mathrm{c}}_{\Omega}(\omega) = \overline{\left(\chi^{\mathrm{c}}_{\Omega}(-\omega)\right)}\,,$$

the time reversal symmetry is preserved.

The Matsubara integral of the tadpole term (c.f. (3.12))

$$\oint_{\omega} \frac{\chi^{c}(\omega)}{\mathrm{i}\omega - \xi} = \frac{1}{2}\frac{\xi}{\xi - \Omega}\Theta(-\xi)$$

then vanishes in the limit $\Omega \to \infty$ as desired. While the analytic structure of this regulator seem beneficial here, the pole structure affects the bubble integrals in a possibly harmful way. The reason is that the particle-hole bubble will have only poles in $\mathbb{H}_+$ induced by the bare propagator while the particle-particle bubble will besides have a pole in $\mathbb{H}_-$ caused by the regulator. This asymmetry will, for example, break the Luttinger symmetry in one dimension.

In the case of the two dimensional Hubbard model, we learned from two-patch calculations that the position of the QCP is sensible to the balance between the particle-hole bubbles at momenta (π,π) and $(0,0)$. Figure 5.8.b shows the difference between relevant bubbles driving the phase transition. The zero contour is shifted to smaller hopping parameter compared to the case of the real Ω-regulator. Figure 5.8.a shows the stopping scale and instabilities computed using the regulating function χ^{c} compared to the results of Chapter 3 in gray. There is a significant difference between the position of the phase transitions in these two cases. As predicted by the difference in the relevant bubbles, the critical point now seams to be at a smaller hopping amplitude $t'/t \approx 0.25 < \theta^\star = 0.341$. It is not surprising that results obtained from flow equations depend on the regulator but it takes some more investigation to find out which scheme is better.

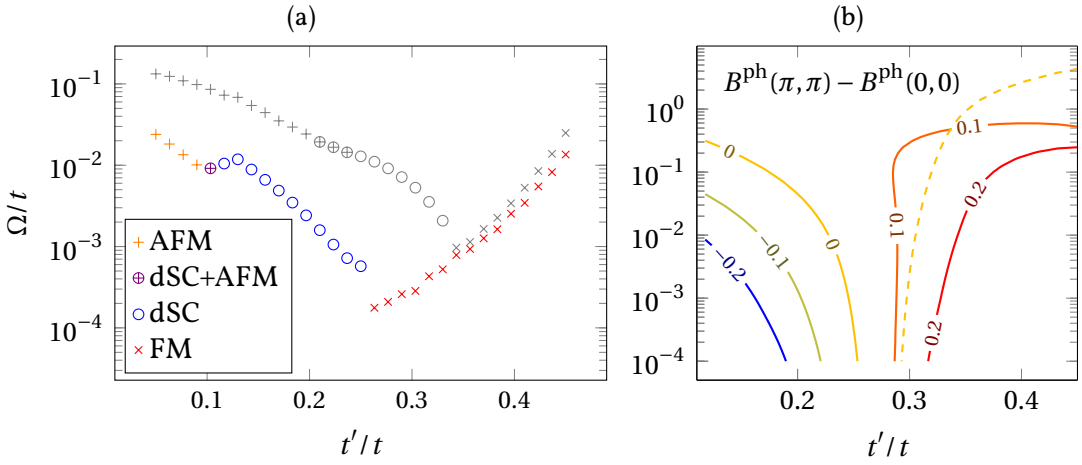

Figure 5.8: a) Stopping scale and instabilities of 2D-Hubbard model at vHF for $U/t = 3$ as a function of hopping parameter. Colorful marks correspond to the complex regulator (3.14) and gray ones to the Ω-regulator (3.11). b) The difference $B^{\mathrm{ph}}(\pi,\pi) - B^{\mathrm{ph}}(0,0)$ as a function of hopping parameter t'/t and scales Ω. The dashed curve is the zero contour in the Ω-scheme (c.f. Figure 2.6).

5.7 Conclusion and Outlook

Some of the most intriguing phenomena in physics happen in parameter ranges where theoretical models are the hardest to solve. Perturbation theory fails for there is no suitable small parameter to expand around. Mean-Field theories miss important quantum fluctuations and disappoint in low dimensions. And in the case of fermions, direct simulations like Monte-Carlo methods suffer from the sign problem. The sign problem is NP-hard and it is widely believed that there are no polynomial-time solutions to these problems. Thus, we need to progress in finding sophisticated approximations which reduce the complexity and take into account quantum fluctuations.

The functional renormalization group is a step in the right direction. We started by drawing a connection between the successful Katanin scheme and the Schwinger-Dyson equation to better understand why this scheme works so well. This led us to a new saddle-point formulation of the Schwinger-Dyson equations. Using the found variational functional, we are able to develop self-consistent approximations. We tested such a new approximation against the Katanin scheme and found out that if the derivative of the interaction vertex is large, one should suspect quantitative errors and threat results with reservation. The major drawback of the self-consistent equations is increased computational complexity. Whether or not the self-consistent equations are valid for bosonic and mixed system is still an open question which requires investigation. The saddle-point formalism can also be used to derive regulator independent flow equations, which should be investigated in the future. In all approximations known to me, it is rather difficult to find a bound on the error. In the case of the saddle-point or Schwinger-Dyson flow equations, we expressed the error in orders of the interaction vertex. But this does not provide any bound on the error by itself, especially not when the interaction is not small. The computational time grows so rapidly that including higher order terms and checking for a convergent result is not feasible. A generic and practical method of finding an upper bound for the errors is desirable.

The two-dimensional Hubbard model is of special interest for the following reasons. It is believed to be the key to understanding high-temperature superconductivity in cuprate. It is a simple but highly non-trivial example of a low dimensional fermionic system with a very rich phase diagram. A singular Fermi surfaces at van Hove filling demands special attention and usually invalidates calculations which don't count for it. The phase diagram

includes a quantum critical point which turns the Hubbard model into a prime example of a non-Fermi-liquid. Furthermore, it is possible to realize the Hubbard model on optical lattices experimentally. They main challenge is reaching lower temperatures. Eventually, we hope that it becomes possible to simulate the Hubbard model in tunable setup so we find a reliable basis for comparison.

Using static vertex approximation which allows for good numerical optimization we presented the instability diagram of the 2D-Hubbard model for a large range of filling and hopping amplitudes. In parameter regimes where we suspected self-energy effects to be important we made it a priority to check for them carefully, as detailed below. The instability forecasts a certain phase. The gaps can be computed using mean-field theory. We did this in the vicinity of the quantum critical point and showed that all relevant order parameter vanish there. Using a toy model we found out that the frequency dependence of the self-energy suppresses gap formation. The non-Fermi-liquid-like self-energy $\sim (-)\mathrm{sgn}(\omega)|\omega|^{\alpha}$ with the exponent $\alpha \approx 0.74$ is consistent with direct two-loop calculations. It deviates from the exponent $\alpha = 2/3$ found by Rech et al. but their assumption of a circular Fermi-surface does not apply to the singular Fermi-surface in our case. We also checked effects of the real part of the self-energy on the flow and found out that the deformation of the Fermi-surface is negligible up to very small scales. However, since we know that the curvature of the self-energy at van Hove points will diverge eventually, one must consider it for rigorous results and it may warrant further investigation.

With the exception of the incommensurate antiferromagnet the instabilities are rather insensible to the patching and the details of momentum dependences barely affect the result. In the case of the incommensurate antiferromagnet, based on the shape of the Fermi-surface, we have a good understanding of why the momentum dependence is important. In all other cases, the frequency dependences seem to be much more relevant to the ground state of the system. Therefore, we found it useful to include the frequency dependent interaction vertex in mean-field calculations. We found the general case to be much too difficult to solve and decided to begin with a minimal model. In this model we had a mono-frequency density-density interaction beside the static one. We found that such an interaction, which mimics the actual density-density interaction at the critical point, suppresses the quasiparticle lifetime. Exploring the minimal model we gained valuable information about the saddle points of the free-energy. The evaluation of the free-energy requires computing the

determinant of a matrix with as many rows and columns as they are non-zero contributions in the interaction. Then, one has to minimize this free-energy in equally as many fields. So mean-field calculations for a more realistic frequency dependent interaction require extensive work.

Appendix A

Appendix to Chapter 1 on Higher Order Flow Equations

We will discuss higher order SDRG flow equations briefly. Let us begin with the interaction vertex. The starting point is Equation (1.6) which leads to the flow equation

$$\begin{aligned}\dot{\Gamma}^{(4)} = \frac{\mathrm{d}}{\mathrm{d}\Omega}\mathbb{S}\Big\{&\frac{1}{2}\Gamma^{(4)}\circ\Pi_G\circ\Gamma^{(4)} - 2\Gamma^{(4)} * \Upsilon_G * \Gamma^{(4)} \\ &-\frac{1}{4}\Gamma^{(4)}\circ\Pi_G\circ\Gamma^{(4)}\circ\Pi_G\circ\Gamma^{(4)} - 2\Gamma^{(4)} * \Upsilon_G * \Gamma^{(4)} * \Upsilon_G * \Gamma^{(4)}\Big\} + \mathscr{O}\left(\Gamma^{(4)}\right)^5 .\end{aligned} \tag{A.1}$$

After taking the derivative we obtain terms involving $\dot{\Gamma}^{(4)}$ on the right-hand side. Of course we can iterate this equation to replace these terms with ones involving only the vertex, the propagator and its derivative. The right-hand-side of Equation (A.1) is a sum of ladder equation but the iteration mixes up different channels and yields to

$$\begin{aligned}\dot{\Gamma}_{x_1,x_2;x_3,x_4} = \mathbb{S}_{x_1,x_2;x_3,x_4}\Bigg(&\int_{z_1\cdots z_4}\Gamma_{x_1,x_2;z_1,z_2}\Gamma_{z_3,z_4;x_3,x_4}\dot{G}_{z_1,z_3}G_{z_2,z_4} \\ &-4\int_{z_1\cdots z_4}\Gamma_{z_1,x_1;x_3,z_2}\Gamma_{x_2,z_3;z_4,x_4}\dot{G}_{z_4,z_1}G_{z_2,z_3} \\ &+4\int_{z_1\cdots z_8}\Gamma_{z_1,x_1;x_3,z_2}\Gamma_{z_3,x_2;z_4,z_5}\Gamma_{z_6,z_7;z_8,x_4}G_{z_8,z_1}G_{z_2,z_3}G_{z_4,z_6}\dot{G}_{z_5,z_7} \\ &+8\int_{z_1\cdots z_8}\Gamma_{z_1,x_1;x_3,z_2}\Gamma_{z_3,x_2;z_4,z_5}\Gamma_{z_6,z_7;z_8,x_4}G_{z_4,z_1}G_{z_2,z_6}G_{z_8,z_3}\dot{G}_{z_5,z_7}\end{aligned}$$

(continued on next page)

$$
\begin{aligned}
&+8\int_{z_1\cdots z_8}\Gamma_{z_1,x_1;x_3,z_2}\Gamma_{z_3,x_2;z_4,z_5}\Gamma_{z_6,z_7;z_8,x_4}G_{z_4,z_1}G_{z_2,z_6}\dot{G}_{z_8,z_3}G_{z_5,z_7} \\
&+2\int_{z_1\cdots z_8}\Gamma_{x_1,z_1;z_2,z_3}\Gamma_{z_4,x_2;z_5,z_6}\Gamma_{z_7,z_8;x_3,x_4}\dot{G}_{z_6,z_1}G_{z_2,z_4}G_{z_3,z_8}G_{z_5,z_7} \\
&-4\int_{z_1\cdots z_8}\Gamma_{x_1,z_1;z_2,x_3}\Gamma_{x_2,z_3;z_4,x_4}\Gamma_{z_5,z_6;z_7,z_8}G_{z_7,z_1}\dot{G}_{z_2,z_5}G_{z_8,z_3}G_{z_4,z_6} \\
&-4\int_{z_1\cdots z_8}\Gamma_{x_1,z_1;z_2,x_3}\Gamma_{x_2,z_3;z_4,x_4}\Gamma_{z_5,z_6;z_7,z_8}\dot{G}_{z_7,z_1}G_{z_2,z_5}G_{z_8,z_3}G_{z_4,z_6} \\
&+2\int_{z_1\cdots z_8}\Gamma_{x_2,x_1;z_1,z_2}\Gamma_{z_3,z_4;x_3,z_5}\Gamma_{z_6,z_7;z_8,x_4}G_{z_1,z_4}G_{z_2,z_6}G_{z_8,z_3}\dot{G}_{z_5,z_7}\Big).
\end{aligned}
\tag{A.2}
$$

Provided that the interaction vertex satisfies (A.2), the self-consistent equation for the self-energy at second and higher orders in $\Gamma^{(4)}$ coincide with the exact equation

$$\dot{\Sigma} = -G[\![v]\!] - \frac{1}{2}G[\![v\circ\Pi_G\circ\Gamma^{(4)}]\!]\,.$$

The associated flow equation is

$$\dot{\Sigma} = -\dot{G}[\![v]\!] - \frac{1}{2}\dot{G}[\![v\circ\Pi_G\circ\Gamma^{(4)}]\!] - \frac{1}{2}G[\![v\circ\dot{\Pi}_G\circ\Gamma^{(4)}]\!] - \frac{1}{2}G[\![v\circ\Pi_G\circ\dot{\Gamma}^{(4)}]\!]\,.$$

It is important to consider that the flow equation of the vertex depends on the derivative of the self-energy and the self-energy derivative itself on the derivative of the vertex. So we end up with an implicit ODE. Since (1.14) already contains two-loop contributions (see Section 5.1) one may combine it with (A.2) to obtain explicit two-loop flow equations.

Appendix B

Appendix to Chapter 2 on the Precise Definition of the Couplings

Since our model exhibits SU(2) spin rotation invariance, we can express the four-point irreducible vertex as

$$\begin{aligned}\Gamma^{(4)}(p_1\sigma_1, p_3\sigma_2; p_3\sigma_3, p_4\sigma_4) = &v(p_1, p_3; p_3, p_4)\delta_{\sigma_1,\sigma_4}\delta_{\sigma_2,\sigma_3} \\ &- v(p_1, p_3; p_3, p_4)\delta_{\sigma_1,\sigma_3}\delta_{\sigma_2,\sigma_4}\,,\end{aligned} \tag{B.1}$$

where v is independent of spin indices and symmetric under simultaneous permutation of its first two and last two arguments [77]. We label the van Hove points by $\boldsymbol{a} = (0, \pi)$ and $\boldsymbol{b} = (\pi, 0)$ and define a projection

$$\mathbb{P} : (-\pi, \pi]^2 \to \{\boldsymbol{a}, \boldsymbol{b}\} \quad , \quad (x, y) \mapsto \boldsymbol{a} \quad \text{if} \quad |y| \geq |x| \quad \text{and} \quad \boldsymbol{b} \quad \text{otherwise} \quad ,$$

from the Brillouin zone to either $\boldsymbol{a}$ or $\boldsymbol{b}$. The symmetric vertex v of the two-patch model is then given by

$$v(p_1, p_3; p_3, p_4) = u(\mathbb{P}p_1, \mathbb{P}p_2; \mathbb{P}p_3, \mathbb{P}p_4)\,,$$

where the four couplings $g_1, \ldots, g_4$ are

$$\begin{aligned} g_1 &= u(\boldsymbol{a}, \boldsymbol{b}; \boldsymbol{b}, \boldsymbol{a}) = u(\boldsymbol{b}, \boldsymbol{a}; \boldsymbol{a}, \boldsymbol{b})\,, \\ g_2 &= u(\boldsymbol{a}, \boldsymbol{b}; \boldsymbol{a}, \boldsymbol{b}) = u(\boldsymbol{b}, \boldsymbol{a}; \boldsymbol{b}, \boldsymbol{a})\,, \\ g_3 &= u(\boldsymbol{a}, \boldsymbol{a}; \boldsymbol{b}, \boldsymbol{b}) = u(\boldsymbol{b}, \boldsymbol{b}; \boldsymbol{a}, \boldsymbol{a})\,, \\ g_4 &= u(\boldsymbol{a}, \boldsymbol{a}; \boldsymbol{a}, \boldsymbol{a}) = u(\boldsymbol{b}, \boldsymbol{b}; \boldsymbol{b}, \boldsymbol{b})\,. \end{aligned}$$

Due to momentum conservation other combinations of the projected momenta are irrelevant.

The self-consistent and RG equations for the couplings $g_1, \dots, g_4$ follow by inserting $\Gamma^{(4)}$ from Eq. (B.1) into the appropriate equation and splitting the momentum integral of bubbles according to

$$\int_{\omega,\boldsymbol{p}} C(\omega,\boldsymbol{p})C(\pm\omega,\pm\boldsymbol{p}) = \left(\int_{\substack{\omega,\boldsymbol{p}\\ \mathbb{P}(\boldsymbol{p})=\boldsymbol{a}}} + \int_{\substack{\omega,\boldsymbol{p}\\ \mathbb{P}(\boldsymbol{p})=\boldsymbol{b}}}\right)\big(C(\omega,\boldsymbol{p})C(\pm\omega,\pm\boldsymbol{p})\big)\,,$$
$$\int_{\omega,\boldsymbol{p}} C(\omega,\boldsymbol{p})C(\pm\omega,\pm(\boldsymbol{p}-\hat{\pi})) = \left(\int_{\substack{\omega,\boldsymbol{p}\\ \mathbb{P}(\boldsymbol{p})=\boldsymbol{a}}} + \int_{\substack{\omega,\boldsymbol{p}\\ \mathbb{P}(\boldsymbol{p})=\boldsymbol{b}}}\right)\big(C(\omega,\boldsymbol{p})C(\pm\omega,\pm(\boldsymbol{p}-\hat{\pi}))\big)\,,$$

where $\hat{\pi} = (\pi,\pi)$. For all $\boldsymbol{p}$,

$$\mathbb{P}(\boldsymbol{p}) = \boldsymbol{a} \implies \mathbb{P}(-\boldsymbol{p}) = \boldsymbol{a} \quad \text{and} \quad \mathbb{P}(\pm(\boldsymbol{p}-\hat{\pi})) = \boldsymbol{b}$$
$$\mathbb{P}(\boldsymbol{p}) = \boldsymbol{b} \implies \mathbb{P}(-\boldsymbol{p}) = \boldsymbol{b} \quad \text{and} \quad \mathbb{P}(\pm(\boldsymbol{p}-\hat{\pi})) = \boldsymbol{a}\,.$$

Furthermore due to symmetry for $\boldsymbol{k} \in \{(0,0),(\pi,\pi)\}$,

$$\int\limits_{\substack{\omega,\boldsymbol{p}\\ \mathbb{P}(\boldsymbol{p})=\boldsymbol{a}}} C(\omega,\boldsymbol{p})C(\pm\omega,\pm(\boldsymbol{p}-\boldsymbol{k})) = \int\limits_{\substack{\omega,\boldsymbol{p}\\ \mathbb{P}(\boldsymbol{p})=\boldsymbol{b}}} C(\omega,\boldsymbol{p})C(\pm\omega,\pm(\boldsymbol{p}-\boldsymbol{k})) = \pm\frac{1}{2}\Pi^{\mathrm{ph/pp}}(\boldsymbol{k})\,.$$

The latter equation explains the factors $1/2$ in Eq. (2.3).

Appendix C

Appendix to Chapter 3 on Numerical Implementation and Optimization

Here we will discuss the numerical implementation and optimization of the programs used to solve the flow equations. After parametrization we have a system of coupled differential equations of the form

$$\dot{v}_i(\Omega) = f_i(\boldsymbol{v}(\Omega)) \,,$$

to solve. The variables v_i are the self-energy and exchange propagators at representative frequency and momenta. The most time consuming parts are the bubble integrals on the right-hand side of the flow equations. Benchmarking a native implementation we found that generic integration routines become slow at small scales as the integrands develop very sharp structures around the Fermi-surface. Furthermore most of the processing time is spent in the portion of code computing the dispersion relation due to the trigonometric functions. To speed up the evaluation we replaced each bubble integral with a weighted sum over a set of points which take into account the momentum structure of that specific bubble. We generate the quadrature rule based on the *double exponential* method introduced by Takahasi and Mori [78]. This quadrature rule is known to be efficient and to handle singularities very well. Figure C.1 shows an example of how the quadrature rule adjusts to the most singular structure of a bubble. Since in our setup every integrand on the right-hand side of the flow equations in evaluated at a fixed set of momenta (specific to every integral), we can compute the dispersion relation at this points once and store the result in memory. So we overcome both causes of slow-downs.

In the next optimization step we replace the single instruction streams with vector instructions. Assume we want to integrate the function $f : (x, y) \mapsto \mathbb{R}$ over the Brillouin zone $[-\pi, \pi)^2$ and let the vectors $\boldsymbol{x}$ and $\boldsymbol{y}$ contain the positions in our quadrature rule and the vector $\boldsymbol{w}$ the associated weights. Schematically the weighted sum of a function

$s \leftarrow 0$
for $i = 1$ **to** n **do**
  $s \leftarrow s + w_i f(x_i, y_i)$
end

is replaced by

$s \leftarrow \tilde{f}(\boldsymbol{x}, \boldsymbol{y}) \cdot \boldsymbol{w}$

where $\tilde{f}$ operates on the vectors $\boldsymbol{x}$ and $\boldsymbol{y}$. When this is done correctly the program can benefit both from cache coherence and modern SIMD (single instruction, multiple data) instructions.

The method described above works as long as we neglect the real-part of the self-energy, i.e. as long as the Fermi-surface is fixed. Frequency dependent interaction vertex and the imaginary-part of the self-energy can be included without any problems. The frequency dependence increases the number of parameters and hence the number of differential equations by an order of magnitude. The zero temperature Matsubara integrals are then evaluated using the double exponential method accurately. A single integral requires between 50 and 200 evaluations to achieve an accuracy of about 1%.

The inclusion of the real part of the self-energy deforms the Fermi-surface and requires other methods. We have developed an integration routine which keeps track of the singular structure of the integrands. The method is slow and only accurate up to about $\Omega / t = 10^{-4}$.

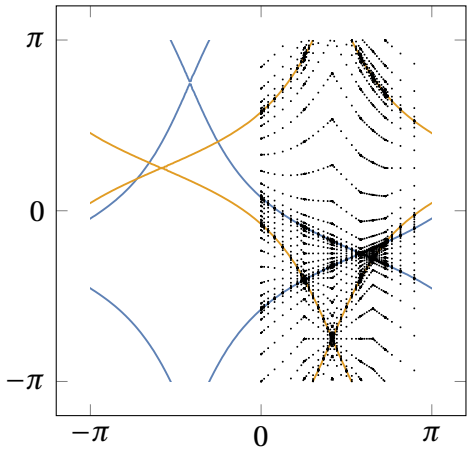

Figure C.1: Example of a quadrature rule for a bubble with total momenta transfer $(\frac{5}{6}\pi, \frac{3}{6}\pi)$. The integrand is evaluated on the black points and the integral is computed as a weighted sum of the results. Due to symmetry the integration can be restricted to half of the Brillouin zone. Colored curves show the position of the Fermi-surfaces.

Appendix D

Appendix to Chapter 4 on Two-Loop Estimations of the Second Derivative of the Self-Energy

Here we review few details concerning the evaluation of $\left(\partial_x^2\Sigma\right)(\frac{\pi}{\beta},\pi,0)$ plotted in figure 5.5. The derivative is taken with respect to the second argument, i.e. the first component of the momentum. The two-loop contribution to the self-energy is given by

$$\Sigma^{(2)}(k) = -U^2\frac{1}{2}\int_q c(k-q)P(q)\,,$$

where

$$P(q) = \frac{1}{\beta}\int_p c(p)c(p-\boldsymbol{q})$$

and $c(\boldsymbol{p}) = (\mathrm{i}\,p_0 - \xi_{\boldsymbol{p}})^{-1}$ is the bare propagator. We are interested in the second derivative of the self-energy as a function of inverse temperature and there is no regulating function involved. The Matsubara sums can be performed analytically and one obtains

$$\begin{aligned}\Sigma^{(2)}(k) =& U^2\int_{\boldsymbol{p},\boldsymbol{q}} S(\boldsymbol{p},\boldsymbol{q})\,,\\ S(k;\boldsymbol{p},\boldsymbol{q}) =& \frac{f(\xi_{\boldsymbol{p}})f(-\xi_{\boldsymbol{p}-\boldsymbol{q}})f(\xi_{\boldsymbol{k}-\boldsymbol{q}}) + f(-\xi_{\boldsymbol{p}})f(\xi_{\boldsymbol{p}-\boldsymbol{q}})f(-\xi_{\boldsymbol{k}-\boldsymbol{q}})}{\mathrm{i}\,k_0 - \xi_{\boldsymbol{k}-\boldsymbol{q}} - \xi_{\boldsymbol{p}} + \xi_{\boldsymbol{p}-\boldsymbol{q}}}\,,\end{aligned}$$

where f is the Fermi function

$$f(x) = \frac{1}{1+\mathrm{e}^{\beta x}}\,.$$

The remaining integrals are very tough to evaluate accurately at low temperatures. In order to estimate the second derivatives we first exchange the order of integration and differentiation, then we restrict the integration to small regions where the integrand is the largest and obtain

$$\frac{1}{U^2}\left(\partial_x^2\Sigma^{(2)}\right)\left(\tfrac{\pi}{\beta},\pi,0\right) \sim \left(\int\limits_{\substack{\boldsymbol{p}\in D_a(0,\pi)\\ \boldsymbol{q}\in D_a(0,0)}} + \int\limits_{\substack{\boldsymbol{p}\in D_a(0,\pi)\\ \boldsymbol{q}\in D_a(\pi,\pi)}} + \int\limits_{\substack{\boldsymbol{p}\in D_a(\pi,0)\\ \boldsymbol{q}\in D_a(0,0)}} + \int\limits_{\substack{\boldsymbol{p}\in D_a(\pi,0)\\ \boldsymbol{q}\in D_a(\pi,\pi)}}\right)\left(\partial_x^2 S(\tfrac{\pi}{\beta},\pi,0;\boldsymbol{p},\boldsymbol{q})\right), \tag{D.1}$$

where

$$D_a(u,v) = \left\{(x,y) : |x-u| < \tfrac{a}{2} \wedge |y-v| < \tfrac{a}{2}\right\}$$

and $a > 0$ is a constant. Depending on β, a has to be chosen large enough to capture the main structures of the integrand but small enough to allow a reliable numerical evaluation of the integrals. In order to get an estimate for a large range of inverse temperature we compute (D.1) for several values of a in different regimes of β and glue the results together. Figure D.1 shows estimates with different values of a. By shifting the curves so that the last point of a curve corresponding to a larger a matches the first one corresponding to the next smaller a we can glue the curves together. Shifting the curves is based on the assumption that the regions we do not integrate over, approximately contribute a temperature independent constant to the result. The final result is then what is shown in Figure 5.5. Estimates for $t\beta > 10^6$ are unreliable due to limits imposed by floating point precision.

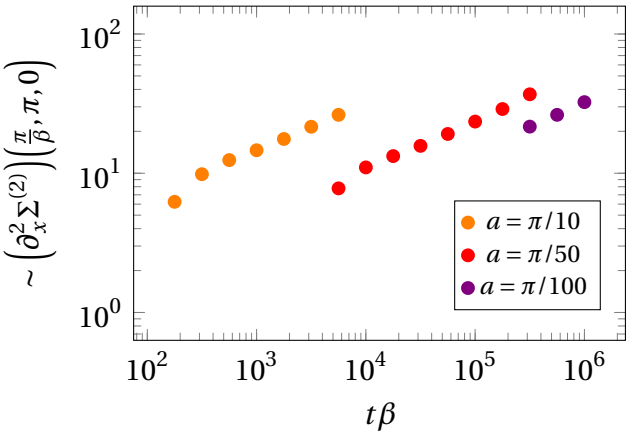

Figure D.1: Estimates of the second derivative of self-energy according to (D.1). With a smaller a we can estimate the integral better for larger inverse temperatures. Combining the results leads to Figure 5.5.

Appendix E

Lists of Abbreviations

1PI ..... One-Particle Irreducible
IR ..... Infrared
UV ..... Ultraviolet
RG ..... Renormalization Group
fRG ..... functional Renormalization Group
vHP ..... van Hove Point(s)
vHS ..... van Hove Singularity (Singularities)
LW ..... Luttinger-Ward
SD ..... Schwinger-Dyson
SDE ..... Schwinger-Dyson Equation(s)
SDRG ..... Schwinger-Dyson Renormalization Group
HS ..... Hubbard Stratonovich
AFM ..... Antiferromagnet(ic)
FM ..... Ferromagnet(ic)
SC ..... Superconductor (Superconducting)
dSC ..... d-Wave Superconductor (Superconducting)
QCP ..... Quantum Critical Point
NFL ..... Non-Fermi-Liquid
NFLL ..... Non-Fermi-Liquid-Like

References

[1] Martin C. Gutzwiller. "Effect of Correlation on the Ferromagnetism of Transition Metals". In: *Phys. Rev. Lett.* 10 (5 Mar. 1963), pp. 159–162. DOI: 10.1103/PhysRevLett.10.159.

[2] J. Hubbard. "Electron Correlations in Narrow Energy Bands". In: *Proceedings of the Royal Society of London Series A* 276.1365 (Nov. 26, 1963), pp. 238–257.

[3] Elliott H. Lieb and F. Y. Wu. "Absence of Mott Transition in an Exact Solution of the Short-Range, One-Band Model in One Dimension". In: *Phys. Rev. Lett.* 20 (25 June 1968), pp. 1445–1448. DOI: 10.1103/PhysRevLett.20.1445.

[4] Ovchinnikov A. A. "Excitation Spectrum in the One-dimensional Hubbard Model". In: *JETP* 30 (6 June 1970), p. 1160.

[5] H. Shiba. "Magnetic Susceptibility at Zero Temperature for the One-Dimensional Hubbard Model". In: *Phys. Rev. B* 6 (3 Aug. 1972), pp. 930–938. DOI: 10.1103/PhysRevB.6.930.

[6] Minoru Takahashi. "Low-Temperature Specific-Heat of One-Dimensional Hubbard Model". In: *Progress of Theoretical Physics* 52.1 (1974), pp. 103–114. DOI: 10.1143/PTP.52.103.

[7] Walter Metzner and Dieter Vollhardt. "Correlated Lattice Fermions in $d = \infty$ Dimensions". In: *Phys. Rev. Lett.* 62 (3 Jan. 1989), pp. 324–327. DOI: 10.1103/PhysRevLett.62.324.

[8] W.D. Langer and D.C. Mattis. "Ground state energy of Hubbard model". In: *Physics Letters A* 36.2 (1971), pp. 139–140. ISSN: 0375-9601. DOI: 10.1016/0375-9601(71)90784-5.

[9] Kenn Kubo and Tatsuya Kishi. "Rigorous bounds on the susceptibilities of the Hubbard model". In: *Phys. Rev. B* 41 (7 Mar. 1990), pp. 4866–4868. DOI: 10.1103/PhysRevB.41.4866.

[10] Elliott H. Lieb. "Two theorems on the Hubbard model". In: *Phys. Rev. Lett.* 62 (10 Mar. 1989), pp. 1201–1204. DOI: 10.1103/PhysRevLett.62.1201.

[11] Martin C. Gutzwiller. "Correlation of Electrons in a Narrow *s* Band". In: *Phys. Rev.* 137 (6A Mar. 1965), A1726–A1735. DOI: 10.1103/PhysRev.137.A1726.

[12] Gabriel Kotliar and Andrei E. Ruckenstein. "New Functional Integral Approach to Strongly Correlated Fermi Systems: The Gutzwiller Approximation as a Saddle Point". In: *Phys. Rev. Lett.* 57 (11 Sept. 1986), pp. 1362–1365. DOI: 10.1103/PhysRevLett.57.1362.

[13] N. E. Bickers, D. J. Scalapino, and S. R. White. "Conserving Approximations for Strongly Correlated Electron Systems: Bethe-Salpeter Equation and Dynamics for the Two-Dimensional Hubbard Model". In: *Phys. Rev. Lett.* 62 (8 Feb. 1989), pp. 961–964. DOI: 10.1103/PhysRevLett.62.961.

[14] Edwin Langmann and Mats Wallin. "Mean Field Magnetic Phase Diagrams for the Two Dimensional t - t' - U Hubbard Model". In: *Journal of Statistical Physics* 127.4 (2007), pp. 825–840. ISSN: 1572-9613. DOI: 10.1007/s10955-007-9308-y.

[15] A. Montorsi. *The Hubbard Model: A Collection of Reprints*. 1992. ISBN: 978-9-81-450635-9.

[16] J. G. Bednorz and K. A. Müller. "Possible highTc superconductivity in the Ba–La–Cu–O system". In: *Zeitschrift für Physik B Condensed Matter* 64.2 (1986), pp. 189–193. ISSN: 1431-584X. DOI: 10.1007/BF01303701.

[17] P. W. ANDERSON. "The Resonating Valence Bond State in La2CuO4 and Superconductivity". In: *Science* 235.4793 (1987), pp. 1196–1198. ISSN: 0036-8075. DOI: 10.1126/science.235.4793.1196.

[18] F. C. Zhang and T. M. Rice. "Effective Hamiltonian for the superconducting Cu oxides". In: *Phys. Rev. B* 37 (7 Mar. 1988), pp. 3759–3761. DOI: 10.1103/PhysRevB.37.3759.

[19] D. N. Basov and Andrey V. Chubukov. "Manifesto for a higher Tc". In: *Nature Physics* 7.4 (Apr. 2011), pp. 272–276. ISSN: 1745-2473. DOI: 10.1038/nphys1975.

[20] Joseph Polchinski. "Renormalization and Effective Lagrangians". In: *Nucl. Phys.* B231 (1984), pp. 269–295. DOI: 10.1016/0550-3213(84)90287-6.

[21] D. C. Brydges and J. D. Wright. "Mayer expansions and the Hamilton-Jacobi equation. II. Fermions, dimensional reduction formulas". In: *Journal of Statistical Physics* 51.3 (1988), pp. 435–456. ISSN: 1572-9613. DOI: 10.1007/BF01028465.

[22] Manfred Salmhofer. “Continuous Renormalization for Fermions and Fermi Liquid Theory”. In: *Communications in Mathematical Physics* 194.2 (1998), pp. 249–295. ISSN: 1432-0916. DOI: 10.1007/s002200050358.

[23] Christof Wetterich. “Exact evolution equation for the effective potential”. In: *Physics Letters B* 301.1 (1993), pp. 90–94. ISSN: 0370-2693. DOI: 10.1016/0370-2693(93)90726-X.

[24] M. Salmhofer and C. Honerkamp. “Fermionic Renormalization Group Flows”. In: *Prog. Theor. Phys.* 105.1 (2001), pp. 1–35. DOI: 10.1143/PTP.105.1.

[25] Franz Wegner. “Flow-equations for Hamiltonians”. In: *Annalen der Physik* 506.2 (1994), pp. 77–91. ISSN: 1521-3889. DOI: 10.1002/andp.19945060203.

[26] Jürgen Berges, Nikolaos Tetradis, and Christof Wetterich. “Non-perturbative renormalization flow in quantum field theory and statistical physics”. In: *Physics Reports* 363.4–6 (2002). Renormalization group theory in the new millennium. {IV}, pp. 223–386. ISSN: 0370-1573. DOI: 10.1016/S0370-1573(01)00098-9.

[27] Walter Metzner et al. “Functional renormalization group approach to correlated fermion systems”. In: *Rev. Mod. Phys.* 84 (1 Mar. 2012), pp. 299–352. DOI: 10.1103/RevModPhys.84.299.

[28] A. A. Katanin. “Fulfillment of Ward identities in the functional renormalization group approach”. In: *Phys. Rev. B* 70 (11 Sept. 2004), p. 115109. DOI: 10.1103/PhysRevB.70.115109.

[29] Manfred Salmhofer et al. “Renormalization Group Flows into Phases with Broken Symmetry”. In: *Progress of Theoretical Physics* 112.6 (2004), pp. 943–970. DOI: 10.1143/PTP.112.943.

[30] S. Floerchinger and C. Wetterich. “Exact flow equation for composite operators”. In: *Physics Letters B* 680.4 (2009), pp. 371–376. ISSN: 0370-2693. DOI: 10.1016/j.physletb.2009.09.014.

[31] Jing Wang, Andreas Eberlein, and Walter Metzner. “Competing order in correlated electron systems made simple: Consistent fusion of functional renormalization and mean-field theory”. In: *Phys. Rev. B* 89 (12 Mar. 2014), p. 121116. DOI: 10.1103/PhysRevB.89.121116.

[32] H. J. Schulz. “Superconductivity and Antiferromagnetism in the Two-Dimensional Hubbard Model: Scaling Theory”. In: *EPL (Europhysics Letters)* 4.5 (1987), p. 609.

[33] I. E. Dzyaloshinskii. "Maximal increase of the superconducting transition temperature due to the presence of van't Hoff singularities". In: *Sov. Phys. JETP* 66 (1987), pp. 848–854.

[34] P. Lederer, .G Montambaux, and D. Poilblanc. "Antiferromagnetism and superconductivity in a quasi two-dimensional electron gas. Scaling theory of a generic Hubbard model". In: *J. Phys. France* 48 (1987), pp. 1613–1618.

[35] I. E. Dzyaloshinskii. "Extended Van-Hove Singularity and Related Non-Fermi Liquids". In: *J. Phys. I France* 6 (1996), pp. 119–135.

[36] N Furukawa et al. "Renormalization group study of the Hubbard model at the van Hove singular point". In: *Physica B: Condensed Matter* 284–288, Part 2 (2000), pp. 1571–1572. ISSN: 0921-4526. DOI: 10.1016/S0921-4526(99)02824-0.

[37] Nobuo Furukawa, T. M. Rice, and Manfred Salmhofer. "Truncation of a Two-Dimensional Fermi Surface due to Quasiparticle Gap Formation at the Saddle Points". In: *Phys. Rev. Lett.* 81 (15 Oct. 1998), pp. 3195–3198. DOI: 10.1103/PhysRevLett.81.3195.

[38] A. P. Kampf and A. A. Katanin. "Competing phases in the extended $U - V - J$ Hubbard model near the Van Hove fillings". In: *Phys. Rev. B* 67 (12 Mar. 2003), p. 125104. DOI: 10.1103/PhysRevB.67.125104.

[39] D. Zanchi and H. J. Schulz. "Weakly correlated electrons on a square lattice: A renormalization group theory". In: *EPL (Europhysics Letters)* 44.2 (1998), p. 235.

[40] Christoph J. Halboth and Walter Metzner. "Renormalization-group analysis of the two-dimensional Hubbard model". In: *Phys. Rev. B* 61 (11 Mar. 2000), pp. 7364–7377. DOI: 10.1103/PhysRevB.61.7364.

[41] C. Honerkamp et al. "Breakdown of the Landau-Fermi liquid in two dimensions due to umklapp scattering". In: *Phys. Rev. B* 63 (3 Jan. 2001), p. 035109. DOI: 10.1103/PhysRevB.63.035109.

[42] Carsten Honerkamp and Manfred Salmhofer. "Temperature-flow renormalization group and the competition between superconductivity and ferromagnetism". In: *Phys. Rev. B* 64 (18 Oct. 2001), p. 184516. DOI: 10.1103/PhysRevB.64.184516.

[43] Joel Feldman, Manfred Salmhofer, and Eugene Trubowitz. "Regularity of the moving Fermi surface: RPA contributions". In: *Communications on Pure and Applied Mathematics* 51.9-10 (1998), pp. 1133–1246. ISSN: 1097-0312.

[44] Sascha Ledowski and Peter Kopietz. "An exact integral equation for the renormalized Fermi surface". In: *Journal of Physics: Condensed Matter* 15.27 (2003), p. 4779.

[45] C. Husemann, K.-U. Giering, and M. Salmhofer. "Frequency-dependent vertex functions of the (t, t') Hubbard model at weak coupling". In: *Phys. Rev. B* 85 (7 Feb. 2012), p. 075121. DOI: 10.1103/PhysRevB.85.075121.

[46] D. Zanchi. "Angle-resolved loss of Landau quasiparticles in 2D Hubbard model". In: *EPL (Europhysics Letters)* 55.3 (2001), p. 376.

[47] Carsten Honerkamp and Manfred Salmhofer. "Flow of the quasiparticle weight in the N -patch renormalization group scheme". In: *Phys. Rev. B* 67 (17 May 2003), p. 174504. DOI: 10.1103/PhysRevB.67.174504.

[48] Kay-Uwe Giering and Manfred Salmhofer. "Self-energy flows in the two-dimensional repulsive Hubbard model". In: *Phys. Rev. B* 86 (24 Dec. 2012), p. 245122. DOI: 10.1103/PhysRevB.86.245122.

[49] Kay-Uwe Giering. "Self-energy flows and the frequency-dependent interaction vertex in the two-dimensional repulsive Hubbard model". eng. PhD thesis. Heidelberg, Univ., Diss., 2012, 2012, Online–Ressource (VI, 141 S.)

[50] Kambis Veschgini and Manfred Salmhofer. "Schwinger-Dyson renormalization group". In: *Phys. Rev. B* 88 (15 Oct. 2013), p. 155131. DOI: 10.1103/PhysRevB.88.155131.

[51] F. Dyson. "The S Matrix in Quantum Electrodynamics". In: *Phys. Rev.* 75 (1949), p. 1736.

[52] J. Schwinger. "On Green's functions of quantized fields I + II". In: *Proc. Nat. Acad. Sci.* 37 (1951), pp. 452–459.

[53] J. Berges, N. Tetradis, and C. Wetterich. In: *Phys. Rep.* 363 (2002), p. 223.

[54] G. Keller and C. Kopper. "Perturbative renormalization of QED via flow equations". In: *Phys. Lett. B* 273 (1991), pp. 323–332.

[55] G. Keller and C. Kopper. "Renormalizability proof for QED based on flow equations". In: *Comm. Math. Phys.* 176 (1996), pp. 193–226.

[56] Gordon Baym and Leo P. Kadanoff. "Conservation Laws and Correlation Functions". In: *Phys. Rev.* 124 (2 Oct. 1961), pp. 287–299. DOI: 10.1103/PhysRev.124.287.

[57] Gordon Baym. "Self-Consistent Approximations in Many-Body Systems". In: *Phys. Rev.* 127 (4 Aug. 1962), pp. 1391–1401. DOI: 10.1103/PhysRev.127.1391.

[58] J.M. Cornwall, R. Jackiw, and E. Tomboulis. "Effective action for composite operators". In: *Phys. Rev. D* 10 (1974), pp. 2428–2445.

[59] M. Potthoff. "Diagram technique for nonequilibrium processes". In: *Adv. Solid State Phys.* 45 (2005), pp. 135–147.

[60] M. Potthoff. "Diagram technique for nonequilibrium processes". In: *Springer Series in Solid-State Sciences* 171 (2012), pp. 303–339.

[61] D. C. Brydges and T. Kennedy. "Mayer expansions and the Hamilton-Jacobi equation". In: *J. Stat. Phys.* 48 (1987), p. 19.

[62] M. Hindgren. PhD thesis. Lund University, 1997.

[63] Nils Erik Dahlen and Ulf von Barth. "Variational energy functionals tested on atoms". In: *Phys. Rev. B* 69 (19 May 2004), p. 195102. DOI: 10.1103/PhysRevB.69.195102.

[64] M. Salmhofer. "Continuous Renormalization for Fermions and Fermi Liquid Theory". In: *Commun. Math. Phys.* 194 (1998), pp. 249–295.

[65] M. Salmhofer. *Renormalization*. Springer, 1998.

[66] C. Honerkamp and M. Salmhofer. "Temperature-flow renormalization group and the competition between superconductivity and ferromagnetism". In: *Phys. Rev. B* 64.18 (Nov. 2001), pp. 184516–+. DOI: 10.1103/PhysRevB.64.184516.

[67] C. Husemann and M. Salmhofer. "Efficient parametrization of the vertex function, Ω scheme, and the (t, t') Hubbard model at van Hove filling". In: *Phys. Rev. B* 79.19 (May 2009), pp. 195125–+. DOI: 10.1103/PhysRevB.79.195125.

[68] Manfred Salmhofer and Carsten Honerkamp. "Fermionic Renormalization Group Flows: Technique and Theory". In: *Prog. Theor. Phys.* 105 (1 2001), pp. 1–35.

[69] Joel Feldman and Manfred Salmhofer. "Singular Fermi Surfaces II: The Two-Dimensional Case". In: *Reviews in Mathematical Physics* 20.03 (2008), pp. 275–334. DOI: 10.1142/S0129055X08003304.

[70] Joel Feldman and Manfred Salmhofer. "Singular Fermi Surfaces I: General Power Counting and Higher Dimensional Cases". In: *Reviews in Mathematical Physics* 20.03 (2008), pp. 233–274. DOI: 10.1142/S0129055X08003274.

[71] Carsten Honerkamp and Manfred Salmhofer. "Ferromagnetism and triplet superconductivity in the two-dimensional Hubbard model". In: *Physica C: Superconductivity* 408–410 (2004). Proceedings of the International Conference on Materials and Mechanisms of Superconductivity. High Temperature Superconductors VII – M2S-RIO, pp. 302–304. ISSN: 0921-4534. DOI: 10.1016/j.physc.2004.02.089.

[72] J. E. Hirsch. "Two-dimensional Hubbard model: Numerical simulation study". In: *Phys. Rev. B* 31 (7 Apr. 1985), pp. 4403–4419. DOI: 10.1103/PhysRevB.31.4403.

[73] D. Lehmann. *Mathematical Methods of Many-Body Quantum Field Theory*. Chapman & Hall/CRC Research Notes in Mathematics Series. Taylor & Francis, 2004. ISBN: 9781420035018.

[74] A. Schütte. "The Symmetry of the Gap in the BCS Model for Higher l-Wave Interactions". Diploma thesis. ETH Zürich, 1997.

[75] Volker Bach, Elliott H. Lieb, and Jan Philip Solovej. "Generalized Hartree-Fock theory and the Hubbard model". In: *Journal of Statistical Physics* 76.1 (July 1994), pp. 3–89. ISSN: 1572-9613. DOI: 10.1007/BF02188656.

[76] Folkmar Bornemann. "On the numerical evaluation of Fredholm determinants." In: *Math. Comput.* 79.270 (2010), pp. 871–915.

[77] P. Kopietz, L. Bartosch, and F. Schütz. *Introduction to the Functional Renormalization Group*. Lecture Notes in Physics. Springer, 2010. ISBN: 9783642050930.

[78] Hidetosi Takahasi and Masatake Mori. "Double Exponential Formulas for Numerical Integration." In: *Publ. Res. Inst. Math. Sci.* 9.3 (1973), pp. 721–741. DOI: 10.2977/prims/1195192451.

My time in Heidelberg has profoundly shaped me intellectually, socially and emotionally. I am most grateful for the friendship and support of many people without whom I would not be here today.

My greatest debt is to my doctoral supervisor and teacher, Professor Manfred Salmhofer. He challenged me with fascinating topics, while providing his deep insights and consistent advice throughout all stages of my dissertation.

Philosophenweg 19 has been my academic home during my graduate studies. I sincerely thank my friends and colleagues Giulio Schober, Kay Giering and Long Lu for inspiring discussions and memorable times, and David Breyel and Frank Hantschel for countless entertaining and motivating coffee breaks. I thank Lauren Andalora for proofreading my thesis.

I am grateful to Alice for her friendship and constant encouragement over many years. I thank Lara for sharing many adventures with me, and I am grateful to Lera for the amazing moments during this phase.

I cannot thank my parents and sister enough for their trust and support.